Dynamics and mass balance of Penny Ice Cap, Baffin Island, Nunavut, in a changing climate

Nicole Schaffer

Thesis submitted to the
Faculty of Graduate and Postdoctoral Studies
in partial fulfillment of the requirements for the degree of
Doctorate of Philosophy in Geography

Department of Geography, Environment and Geomatics
Faculty of Arts
University of Ottawa

ABSTRACT

This thesis presents a detailed study of recent changes in the mass balance and dynamics of Penny Ice Cap (PIC), and projects its evolution under a warming climate. Mass losses from 2005-2014 were quantified from airborne altimetry elevation change measurements, and adjusted for vertical ice motion caused by firn compaction and/or ice dynamics. Mass loss from PIC increased four-fold between the mid-1990s (-1.3 ± 0.7 Gt a^{-1}) and 2005-2013 (-5.4 ± 1.9 Gt a^{-1}). The adjustment calculations indicate that mass loss may be overestimated by 19% if vertical motion is not properly accounted for. The velocity response to increased surface melt was quantified using satellite imagery and historical ground measurements from Highway Glacier, on the southern part of PIC. Over the period 1985-2011, the six largest outlet glaciers on the ice cap decelerated at an average rate of 21 m a^{-1} over the 26 year period (0.81 m a^{-1}), or 12% $decade^{-1}$. Highway Glacier decelerated by 71% between 1953 and 2009/11. The recent slowdown of outlet glaciers has coincided with increases in mass loss and an inferred reduction in basal sliding. The ice-cap-wide mass balance was modeled from 1958 to 2099 with an enhanced temperature index model. Since the mid-1990s mass balance rates over PIC have become increasingly negative. Peak mass loss is projected to occur in the late 2070s and PIC is expected to lose 16-20% of its 2014 ice volume by 2099 assuming a moderate climate warming scenario (RCP4.5). If a +2°C offset is applied to this scenario, the ice cap is expected to lose 30-40% of its initial ice volume by 2099.

These results provide the first comprehensive evaluation of the impact of vertical ice motion on mass loss derived from geodetic measurements over a large Arctic ice cap. The ice velocity record provides insights into the relationship between surface melt rates and glacier motion over the past 30-60 years. This study projects the mass change of the largest ice cap in the southern Canadian Arctic to 2099, calibrated and validated with a wealth of spatially distributed data for the first time.

TABLE OF CONTENTS

LIST OF TABLES

LIST OF FIGURES

LIST OF ACRONYMS

AINA	Arctic Institute of North America
ATM	Airborne Topographic Mapper
AWS	Automatic weather station
CAA	Canadian Arctic Archipelago
CCF-O	Cross correlation method in the frequency domain called orientation correlation
CDED	Canada Digital Elevation Data
DEM	Digital elevation model
DETIM	Distributed Enhanced Temperature Index Model
dGPS	Dual-frequency global positioning system
ELA	Equilibrium line altitude
ESA EOLi	European Space Agency Earth Observation Link
ETM+	Enhanced Thematic Mapper Plus
GIS	Greenland Ice Sheet
GLAS	Geoscience Laser Altimeter System
GRACE	Gravity Recovery and Climate Experiment
GPR	Ground Penetrating Radar
ICESat	Ice, cloud, and land elevation satellite
IMAU	Institute for Marine and Atmospheric Research Utrecht
IPCC	Intergovernmental Panel on Climate Change
NE	Northeast
NW	Northwest
PIC	Penny Ice Cap
PMW	Passive spaceborne microwave
RCP	Representative Concentration Pathway
RGI	Randolph Glacier Inventory
RMSE	Root mean square error
s.w.e.	Snow water equivalent
SE	Southeast
SAR	Synthetic Aperture Radar
SLC-off	Scan line corrector off
SMB	Surface mass balance
SW	Southwest
TM	Thematic Mapper
w.e.	Water equivalent

LIST OF SYMBOLS

a	Ablation
A	Parameter dependent on ice temperature (Glen`s Flow Law)
α	Surface slope
b	Surface mass balance
$\dot{b}$	Surface mass balance rate
$\dot{b}_{dens}$	Mass balance rate inferred from $\dot{h}$ corrected for densification
$\dot{b}_{dyn}$	Mass balance rate inferred from $\dot{h}$ corrected for ice dynamics
$\dot{b}_{dyn\_dens}$	Mass balance rate inferred from $\dot{h}$ corrected for densification and ice dynamics
$\dot{B}$	Surface mass balance rate integrated over the entire glacier
c	Accumulation
C_i	Heat capacity of ice (2050 J kg^{-1} K^{-1})
d	Iceberg detachment
dZ	Thickness of the entire ice core
dZ_F	Thickness of firn layers containing ice
dZ_{MF}	Thickness of individual ice layers in a core
ρ	Density
$\dot{\rho}$	Firn densification rate
ρ_i	Density of ice
$\dot{\varepsilon}$	Strain rate
F_{ice}	Fraction of refrozen meltwater
$\dot{h}$	Surface elevation change rate
$\dot{h}_b$	Surface height change due to mass loss or gain
$\dot{h}_{dens}$	Densification component of height change
$\dot{h}_{dyn}$	Dynamic component of height change
$\dot{h}_{dGPS}$	Change in height measured at a stake
$\dot{h}_{slope}$	Elevation change rate due to the downslope movement of a stake
H	Ice thickness
$\dot{H}$	Surface elevation change rate integrated over the entire glacier
h_a	Thickness of the thermally active layer
I	Potential clear-sky direct solar radiation
L_f	Latent heat of fusion (0.334 x 10^6 J Kg^{-1})
M_f	Melt factor
MF%	Melt feature percent
n	Number of measurements
n_g	A constant that describes the flow of a material (Glen`s Flow Law)
P	Daily total precipitation
P_r	Maximum potential refrozen mass
r	Pearson's correlation coefficient
r^2	Coefficient of determination
R	Refrozen mass
$R_{f\ snow}$	Radiation factor for snow

$R_{f\ ice}$	Radiation factor for ice
T	Daily mean air temperature
T_s	Annual mean glacier surface temperature
T_{snow}	Threshold temperature
$\boldsymbol{\tau}$	Basal shear stress
σ	Standard deviation
σ°	Standardized backscatter values in decibels (dB)
U_i	Surface velocity due to internal deformation
U_{v_den}	Dynamic component of vertical velocity
U_{v_dyn}	Densification component of vertical velocity
U_{v_top}	Vertical velocity (U_v) measurement at the top of a mass balance stake
W_r	Available water mass
z	Elevation
ΔA	Change in glacier area
ΔV	Change in glacier volume

ACKNOWLEDGEMENTS

The support, encouragement and guidance of many mentors, friends, relatives and organizations have made the completion of this thesis possible. First, I would like to thank both my supervisors Dr. Luke Copland and Dr. Christian Zdanowicz. Luke for always being available and ready to help, providing many opportunities to develop as a scientist, encouraging and believing in me, and teaching me how to be super prepared for field work! Christian for being available when I needed his mentorship, his honesty, great sense of humor, care for my well-being, for providing me with the opportunity to study at Uppsala University in Sweden for one term, and for introducing me to Penny Ice Cap whose majestic beauty will always remain close to my heart. I would also like to acknowledge my committee members for their feedback and advice, Dr. David Burgess, Dr. Denis Lacelle and Dr. Konrad Gajewski.

I gratefully acknowledge my co-authors and those who have provided mentorship. Dr. David Burgess for his feedback and Dr. Johan Nilsson for providing ICESat elevation change data for Chapter 2. Dr. Laurence Gray for providing the speckle tracking code and Dr. Wesley Van Wychen for his mentorship on ice velocity analysis for Chapter 3. The Institute for Marine and Atmospheric Research (IMAU) group at the University of Utrecht, including Stefan Ligtenberg and Brice Noel, for providing me with RACMO2 data and valuable feedback. Dr. Regine Hock who patiently mentored me through modeling the surface mass balance of Penny Ice Cap for Chapter 4.

Thank you to all those who have helped with field work for this PhD. To both Christian and Luke for their assistance and guidance in the field. Alexandre Bevington who was an invaluable member of the team for two seasons. All of the Parks Canada wardens including Matthew Nakashuk, Matthew Nauyuk, Danial Kilabuk and Billy Etooangat and Monty Yank for their ready assistance, capable leadership on the land, and friendship. To Delia Siivola and Jane Chisholm at Parks Canada for helping with logistics. To many other field assistants including Patricia Peyton and Charles Latour. Many thanks to Alexander Chichagov and Mark Ednie from the Geological Survey of Canada. My colleagues at the Laboratory for Cryospheric Research who each contributed to the completion of this thesis through a supportive work environment, scientific discussion, and encouragement throughout my Ph.D.

Finally, to my family and friends who have helped me tremendously on this journey. My mom, Jua, for her keen interest in my thesis and for being there every step of the way. My parents Monica and Boris, sister Karina and extended family for their unconditional love and support. My main yoga teacher Janice DeFilippi, many other teachers and fellow yogis, for creating the space within which I found the internal strength, lightness and peace of mind to work through the challenging parts of my PhD and complete it in good health. To many close friends and my housemates for being there for me the entire journey, uplifting me in difficult times and celebrating my accomplishments.

I would also like to acknowledge various data providers: National Snow and Ice Data Center (IceBridge ATM data), GeoBase (CDED), European Space Agency (Envisat imagery) and the US Geological Survey (Landsat imagery). This work was supported by funding from the Ontario Graduate Scholarship (OGS), Natural Sciences and Engineering Research Council of Canada (NSERC), ArcticNet, Northern Scientific Training Program (NSTP), Canada Foundation for Innovation (CFI), Ontario Research Fund, Polar Continental Shelf Program (PCSP) and University of Ottawa.

CHAPTER 1: INTRODUCTION

1.1 BACKGROUND AND MOTIVATION

Mean annual air temperatures have increased by ~2°C in the Arctic since the 1950s, almost twice the global average rate [*AMAP-SWIPA*, 2011; *Sharp et al.*, 2011; *Vincent et al.*, 2015; Fig. 1.1]. Arctic summer temperatures in the last few decades have been higher than at any time in the last 2000 years according to paleoclimate reconstructions [*Kaufman et al.*, 2009]. These trends are reflected in the Canadian cryosphere, with warming permafrost throughout the Arctic, reduced snow cover extent and duration, reduced summer sea ice extent, and thinning and breakup of the remaining Canadian ice shelves [*Derksen et al.*, 2012]. Glaciers in the Canadian Arctic Archipelago (CAA) have responded to the warming with widespread mass losses, particularly since 2005 [*Gardner et al.*, 2011; *Sharp et al.*, 2011; *Fisher et al.*, 2012; *Harig and Simons*, 2016]. Current melt rates equal or surpass those observed over the last 3000 years on Penny Ice Cap (hereafter: PIC), southern Baffin Island [*Zdanowicz et al.*, 2012], and over the last 4000 years on Agassiz Ice Cap, Ellesmere Island [*Fisher et al.*, 2012]. Spaceborne altimetry and gravity measurements suggest that glacier losses in the CAA and Alaska are now the largest contributors to eustatic sea-level rise outside of the Greenland Ice Sheet (GIS) and Antarctica [*Gardner et al.*, 2012; *Jacob et al.*, 2012]. The greatest change has occurred in the southern CAA (Baffin and Bylot islands) where the area-averaged mass loss rate was 1.6 times that of the northern CAA over the period 2003-2009 [*Gardner et al.*, 2012]. The observed mass losses in the CAA have been directly attributed to increased air temperatures over the last few decades [*Gardner et al.*, 2011; *Sharp et al.*, 2011] as there is little evidence for a significant decrease in precipitation in this region since the 1950s [*Gardner et al.*, 2012; *Vincent et al.*, 2015]. By the end of the 21st century sustained and irreversible glacier mass losses in the CAA are predicted. A coupled atmosphere/snow model forced with the IPCC's moderate RCP4.5 greenhouse gas emission scenario forecasts an 18% loss of the current ice volume, with the mass loss rates increasing from -51 ± 26 Gt a^{-1} over 2000-2011 to -144 ± 33 Gt a^{-1} by 2100 [*Lenaerts et al.*, 2013].

Recent mass loss of glaciers and ice caps in the CAA has primarily been determined from elevation change (geodetic) measurements [e.g. *Abdalati et al.*, 2004; *Gardner et al.*, 2011,

2012]. In such studies mass loss is typically inferred directly from the observed surface elevation change of a glacier or ice cap over time ($\dot{h}$). However, $\dot{h}$ may change due to: a) glacier melt and subsequent runoff, b) an increased firn densification rate ($\dot{\rho}$), or c) compression or extension due to ice dynamics. To determine the true mass loss, factors b) and c) must be accounted for. There is ample evidence for increased firn densification in glaciers of the CAA. For example, at the summit of PIC the firn density has increased due to the percolation and refreezing of meltwater as ice layers, resulting in a 6% increase in cumulative ice-equivalent thickness between 1995-2010 [*Zdanowicz et al.*, 2012]. On Devon Ice Cap (northern CAA), the near-surface density increased by 13-80% between 2005-2012, associated with a surface lowering rate of 0.02 - 0.17 m a^{-1} [*Bezeau et al.*, 2013]. Several studies in the dry snow zones of the GIS and Antarctica have sought to account for $\dot{\rho}$ by modeling it and quantifying the contribution to observed $\dot{h}$ [*Cuffey*, 2001; *Zwally and Li*, 2002; *Li et al.*, 2003; *Shepherd et al.*, 2012; *Gardner et al.*, 2013; *Morris and Wingham*, 2014; *Ligtenberg et al.*, 2015]. Others have included $\dot{\rho}$ into the error estimate for mass change calculations [e.g. *Gardner et al.*, 2012]. However, the influence of $\dot{\rho}$ or ice dynamics on geodetic measurements over an entire ice cap has not been measured, and the significance of these factors for mass change measurements is currently poorly constrained.

Predicting the velocity response of glaciers to increased surface melt is another major topic of ongoing research, with significant implications for accurate sea level rise forecasting. Numerous studies have demonstrated that the movement of surface meltwater into the subglacial system leads to an over-pressurized basal drainage network, reduced basal friction, and a short-term increase in ice velocity [*Iken*, 1981; *Nienow et al.*, 1998; *Zwally et al.*, 2002; *Copland et al.*, 2003b; *Mair et al.*, 2003; *Bartholomew et al.*, 2012; *Fitzpatrick et al.*, 2013]. Faster ice motion can produce dynamic thinning [*Alley et al.*, 2005] and a greater drawdown of ice from higher elevations, resulting in a greater sensitivity of glacier mass balance to climate change [*Parizek and Alley*, 2004]. However, this positive correlation between increased surface melt and ice motion may not hold over longer time scales because increased meltwater can eventually aid in the evolution of a more efficient subglacial drainage system, leading to lower velocities [*Schoof*, 2010; *Sundal et al.*, 2011]. For example, Sundal *et al.* [2011] found a negative correlation between mean summer ice motion and melt for land-terminating glaciers in southwestern Greenland due to the early formation of an efficient channelized subglacial drainage network earlier in high melt years. Other studies have found a similar negative relationship with high

summer melt leading to a more efficient subglacial drainage system and lower velocities the following winter [*Burgess et al.*, 2013; *Sole et al.*, 2013; *Tedstone et al.*, 2013]. Despite an overall increase in surface temperature and melt rates in recent decades, deceleration of glaciers has been measured on the land-terminating region of the western GIS [*Tedstone et al.*, 2015] and many other non-surging glaciers elsewhere [*van de Wal et al.*, 2008; *Heid and Kääb*, 2012b; *Waechter et al.*, 2015] over longer time scales (>= 8 years).

For tidewater-terminating glaciers the velocity response over longer time scales has been more variable. For example, in Patagonia average velocities decreased by 20% per decade in a region dominated by water-terminating glaciers [*Heid and Kääb*, 2012b]. In the northern CAA, ~86% of glaciers showed no significant change in velocity over the period 1999-2015 [*Van Wychen et al.*, 2016]. However, Wykeham and Trinity glaciers on Ellesmere Island have doubled and tripled in speed, respectively, over this period, and now account for 62% of the total dynamic (iceberg) discharge from all ice masses in the northern CAA, compared to ~22% in 2000. Likewise, Kangerlussuaq and Helheim glaciers in southeast Greenland sped up by over 100% and 40%, respectively, between 2002-2005, following more than a decade of apparent stability [*Luckman et al.*, 2006]. This acceleration was the main reason for a doubling of annual discharge from the GIS in the early 2000s [*Luckman et al.*, 2006].

The aforementioned studies, as well as others, indicate that glacier velocities can vary considerably over time. It remains uncertain how increased meltwater will impact ice velocities in a warming climate, particularly for tidewater-terminating glaciers. Understanding this relationship between melt and ice velocities is critical for projecting future ice motion and accurate estimates of sea level rise contributions from glaciers.

A few studies have attempted to model the global- to regional-scale response of glaciers and ice caps to future warming, and some of these studies included PIC. *Lenaerts et al.* [2013] modeled the future fate of Canadian Arctic glaciers and ice caps using a coupled atmosphere/snow model, calibrated against mass balance data from northern part of the CAA only (Agassiz, Devon and Melville Ice Caps). Apart from the *Lenaerts et al.* [2013] study, PIC has only been included in global-scale assessments, which can have large uncertainties resulting from a lack of local model calibration or validation (e.g. *Radic and Hock*, 2011; *Marzeion et al.*, 2012; *Slangen et al.*, 2012; *Huss and Hock*, 2015). Hence, despite the rapid recent changes in mass balance observed in the

southern part of the CAA, the present and future mass balance of its largest ice cap, PIC, has never been properly modeled using spatially distributed in situ data for calibration and validation.

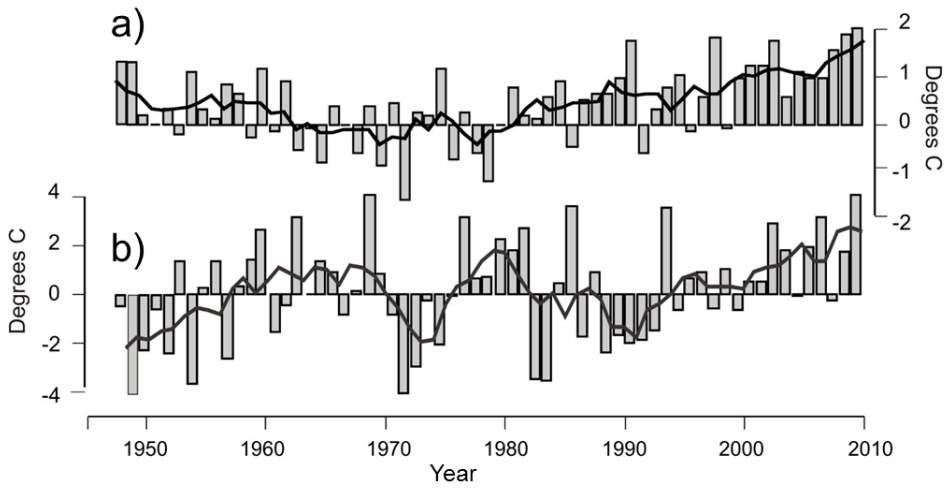

Figure 1.1: Surface air temperature anomalies relative to the mean of years 1961-1990 for a) summer (JJA) and b) winter (DJF) in the eastern Canadian Arctic from 1948 to 2010, calculated using historical weather station data. Reproduced from Zdanowicz et al. (2012) with permission of the American Geophysical Union.

1.2 RESEARCH QUESTIONS, THESIS ORGANIZATION, AND CONTRIBUTIONS

This thesis presents a detailed study of the recent mass balance and dynamics of PIC, and of its response to a changing climate. Mass losses are quantified from geodetic data corrected for the impacts of firn densification and ice dynamics, the velocity response to increased surface melt is assessed, and the ice-cap-wide mass balance is modeled from 1958 to 2099 using a modified temperature index model. The thesis is written in article format and each chapter addresses distinct questions, as described below.

Objective 1: How has the mass loss rate on PIC changed since 2005, and what are the impacts of firn densification and ice dynamics on mass losses derived from geodetic measurements?

This research objective is addressed in Chapter 2, in which NASA Airborne Topographic Mapper (ATM) altimetry elevation changes across Penny Ice Cap are updated to assess total changes in ice mass from 2005-2014. The components of the ATM altimetry-derived measurements of $\dot{h}$ that are due to ice dynamics and increased firn densification are calculated from dual-frequency GPS measurements and temporal changes in ice core density profiles, and the $\dot{h}$ due to net mass loss is isolated. Envisat satellite imagery is used to delineate the areas with subsurface firn that would be impacted by firn densification. This chapter has been submitted to the *Journal of Geophysical Research: Earth Surface*.

Schaffer, N,, Copland, L., Zdanowicz, C., Burgess, D. and Nilsson, J. (in review) Recent elevation changes of Penny Ice Cap, Baffin Island, corrected for ice dynamics and firn densification *J. Geophys. Res. Earth Surf.*

Objective 2: How has the velocity of PIC changed in recent decades in response to changes in mass balance?

In Chapter 3 optical and radar satellite imagery are used to produce a multi-decadal record of ice velocity variations on PIC. An ice-cap-wide velocity map is produced from 2011/2012 radar imagery and ice motion is mapped on the six largest outlet glaciers from 1985-2014 using optical imagery. The derived velocity data are also compared to in situ velocity measurements from

1953 on one outlet glacier, to in situ mass balance data collected since 2006, and to estimates of ice mass loss obtained with a time-varying mass balance model. This study provides a record of ice motion variability over the past 30-60 years and insights into the relationship between surface melt and ice velocities. This chapter has been submitted to the *Journal of Glaciology*.

Schaffer N, Copland L and Zdanowicz C (in review) Ice velocity changes on Penny Ice Cap, Baffin Island, since the 1950s. *J. Glaciol.*

Objective 3: How has the mass balance of PIC changed since 1958, and how will it evolve over the remainder of this century?

In Chapter 4 the daily mass balance of PIC is modeled from 1958 to 2099 using an enhanced temperature-index model calibrated with annual in situ mass balance data from 2006-2014 and ATM altimetry data from 2005-2013. The Distributed Enhanced Temperature Index Model (DETIM) [*Hock*, 1999] accounts for changes in incoming solar radiation and glacier retreat. The model is forced with the regional atmospheric climate model RACMO2 data [*Lenaerts et al.*, 2012; *Noël et al.*, 2015]. A new refreezing parameterization is also developed using ice core data to determine when the surface of PIC will become firn-free. This chapter will be submitted to a major peer-reviewed journal with the following citation:

Schaffer N, Copland L, Zdanowicz C, Hock R. Modeling the surface mass balance of Penny Ice Cap, Baffin Island, 1958-2099.

I am the primary author for all chapters presented in this thesis and am responsible for the collection, archiving and processing of the vast majority of data and the writing of manuscripts. Five datasets used in this thesis were obtained from other researchers: 1) the 2009-2013 ICESat elevation change measurements (Johan Nilsson, JPL) and 2) the raw RACMO2.1 and RACMO2.3 climate and mass balance data (Brice Noël, IMAU), 3) modeled ice thickness data (Matthias Huss, University of Fribourg), 4) passive microwave melt onset and end dates (Florent Dupont, CNRS), and 5) ice cap outlines (Evelyn Dowdeswell and Frances Delaney). David Burgess is a co-author on Chapter 2 for providing the 2005 ATM altimetry data and valuable feedback which was incorporated into this paper. Johan Nilsson is a co-author on Chapter 2 for providing the 2009-2013 elevation change data set. Regine Hock is a co-author on Chapter 4 for

providing the DETIM model used and invaluable feedback and mentorship. All ideas and analysis presented within this thesis are my own with feedback, edits and collaboration from my supervisors and co-authors.

1.2.2 ADDITIONAL CONTRIBUTIONS

In addition to the three papers that form this thesis, two co-authored papers and a technical document were produced:

Van Wychen, W., Copland, L., Burgess, D., Gray, L. and **Schaffer, N.** (2015). Glacier velocities and dynamic discharge from the ice masses of Baffin and Bylot Islands, Nunavut, Canada. *Canadian Journal of Earth Sciences, 52(11):980-989.*

Zdanowicz, C., Smetny-Sowa, A., Fisher, D., **Schaffer, N**., Copland, L. Eley, J., and Dupont, F. (2012). Summer melt rates on Penny Ice Cap, Baffin Island: past and recent trends and implications for regional climate. *Journal of Geophysical Research*, 117:F02006.

Schaffer, N. (2012). Glacier Velocities and Firn Line Position Determined using 2011 and 2012 RADARSAT-2 Imagery for Penny Ice Cap, Baffin Island, Nunavut. Technical report for Natural Resources Canada, Ottawa, Canada (reference #126758).

I will also create plain language summaries of Chapters 2, 3 and 4 in English and Inuktitut. These will be presented in an information pamphlet to be distributed by Parks Canada to visitors hiking through Akshayuk Pass and visiting Auyuittuq National Park. They will also be distributed to the community of Pangnirtung and posted on the Nunavut Climate Change Centre web site (http://climatechangenunavut.ca/en/node/3806).

1.3 STUDY LOCATION

With an area of ~6300 km^2, PIC (67°N, 66°W) is the southernmost large Canadian Arctic ice cap. It is located on Cumberland Peninsula, southern Baffin Island, which extends into Davis Strait (Fig. 1.2). The regional climate is relatively wet for an Arctic region [*Orvig*, 1954; *Maxwell*, 1981] and relative humidity over PIC often exceeds 90% in both summer and winter. Snow accumulates mostly in autumn (late August to mid-November), with some accumulation occurring in spring (late March to May), and is largely associated with the frequent passage of cyclones tracking north-northeast across or around southern Baffin Island [*Bradley*, 1973;

Maxwell, 1981; *Sorteberg and Walsh*, 2008; *Sepp and Jaagus*, 2010]. In late winter, the average annual snow cover measured at the summit of PIC is ~1-1.2 m, with a mean density of 350 kg m^{-3} [*Zdanowicz et al.*, 2012], and the mean ice accumulation rate inferred from ice core data is 0.4 m w.e. a^{-1} [*Zdanowicz et al.*, 2015]. The present-day mean annual air temperature at the ice cap summit, estimated from AWS recordings (1992-2000, 2007-2011) is -16 ± 1.5^0C [*Zdanowicz et al.*, 2012].

The eastern side of PIC has a higher topography and steep relief, reaching a maximum height of ~1930 m a.s.l. Major outlet glaciers flow from the summit area down deeply-incised valleys toward the north, east and south. Toward the west, PIC displays a smoother topography and terminates in a broad, gently sloping lobe-like region. There are two tidewater-terminating glaciers on PIC: Coronation Glacier terminating in Coronation Fjord, and Glacier 3 terminating in Okoa Bay (Fig. 1.2). In the 1950s Glacier 4 extended into Maktak fjord [*Ward and Baird*, 1954] but its terminus has since retreated inland. The majority of the ice cap moves slowly (<20 m a^{-1}), with faster motion limited to topographically constrained outlet glaciers that connect to large areas of accumulation in the interior. The highest velocities occur in areas of high relief and range from ~100 - 250 m a^{-1} [*Van Wychen et al.*, 2015]. The two tidewater-terminating glaciers discharge ~20 Mt a^{-1} combined, which accounted for ~0.2% of the total mass loss over Penny Ice Cap in 2011 [*Van Wychen et al.*, 2015]. Unlike Barnes Ice Cap (central Baffin Island) and Bylot Island Ice Cap, none of the outlet glaciers on PIC appear to be surge-type. The maximum ice thickness measured is ~880 m [*Shi et al.*, 2010].

The Arctic Institute of North America (AINA) carried out the first scientific expedition to PIC in 1953 [*Baird*, 1953; *Orvig*, 1954]. Various glaciological and climatological observations were made on the expedition including snow and ice stratigraphy and density, summer melt progression, ice thicknesses, ice velocities, surface mass balance and the energy budget [*Baird*, 1953; *Orvig*, 1954; *Ward*, 1954, 1955; *Ward and Baird*, 1954; *Rothlisberger*, 1955]. Research was focused on Highway Glacier and the adjacent southeastern portion of the ice cap (Fig. 1.2). In the ensuing decades (1960-1993), four field campaigns were conducted to measure ice thicknesses and ice movement near the ice cap summit, on Glacier 1 and on Highway Glacier [*Weber and Andrieux*, 1970; *Weber and Cooper*, 1993]. In 1979 and again in the mid-1990s several ice cores were drilled in the summit region of PIC, with the longest core reaching

bedrock at 334 m a.s.l. [*Holdsworth*, 1984; *Fisher et al.*, 1998]. These were updated with shallow ice cores drilled in 2010 and 2011 [*Zdanowicz et al.*, 2012].

In 2006, the Geological Survey of Canada initiated a program to monitor the surface mass balance (SMB) of PIC in collaboration with Parks Canada. Annual SMB measurements have been conducted along three survey lines converging at the summit AWS and on Coronation Glacier. From these SMB measurements, the mean equilibrium line altitude (ELA) was estimated to be ~1646 m between 2006-2014, but varied between ~1320 m in low mass loss years to ~1820 m during high mass loss years. At the lowest elevations, PIC thinning rates have been 3-4 m a^{-1}, amongst the highest rates in the Canadian Arctic [*Zdanowicz et al.*, 2012]. Spaceborne passive microwave (PMW) data show that the average onset and end of the summer melt period on PIC were ~May 23rd and ~September 3rd, respectively, over the period 2007-2010 (F. Dupont, personal communication, 2015).

Satellite-derived digital elevation models (DEMs) and altimetry data (ICESat) show that PIC has been losing mass since 1958, and this trend has accelerated in recent decades. The average mass loss rate between 2000-2005 was 443 ± 172 kg m^{-2} a^{-1} [*Gardner et al.*, 2012], more than double the loss rate calculated between 1995-2000 [*Abdalati et al.*, 2004]. The average melt season length on PIC has also nearly doubled between 1979 and 2010 according to the PMW data [*Zdanowicz et al.*, 2012]. The increased surface melt has resulted in the formation of thick infiltration ice layers in the firn which have increased its density and caused 10 m firn temperatures to rise ~10°C between the mid-1990s and 2011 [*Zdanowicz et al.*, 2012].

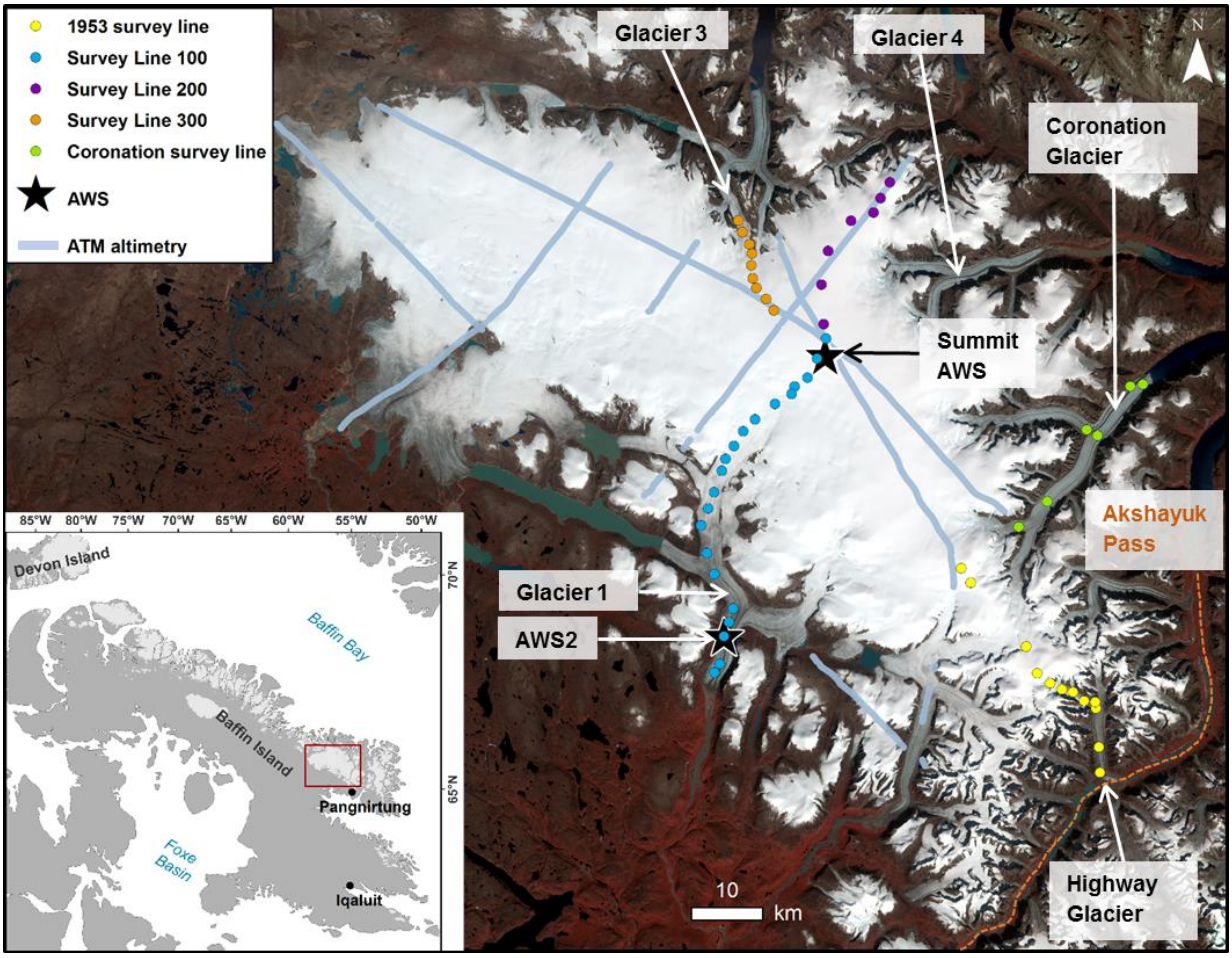

Figure 1.2: Map of Penny Ice Cap (67°N, 66°W) with five mass balance survey lines, automatic weather stations (AWS) and ATM altimetry flight lines. Glacier 3 and Coronation Glacier are tidewater-terminating and all other glaciers are land-terminating. Background image: Landsat 5, August 19, 1985.

CHAPTER 2: RECENT ELEVATION CHANGES OF PENNY ICE CAP, BAFFIN ISLAND, CORRECTED FOR ICE DYNAMICS AND FIRN DENSIFICATION

ABSTRACT

Measurements of ice cap changes are often based on geodetic methods, which calculate glacier-wide mass loss from elevation change over time. However, these measurements typically don't account for vertical ice motion caused by firn compaction and/or ice dynamics, so the significance of these factors for mass change measurements over an entire ice cap are currently poorly constrained. In this study, we update NASA Airborne Topographic Mapper (ATM) altimetry elevation changes across Penny Ice Cap (Baffin Island, Canada) to assess total changes in ice mass from 2005-2014. Dual-frequency GPS measurements and temporal changes in ice core density profiles are used to calculate vertical motion and isolate the ATM altimetry elevation change due to mass loss. Envisat satellite imagery is used to delineate the areas impacted by firn densification. These calculations, the first for a Canadian Arctic ice cap, indicate that failure to properly account for vertical ice motion results in a 19% overestimation of mass loss. The results, when corrected for vertical motion, are largely insensitive to the assumed density in the firn zone (900 or 800 kg m^{-3}). Overall, there has been a four-fold increase in mass loss from Penny Ice Cap between 2005-2013 (-5.4 ± 1.9 Gt a^{-1}) compared to the mid-1990s (-1.3 ± 0.7 Gt a^{-1}). The relatively rapid upglacier migration of the equilibrium line altitude (ELA) has left large areas of sub-surface firn in the current ablation area, and has far outpaced the dynamic response of the ice cap to the observed mass loss.

2.1 INTRODUCTION

Glaciers of the Canadian Arctic Archipelago (CAA) have experienced increasing rates of mass loss in recent decades, particularly since 2005 [*Gardner et al.*, 2011; *Harig and Simons*, 2016]. As a result, glaciers in this area are now the largest contributors to eustatic sea level rise outside of Greenland and Antarctica [*Gardner et al.*, 2011, 2013; *Jacob et al.*, 2012]. The southern part of the CAA (Baffin and Bylot islands) has lost ice mass at an area-averaged rate that is 1.6 times greater than the northern CAA over the period 2003-2009 [*Gardner et al.*, 2012]. There is little evidence for a significant decrease in precipitation in this region since the 1950s [*Gardner et al.*, 2012; *Vincent et al.*, 2015], so the main driver of mass loss is most likely greater summer melt.

Temperatures have increased throughout the southern Canadian Arctic since 1948 with the largest warming occurring in the winter months [*Vincent et al.*, 2015] and glacier mass balance has been highly correlated to summer temperatures [*Gardner et al.*, 2011; *Sharp et al.*, 2011]. Projections by a coupled atmosphere/snow model forced with the IPCC's moderate RCP4.5 greenhouse gas emission scenario forecasts sustained and irreversible glacier mass losses in the CAA, increasing from -51 ± 26 Gt a^{-1} over 2000-2011 to -144 ± 33 Gt a^{-1} by the end of the 21st century, resulting in a projected 18% loss of the current ice volume [*Lenaerts et al.*, 2013].

Geodetic methods have been heavily relied upon to quantify the response of glaciers and ice caps to climate warming over the past few decades [e.g. *Abdalati et al.*, 2004; *Gardner et al.*, 2011, 2012]. Typically in such studies, the observed surface elevation change of a glacier or ice cap over a given time interval ($\dot{h}$) is used to directly calculate its mass loss. However, there can be a change in surface elevation due to a change in firn densification rate ($\dot{\rho}$) or ice dynamics without actual mass loss. For example, on Devon Ice Cap (northern CAA), the near-surface firn density was found to have increased by 13-80% between 2005-2012, corresponding to a surface lowering rate of 0.02 - 0.17 m a^{-1} (Bezeau et al., 2013). At the summit of Penny Ice Cap (hereafter: PIC) on southern Baffin Island, the firn density also increased due to the formation of infiltration ice layers, resulting in a 6% increase in cumulative ice-equivalent thickness between 1995 and 2010 [*Zdanowicz et al.*, 2012]. To correct geodetic measurements of ice losses for this effect, several studies have sought to model $\dot{\rho}$ and quantify the contribution to observed $\dot{h}$ in the dry snow zones of Greenland and Antarctica [*Cuffey*, 2001; *Zwally and Li*, 2002; *Li et al.*, 2003; *Shepherd et al.*, 2012; *Gardner et al.*, 2013; *Morris and Wingham*, 2014; *Ligtenberg et al.*, 2015]. Geodetic studies have also incorporated densification into the error estimate for mass change calculations above the equilibrium line altitude [ELA; e.g. *Gardner et al.*, 2012]. However, to our knowledge no studies have measured the vertical component of ice motion or corrected geodetic data over an entire ice cap for the influence of firn compaction or ice dynamics.

This study focuses on PIC, which is the largest ice mass in the southern CAA (Fig. 2.1). In previous studies, elevation changes over PIC were estimated from NASA Airborne Topographic Mapper laser altimetry data (hereafter: ATM altimetry) between 1995-2005, ICESat satellite altimetry data between 2003-2009, and comparison of digital elevation models (DEMs) at lower

elevations on the ice cap between 1958-2009 [*Abdalati et al.*, 2004; *Gardner et al.*, 2011, 2012]. Since 2005, there have been two more ATM altimetry surveys over PIC in 2013 and 2014. Using these new data, as well as in situ geodetic and surface mass balance measurements, we updated estimates of $\dot{h}$ over PIC to 2014, and corrected these data to account for the effects of vertical motion due to ice dynamics and $\dot{\rho}$ using in situ data.

2.2 STUDY SITE

At 67°N and 66°W, PIC is the southernmost large Canadian Arctic ice cap, covering an area of ~6300 km^2 (Fig. 2.1). The ice cap rises to ~1930 m and major outlet glaciers flow from its interior down deeply-incised valleys toward the north, east and south. Higher topography and relief dominate the eastern side of the ice cap, trending toward lower elevations to the west where PIC terminates in a broad, gently sloping lobe-like region. The highest surface velocities on the ice cap occur on the outlet glaciers in areas of high relief, with rates of ~100-120 m a^{-1}, while the interior and the western sectors are generally slow-moving at <40 m a^{-1} [*Van Wychen et al.*, 2015]. In contrast to Barnes Ice Cap (central Baffin Island) and Bylot Island Ice Cap, none of the outlet glaciers on PIC appear to be surge-type [*Van Wychen et al.*, 2015].

There are two tidewater terminating glaciers on PIC: Coronation Glacier in the south-east sector, and an unnamed glacier in the north-central sector. These glaciers discharge ~11 and ~9 Mt a^{-1}, respectively [*Van Wychen et al.*, 2015], which accounted for ~0.2% of the total mass loss over PIC in 2011. The mean, maximum and minimum annual air temperatures measured at the summit of PIC between Aug. 1 2007 – July 31 2008 were -15.4°C, 2.9°C and -42.9°C, respectively [*Zdanowicz et al.*, 2012]. Annual surface mass balance measurements have been conducted on PIC since 2006 along three survey lines (designated 100, 200 and 300; Fig. 2.1). Based on these measurements, the mean equilibrium line altitude (ELA) between 2006-2014 was ~1646 m, varying between ~1320 m in low mass loss years to 1820 m during high mass loss years. The average surface mass balance along the 100 survey line (Fig. 2.1), which covers an elevation range of 329 m to 1817 m, was -1.3 m w.e. a^{-1} between 2007-2014, but varied from -0.8 to -1.7 m w.e. a^{-1} during low and high mass loss years, respectively [*Van Wychen et al.*, 2015]. Maximum ice thicknesses on PIC are >700 m at 1500 m elevation ~3 km north of stake P105 [*Weber and Andrieux*, 1970; *Weber and Cooper*, 1993], and a borehole drilled near

the summit in 1995 (1860 m a.s.l.) reached bedrock at a depth of ~334 m [*Fisher et al.*, 1998]. More recent measurements confirm a maximum thickness of 880 m measured with a NASA airborne radar in 2013 ~5.5 km northwest of P106 [*Shi et al.*, 2010].

The average dates for the onset and end of the summer melt period, as determined from spaceborne passive microwave (PMW) measurements, were ~May 23rd and ~September 3rd, respectively, over the period 2007-2010 (F. Dupont, personal communication, 2015). These same PMW data revealed that the average melt season length on PIC nearly doubled between 1979 and 2010 [*Zdanowicz et al.*, 2012]. Borehole and shallow core measurements from the ice cap's summit show that the firn density has been increasing since the mid-1990s due to the formation of thick infiltration layers, and deep meltwater percolation has caused firn temperatures at 10 m depth to rise by ~10°C between the mid-1990s and 2011. In recent years, 70-100% of the annual accumulation was in the form of infiltration ice. *Zdanowicz et al.* [2012] reported that the increased melt and length of the melt season observed since the 1980s is associated with increasingly positive summer and winter air temperatures in the eastern Arctic.

2.3 DATA AND METHODS

In this study we compiled new observations of $\dot{h}$ from ATM altimetry over 2005-2013 and 2013-2014, and compared these estimates to dual-frequency global positioning system (dGPS) measurements (2011-2014), mass balance measurements (2006-2014) and ICESat laser altimetry (2003-2009). We corrected the ATM altimetry $\dot{h}$ data for ice dynamics using measurements of vertical motion made with a dGPS along three mass balance survey lines on PIC (Fig. 2.1). Corrections for enhanced $\dot{\rho}$ (i.e. exceeding those expected under Sorge's law), were determined from ice cores collected near the summit. The spatial extent over which the corrections apply were determined by mapping the areal extent of the firn zone using Envisat Synthetic Aperture Radar (SAR) imagery, validated with Ground Penetrating Radar (GPR) measurements along three survey lines crossing PIC. These data sources and methodology are described in detail below.

2.3.1 *Elevation change*

2.3.1.1 *Airborne laser altimetry*

In spring 2005, 2013 and 2014, repeat airborne ATM altimetry measurements were performed over PIC by NASA prior to the start of the ablation season (Fig. 2.1). The 11 May 2005 mission used NASA's ATM sensor, which has a conical scanning laser to measure surface elevations. Resolution varies with altitude flown and scanner configuration, but for a typical flight altitude of 500 m above the ice cap surface the swath width is ~140 m, with each laser shot having a 1-3 m footprint, a ground spacing of 2-5 m and nominal vertical accuracy of <0.2 m [*Krabill et al.*, 1995]. Since 2009 the ATM has been used in NASA's Operation IceBridge. The altimetry data on 12 April 2013 and 23 April 2014 were collected with a swath width of ~230 m, measurement density of ~1 per 10 m^2, a footprint of ~0.5 m, and a nominal vertical accuracy of <0.1 m [*Krabill*, 2013].

We used the ATM L1B elevation dataset, in which each ATM surface elevation corresponds to one raw laser pulse (http://nsidc.org/data/docs/daac/icebridge/ilatm1b/, last accessed February 2, 2016). A line of best fit composed of points at 10 m spacing was drawn through the original 2005, 2013 and 2014 ATM altimetry L1B data in ESRI ArcMap 10.1. The elevations of ATM data points closest to the line of best fit were extracted using a Matlab script and subtracted between 2005-2013 and 2013-2014 to obtain the changes in elevation over time ($\dot{h}$). Points >10 m apart or with $\dot{h}$ values equal to or greater than twice the maximum in situ measured annual accumulation or ablation (>= 3 or <= -8 m a^{-1}) were excluded from the analysis. Points with $\dot{h}$ values outside the 99.99% confidence interval (>5 times the standard deviation about the ATM altimetry mean) were also excluded. A manual check was then completed to remove anomalous points in areas of high relief, outside the ice cap, or where patterns were physically implausible (e.g a change in $\dot{h}$ of 3 m a^{-1} or more between adjacent data points). The ice cap extent was digitized manually from late summer 2014 Landsat 8 images. All elevation changes were standardized to units of meters per year (m a^{-1}).

2.3.1.2 *In situ mass balance and dGPS*

Surface mass balance measurements were made annually on a fixed-date system [*Cogley et al.*, 2011] at stakes along three survey lines during spring (100, 200, 300 lines) and on Coronation

Glacier during summer between 2006-2014, totalling 140 measurements at elevations ranging from 71-1822 m a.s.l. (Fig. 2.1). Snow pits were dug at most stake locations annually and a known volume of snow or firn from each stratigraphic layer was weighted to determine the density. Ice lenses were assumed to have a density of 900 kg m^{-3}. Thirty-two of these measurements were within 250 m horizontally of the 2005-2013 ATM altimetry survey lines.

High accuracy coordinates were collected along the 100, 200 and 300 survey lines in April each year from 2011 to 2014 using a Trimble R7 dGPS receiver, with a minimum 20 minute occupation time per stake. The total number of stakes measured with the dGPS were 33, 28, 34 and 3, respectively, in 2011, 2012, 2013 and 2014. The dGPS data were post processed using the Precise Point Positioning method provided by Natural Resources Canada (http://www.geod.nrcan.gc.ca/online_data_e.php), with resultant accuracies ± 0.08 m horizontally and ± 0.10 m vertically at the 95% confidence level calculated from 15 dGPS measurements.

2.3.1.3 *ICESat*

ICESat elevations measured by the Geoscience Laser Altimeter System (GLAS) in 2009 and airborne ATM altimetry measurements by NASA along the same ICESat lines in 2013 were used to calculate $\dot{h}$ from 2009-2013. ICESat data were collected during two campaigns in 2009: spring (2E; 09 March 2009 – 11 April 2009) and fall (2F; 30 September 2009 – 11 October 2009). GLAS has a footprint of ~70 m and an average along-track spacing of 172 m [*Zwally et al.*, 2011]. A vertical accuracy better than 0.05 m is possible under optimal conditions [*Fricker et al.*, 2005]. However, the accuracy decreases over sloping terrain to 0.14 m and 0.86 m for 0-1° slopes and 3-5° slopes, respectively [*Brenner et al.*, 2007; *Moholdt et al.*, 2010]. The GLAS data were downloaded from the National Snow and Ice Data Centre (http://nsidc.org/data/icesat/index.html; GLA06L1B global surface elevation data product, release R33), and processed using the methodology of *Nilsson et al.* [2015]. Raw ICESat data was filtered using quality flags and rejection parameters included in the product release. Tracks with large offsets were removed from the dataset and ICESat elevations were converted to the WGS84 ellipsoid from the TOPEX/Poseidon ellipsoid. The average elevation of ATM altimetry data within a 70 m radius of each ICESat point was used to calculate the difference between the 2009 ICESat and 2013 ATM altimetry data.

2.3.2 *Ice-cap-wide mass loss calculation*

Surface elevation changes ($\dot{h}$) along ATM altimetry lines were extrapolated to the entire ice cap using least-squares regression of $\dot{h}$ against elevation. The resulting equation was applied to each grid cell of the Canadian Digital Elevation Data (CDED) DEM of PIC to obtain a $\dot{h}$ raster, using the ice cap extent from late summer 2014. The CDED DEM has a resolution of 3-12 arc seconds, which equates to an average grid cell size over PIC of ~93 m x ~37 m. The firn or ice volume change for each grid cell was then calculated from $\dot{h}$, and the results were summed to generate an estimate of the total volume change over the whole ice cap. This was converted to snow water equivalent (w.e.) by multiplying cells by the average density of ice determined from ice cores (900 kg m^{-3}), following Sorge's law [*Bader*, 1954], and converted to mass loss (Gt a^{-1}). To assess the sensitivity of the calculations to the assumed density of the firn zone, we also calculated the mass loss with a density of 800 kg m^{-3} applied to the firn zone, based on the average density of the 2013 ice/firn core from the summit of PIC.

2.3.3 *Adjustments to elevation change measurements*

Geodetic measurements of glacier elevation change are a measure of the combined effects of surface mass balance and the vertical component of ice motion. At a point on the glacier surface, $\dot{h}$ is defined by a special case of the continuity equation:

$$\dot{\boldsymbol{h}} = \frac{\dot{\boldsymbol{b}}}{\boldsymbol{\rho}} + \boldsymbol{\nabla Q} \tag{1}$$

Where $\dot{b}$ is the surface mass balance rate, ρ is the associated density, and ∇Q is the flux divergence [*Cuffey and Paterson*, 2010]. Equation 1 assumes that densification, internal and basal mass balance, isostatic displacement and erosion of the glacier bed are negligible. For repeat geodetic measurements taken at fixed coordinates on the ice surface (such as the ATM altimetry measurements used here), $\dot{h}$ equals the sum of $\dot{b}$ and the dynamic component of vertical ice velocity $\left(U_{v\_dyn}\right)$ if it is assumed that the density stays constant over time [*Beedle et al.*, 2014; *Cuffey and Paterson*, 2010] :

$$\dot{\boldsymbol{h}} = \frac{\dot{\boldsymbol{b}}}{\boldsymbol{\rho}} + \boldsymbol{U_{v\_dyn}} \tag{2}$$

If equation 2 is integrated across the entire glacier surface while assuming negligible changes in glacier surface area and no flux across the glacier boundary (e.g. from avalanching or calving), and further assuming that U_{v_dyn} sums to zero, the equation simplifies to:

$$\dot{H} = \frac{\dot{B}}{\rho} \tag{3}$$

Where $\dot{H}$ and $\dot{B}$ are elevation change and surface mass balance integrated over the entire glacier area. The relationship in equation 3 is frequently used to calculate mass loss from elevation change measurements, but is only valid for obtaining average mass change for the entire glacier. To calculate $\dot{b}$ for a given point on the glacier, or for a portion of the ice mass, equation 3 is not applicable since U_{v_dyn} does not sum to zero, and equation 2 must be used instead. Determining the mass loss over a portion of a glacier is useful for understanding spatial variability in mass balance and local impacts of glacier melt, such as the amount of meltwater contributing to a particular drainage basin.

Studies of borehole cores indicate that the firn density has increased substantially on large ice caps in the Canadian Arctic in recent decades as a result of melting and internal refreezing of meltwater [*Zdanowicz et al.*, 2012; *Bezeau et al.*, 2013]. Therefore, possible changes in densification cannot be neglected and equation 2 must be modified to account for this:

$$\dot{h} = \frac{\dot{b}}{\rho} + U_{v\_dyn} + U_{v\_den} \tag{4}$$

where U_{v_den} represents the vertical motion due to densification. Rearranging equation 4 to solve for $\dot{b}$ gives:

$$\dot{b} = (\dot{h} - U_{v\_dyn} - U_{v\_den})\rho \tag{5}$$

In this study we solve equation 5 by calculating both U_{v_dyn} and U_{v_den}. This result is extrapolated over the entire ice cap and then compared to extrapolation of the uncorrected ATM altimetry $\dot{h}$ data multiplied by the density (equation 3). U_{v_dyn} was determined from in situ dGPS measurements (section 2.3.3.1). U_{v_den} was calculated from PIC ice cores (section 2.3.3.2) and used to adjust ATM altimetry data on portions of the ice cap where firn is near the surface.

2.3.3.1 *In situ measurements of vertical motion*

Total vertical motion was quantified at 13 locations over PIC using in situ dGPS observations collected from 2011-2014 at the top of each mass balance stake (U_{v_top}) (section 2.3.1.2). U_{v_top} contains contributions from both U_{v_dyn} and U_{v_den} in the firn zone, so the methodology described in section 2.3.3.4 was used to separate these components. While many more dGPS measurements were collected, only those measured on the same stake in two consecutive years were used for this analysis. The U_{v_top} over one year at each stake was calculated by subtracting the change in height due to the downslope movement of the stake between measurements ($\dot{h}_{slope}$) from the total change in height measured at each stake over one year ($\dot{h}_{dGPS}$) as defined in equation 6:

$$\boldsymbol{U_{v\_top} = \dot{h}_{dGPS} - \dot{h}_{slope}} \quad (6)$$

The surface slope was derived from independent kinematic dGPS surface elevation measurements over a horizontal distance of 200 m (100 m upglacier and downglacier of each point). The mass balance stakes were drilled 1-3 m into the near surface firn (or ice) and therefore assumed to remain frozen solid, so the U_{v_top} measurements were presumed to be unaffected by changes in surface height due to mass loss or gain. It was also assumed that the stakes did not melt downwards into the ice.

2.3.3.2 *Firn densification*

To determine the change in surface height due to densification (U_{v_den}) in the firn zone, we used ice core data from 1995, 2010 and 2013 collected near the summit of PIC (Fig. 2.2). The 1995 and 2010 cores were drilled 3.6 km east of the automatic weather station (AWS) located at an elevation of 1860 m. The 1995 core reached bedrock at a depth of 334 m, while the 2010 core was 23 m long [*Zdanowicz et al.*, 2012]. The 2013 core was 6.7 m long and drilled adjacent to the AWS at an elevation of 1813 m. For each core the length and mass of each section (~20-40 cm long) was measured. Firn-core stratigraphy was documented from visual observations and checked against the measured density.

U_{v_den} was calculated from the change in thickness of near-surface layers equivalent to a total of 5 m w.e., which corresponds to the minimum core length of 6.7 m for the 2013 core. This equates to ~17 years of accumulation based on the mean 1963-2010 accumulation rate of 0.39 m a^{-1} determined by *Zdanowicz et al.* [2012]. The changes were calculated for 1995-2010 and 2010-2013, with the 2005-2013 change determined from a weighted average of these periods. This method of calculating thickness change only accounts for densification due to melting and refreezing and does not account for densification due to dry compaction or densification occurring below an equivalent depth of 5 m w.e. However, this is a reasonable assumption since firn density models and observations indicate that greatest compaction occurs near the surface. For example, the firn density model developed at the Institute for Marine and Atmospheric Research Utrecht (IMAU), indicates that U_{v_den} within the upper 6 m is nearly double that of firn between 6-10 m and six times the compaction below 10 m depth for Antarctica [*Ligtenberg et al.*, 2015]. The model results agree with ice core measurements from Devon Ice Cap in 2004 and 2012, where the majority of layers in the top 5 m at an elevation of 1630 m, and in the top 3 m at an elevation of 1825 m, had a density change which exceeded two standard deviations of the mean density in the bottom 10 m of the core. This demonstrates that the changes in the top 5 m and 3 m, respectively, were well above what is attributable to historically normal climatic variability [*Bezeau et al.*, 2013].

2.3.3.3 *Identification of firn zone and ice-rich regions*

A 500 MHz pulseEKKO PRO GPR was towed behind a snowmobile across all three surface mass balance survey lines (Fig. 2.1) during spring field measurement campaigns in 2011, 2012 and 2013. It was programmed with a time window of 1000 ns (giving a penetration depth of ~80 m) and positions were recorded using an integrated single frequency GPS receiver or external Trimble R7 dGPS system. To determine the radar wave velocity we used values of the dielectric constant inferred from the densities of shallow cores, following the methodology of *Kovacs et al.* [1995]. The resulting radargrams were used to identify the areal extent of the firn zone in which firn layers are dominant to a depth of ~10 m (Fig. 2.3), based on the presence of internal layering and high backscatter [*Sylvestre et al.*, 2013]. The GPR data interpretation was verified using shallow cores collected during spring 2011 with a Kovacs Mark II corer (9 cm internal diameter)

to a depth of ~6 m below the glacier surface (Fig. 2.1). For each core, we recorded the stratigraphy and weighed each section to calculate its density (Fig. 2.4).

Envisat Wide Swath ScanSAR (Synthetic Aperture Radar C-Band) imagery from Oct. 19th 2010 were used to extrapolate the position of the firn-ice transition (boundary between the firn zone and ice below) identified in the GPR records to all of PIC. This imagery has a resolution of 150 m, a swath width of 405 km, and was obtained through the European Space Agency Earth Observation Link (ESA EOLi) catalogue. A scene acquired in a period of below-freezing conditions was selected to avoid complications in image interpretation due to surface melt. The Envisat image was orthorectified, radiometrically corrected, and standardized to backscatter values (σ°, in dB) in PCI Geomatica. The resulting raster was imported into ArcGIS and values along the 100 and 300 survey lines were extracted for direct comparison with GPR results. The locations of the firn/ice transition (firn zone boundary) identified on the GPR radargrams were superimposed with the Envisat data and a threshold backscatter value was chosen to identify the transition point and delineate the firn zone.

2.3.3.4 *Altimetry elevation change adjustments*

Adjustments of the ATM $\dot{h}$ data for U_{v_den} and U_{v_dyn} were determined for each term individually:

$$\dot{b}_{\boldsymbol{dens}} = (\dot{h} - U_{v\_\boldsymbol{den}})\,\rho \tag{7}$$

$$\dot{b}_{\boldsymbol{dyn}} = (\dot{h} - U_{v\_\boldsymbol{dyn}})\,\rho \tag{8}$$

We used the ice core derived U_{v_den} value to: (1) adjust the ATM $\dot{h}$ data for firn densification rates (U_{v_den}) within the firn zone, and (2) quantify the dynamic component ($U_{v\_\boldsymbol{dyn}}$) of U_{v_top} from the stake measurements. We used a constant value of U_{v_den} and subtracted this value from the ATM altimetry data ($\dot{h}$) within the firn zone. A best fit quadratic polynomial model was used to extrapolate the corrected data to the entire ice cap to obtain the $\dot{h}_{\boldsymbol{dens}}$ raster. This was subsequently multiplied by the density to obtain $\dot{b}_{\boldsymbol{dens}}$ (eq. 7).

In the firn zone the densification below each stake was calculated from the ice cores and subtracted from U_{v_top} to isolate the dynamic contribution (U_{v_dyn}). It was assumed that the

stakes were locked into the ice such that densification occurring between the bottom of the stake and the surface (top 1.7 m on average) did not impact the U_{v_top} measurement. Below the firn zone, U_{v_dyn} was obtained directly from the U_{v_top} measurements since there is no densification there. Linear regression was used to extrapolate U_{v_dyn} across the ice cap, and the resulting U_{v_dyn} raster was subtracted from the uncorrected raster $(\dot{h})$ to provide an ice-cap-wide elevation change raster corrected for ice dynamics ($\dot{h}_{dyn}$). To obtain a raster corrected for both densification and dynamics ($\dot{h}_{dyn\_dens}$), we subtracted the U_{v_dyn} raster from the $\dot{h}_{\boldsymbol{dens}}$ raster. This was subsequently multiplied by the density to obtain $\dot{b}_{\boldsymbol{dyn\_dens}}$:

$$\dot{b}_{\boldsymbol{dyn\_dens}} = (\dot{h}_{dens} - U_{v\_dyn}) \, \rho \tag{9}$$

2.4 RESULTS

2.4.1 *Altimetry measurements*

The measurements of $\dot{h}$ derived from ATM altimetry between 2005-2013 were negative over the entire ice cap, with thinning rates ranging from ~0.5 m a^{-1} in the summit area to >2 m a^{-1} at lower elevations on outlet glaciers, and on the northwestern sector of the ice cap (Fig. 2.5a). For 2013-2014, $\dot{h}$ were less, with negligible changes in the summit area, and thinning rates >2 m a^{-1} limited to small isolated areas at the lowest elevations (Fig. 2.5b). The $\dot{h}$ over 2005-2013 derived from ATM altimetry data were compared to those measured by dGPS at 13 mass balance stakes between 2011-2014. For each stake, ATM altimetry data acquired within a similar elevation band (± 10 m vertically) were selected and a range of descriptive statistics were calculated (Table 2.1). The mean difference between the $\dot{h}$ obtained by dGPS and by ATM altimetry was 0.04 m, and the RMSE was 0.39 m.

In Figure 2.6 we compare the ATM altimetry $\dot{h}$ data to in situ surface mass balance stake data, plotted as changes in surface height due to mass loss or gain ($\dot{h}_b$). If interpreted in terms of mass changes, the ATM $\dot{h}$ data tend to overestimate ice losses at higher elevations (> ~1500 m) and underestimate losses at lower elevations. This pattern holds true when comparing the 2005-2013 ATM altimetry data with 2006-2013 surface mass balance measurements (Fig. 2.6a), or the

2013-2014 altimetry data with 2013-2014 surface mass balance measurements (Fig. 2.6b). This is expected due to the effect of the vertical component of ice motion [*Hagen et al.*, 2005], which increases the apparent ice loss rate at high elevations due to submergence, and lessens it at lower elevations due to emergence. Different simple models were least-square fitted to the data (Fig. 2.6). A second order polynomial gave the best-fit for the 2005-2013 ATM data (adjusted R^2 = 0.88), but the fit was poorer for the 2013-2014 data (adjusted R^2 = 0.46) owing to the large variability of $\dot{h}$ values for a given elevation band in a single year (Fig. 2.6), which average out in the 2005-2013 data. All regressions for ATM and mass balance stake data were significant (F-test p-value < 0.001) with regression coefficients that were significant (standard error p-value < 0.001).

Changes in melt and/or internal accumulation over the study period can be independently verified by comparing shallow (~6 m) cores collected adjacent to the AWS in the summit region of PIC in 2011 and 2013. The amount of infiltration ice, or "melt features" (MF) in the cores was quantified by calculating the volumetric percentage of the core occupied by ice, following *Zdanowicz et al.* [2012] :

$$\boldsymbol{MF}\% = \frac{\sum(\boldsymbol{dZ_{MF}}) + \sum(\boldsymbol{dZ_F F_{ice}})}{\sum \boldsymbol{dZ}} \quad (10)$$

Where dZ_{MF} is the thickness of individual ice layers in the core, dZ_F is the thickness of firn layers containing ice, F_{ice} is the fraction of refrozen meltwater in the firn layers and dZ is the thickness of the entire core. Here we used an assumed mean value of 5% for F_{ice}, after *Zdanowicz et al.* [2012]. Our computations indicate that the MF% in firn at the summit of PIC increased from 46 to 79% between 2011 and 2013, suggesting that increased melt resulted in the formation of more and thicker internal ice layers.

2.4.1.1 *Estimating the accuracy of ATM altimetry*

The primary sources of uncertainty when calculating glacier mass changes from ATM altimetry data are: (1) uncertainties in the actual airborne measurements; (2) $\dot{h}$ due to glacial isostatic adjustment; (3) changes in glacier area through time; (4) extrapolation of $\dot{h}$ to determine a glacier-wide volume change; (5) assumption of a constant density for converting volume to mass change; and (6) variations in $\dot{\rho}$ due to changes in precipitation, compaction rates and internal

accumulation (refreezing of meltwater). These errors are summarized in Table 2.2 for each data set, following *Gardner et al.* [2012]. We also re-assessed errors due to ATM altimetry measurements, as these may have changed since the last assessment of data collected in 1999 by *Krabill et al.* [2002].

To assess errors in the ATM altimetry measurements, we compared: (i) the 2013 ATM altimetry measurements of PIC collected on 12 April 2013 to dGPS data collected on PIC between 8-16 April 2013; (ii) elevation values at crossover points between different altimetry swaths in 2013; and (iii) $\dot{h}$ between 2005-2013 over flat bedrock. The NASA flight on 12 April 2013 covered all previously surveyed ATM altimetry lines (Fig. 2.1), plus several new lines along the ICESat ground tracks (Fig. 2.5a). Three static dGPS points and 719 kinematic dGPS points directly overlapped the ATM altimetry point cloud and all dGPS measurements were above 1550 m elevation. The mean differences between ATM elevations and dGPS points (i.e., ATM-dGPS) was -0.52 m for the static locations, and -0.43 m for the kinematic locations, implying that the ATM altimetry measurements are approximately 0.5 m lower than the ice surface measured with the dGPS.

At crossover locations we differenced the cloud of points within the overlapping area from the two passes, using the Matlab script described in section 2.3.1.1. For crossover points within 1 m horizontally the average difference in elevation was 0.005 m (RMSE = 0.15 m) and for points within 10 m horizontally the average difference in elevation was 0.011 m (RMSE = 0.27 m) (Table 2.3; Fig. 2.1). Error estimates in this study are higher than the 0.08 m RMSE for crossover points and 0.01 m a^{-1} RMSE for modelled errors calculated by *Krabill et al.* [2002]. However, the *Krabill et al.* [2002] crossover points were from the central part of the Greenland Ice Sheet, where there is less topographic variation than at PIC, and they summarized data into 70 m square blocks that likely reduced the calculated RMSE compared to the analysis of individual points used here. Elevation change between 2005-2013 measured over flat bedrock surrounding PIC averaged 0.033 m a^{-1} (RMSE = 0.052 m a^{-1}) (Table 2.3).

Errors in Table 2.2 are reported in terms of the 95% confidence interval. The measurement error was obtained by multiplying the largest RMSE value of 0.27 m for crossover points (within 10 m horizontal distance) by 1.96 to define the 95% confidence interval, and by the ice density to

convert to kg m^{-2}. This value was then divided by the number of years in the record to standardize to an annual value.

2.4.1.2 *Ice-cap-wide changes*

To calculate ice-cap-wide mass losses, we extrapolated the 2005-2013 ATM altimetry $\dot{h}$ data to the whole ice cap DEM using the quadratic relationship against elevation (Fig 2.6; section 2.3.2). To test if this quadratic model is appropriate for the entire ice cap, the ATM altimetry $\dot{h}$ data was divided into four quadrants (NW, NE, SW and SE) and the least squared best fit models were computed in each quadrant. Results showed little difference from the best fit obtained with the entire data set, so we opted to use one best fit model for the entire ice cap. Extrapolation of the ATM altimetry $\dot{h}$ data over PIC assuming a mean ice density of 900 kg m^{-3} gives a mass loss rate ($\dot{b}$) of -5.4 ± 1.9 Gt a^{-1} between 2005-2013 (Table 2.2; Fig. 2.7), which is over four times the amount of ice lost per year between 1995-2000 [-1.3 ± 0.72 Gt a^{-1}; *Gardner et al.*, 2012]. The same calculation over 2013-2014 gives a mass loss rate of -3.3 ± 1.5 Gt a^{-1} (Table 2.2; Fig. 2.7). This figure is less negative than the mean for 2005-2013 because 2013-2014 was one of the least negative mass balance years over the past decade, as shown by mass balance data collected on PIC since 2006, and also by spaceborne gravity [*Harig and Simons*, 2016] and altimetry measurements [*Gray et al.*, 2015].

Comparison of 2005-2013 ATM altimetry $\dot{h}$ data with 2009-2013 ICESat/ATM $\dot{h}$ data reveals very similar patterns at and near crossover points (Fig. 2.5). Extrapolation of the 2009-2013 ICESat data yields a mass loss rate of -5.3 ± 1.8 Gt a^{-1}, which is identical, within error, to the mass loss computed from the 2005-2013 ATM altimetry data (Fig. 2.7).

2.4.2 *Elevation change adjustments*

2.4.2.1 *Firn zone delineation and adjustment for firn densification*

Prominent internal layering in the radargrams for the 100, 200 and 300 GPR survey lines enables identification of the regions where firn is present on PIC (Fig. 2.3). The firn/ice transition from low elevation glacier ice regions (with low backscatter) to the upper elevation firn zone (with high backscatter) is most obvious on the 100 line radargram, because this transect covers the greatest elevation range (Fig. 2.3a). The transition is also visible on the 300 line (Fig. 2.3c). We define the firn zone as an area dominated by firn to ~10 m depth, whereas the firn line refers to

the transition from ice to firn at the glacier surface. The GPR interpretations were verified with shallow ice cores taken above and below the firn line (Fig. 2.4), with core 1 (1813 m a.s.l.) dominated by firn below the winter snow cover, whereas core 2 (1560 m a.s.l.) was dominated by ice. Sections within each core dominated by firn correspond to darker (high backscatter) sections on the radargram, while those dominated by ice correspond to lower backscatter since ice is nearly transparent at radio-wave frequencies (Fig. 2.4). This relationship is also seen at a larger scale where areas underlain predominantly with firn (i.e., firn zone) have higher backscatter and areas mostly underlain by ice, below the firn/ice transition, have lower backscatter (Fig. 2.3).

The location of the firn-ice transitions identified in the GPR traces are shown in Figure 2.8 and these correspond to a threshold of -5 dB for the Envisat data at an elevation of ~1300 m a.s.l. on the 100 line (Fig. 2.8 inset). This compares well with the firn-ice transition on Devon Ice Cap, which corresponds to backscatter thresholds of -5 to -7.8 dB (1246 to 1276 m a.s.l.) on winter RADARSAT-1 images from 2003-2006 [*Casey and Kelly*, 2010]. At elevations below the firn-ice transition, Envisat backscatter values on PIC drop steadily and never rise above -5 dB.

Using this threshold, each pixel in the Envisat image was classified as either ice (< -5 dB) or firn (> -5 dB) and the firn zone was defined by a boundary above which >75% of the pixels were classified as firn. This boundary was drawn manually. Testing with automated delineation resulted in a comparable outline, but with a jagged boundary that would be physically implausible. In the upper parts of the glacier the GPR-derived firn line corresponds to an Envisat backscatter value of approximately -2 dB, although this boundary is not as sharp as the firn-ice transition.

Firn densification was assumed to occur only within the firn zone. The value of 0.25 m a^{-1} for U_{v_den} over the period 2005-2013, derived from the change in thickness of the ice cores, was subtracted from $\dot{h}$ within the firn zone. The estimated changes in ice core thickness for the top 5 m w.e. were 0.08 m and 0.53 m, respectively, between 1995-2010 and between 2010-2013. The corrected ATM data set quadratic polynomial (adjusted R^2 = 0.89) was used to extrapolate across the CDED DEM and obtain the $\dot{h}_{dens}$ map (Equation 7) shown in Figure 2.9b.

2.4.2.2 *Adjustment for ice dynamics*

The dynamic component of vertical velocity (U_{v_dyn}) was obtained from dGPS measurements (U_{v_top}) by removing the change in surface height due to densification occurring below the bottom of the stakes (1.7 m to 6.7 m below the surface; 0.21 m a^{-1} in the firn zone) to isolate the dynamic component. The U_{v_dyn} values are positive in the lower parts of the glacier (emergence), but become increasingly negative (submergence) with increasing elevation (Fig. 2.10a). The surface mass balance rate ($\dot{h}_b$) varies in opposition, but the magnitude of variations is not equal to U_{v_dyn}. At the lowest elevation (348 m a.s.l.), U_{v_dyn} is ~0.98 m a^{-1} while $\dot{h}_b$ is ~ -3.5 m a^{-1} or >3.5 times U_{v_dyn}. Moving upglacier the deviation decreases with $\dot{h}_b$ 3.2 times U_{v_dyn} at ~910 m a.s.l. and roughly in balance at the current ELA of ~1646 m a.s.l. (U_{v_dyn} = 0.15 m a^{-1}, $\dot{h}_b$ = -0.13 m a^{-1}). The transition between submergence and emergence occurs between ~1000 – 1400 m elevation (Fig. 2.10a).

To correct the ATM altimetry data for dynamics, values of U_{v_dyn} were plotted against elevation (Fig. 2.10b) and a linear model was fitted to these data with an adjusted R^2 value of 0.79 (p-value = <0.001) and significant coefficient (standard error p-value = <0.001). This linear model was applied to each grid cell on the CDED DEM to obtain the U_{v_dyn} component across all of PIC (Fig. 2.11). The dynamic equilibrium line (U_{v_dyn} = 0) across the ice cap delineates the boundary between submergence above and emergence below, covers a range of elevations from ~1100 – 1500 m a.s.l. (Fig. 2.11), and is more than 300 vertical meters below the current ELA. The mean value of U_{v_dyn} over the entire ice cap is -0.04 m a^{-1}. The U_{v_dyn} raster was subtracted from the $\dot{h}$ raster to obtain the $\dot{h}_{dyn}$ raster (Fig. 2.9c; Equation 8) and from the $\dot{h}_{dens}$ raster to obtain the final $\dot{h}_{dyn\_dens}$ raster shown in Figure 2.9d.

2.4.2.3 *Uncorrected vs. corrected estimates of ice cap mass loss rates*

Correcting the 2005-2013 $\dot{h}$ data for densification decreases the mass loss rate in the firn zone, resulting in a glacier wide loss rate of -4.6 Gt a^{-1} (ρ = 900 kg m^{-3}), which is 15% less than the uncorrected mass loss rate (Table 2.4). Correcting for ice dynamics increases the mass loss rate at lower elevations and decreases it at higher elevations (Fig. 2.9c, 2.11), resulting in a glacier wide mass loss rate of -5.2 Gt a^{-1}, which is 4% less than the uncorrected mass loss rate of -5.4 Gt

a^{-1} (Table 2.4). When both corrections are applied, the resulting mass loss rate is -4.4 Gt a^{-1}, 19% below the uncorrected mass loss rate. This is a marked difference, but still within the margin of error for the uncorrected estimate (+/- 1.9 Gt a^{-1}). The RMSE between the in situ surface mass balance measurements and a quadratic fit through the 2005-2013 ATM altimetry data (Fig. 2.12), which was 0.62 m for the uncorrected ($\dot{h}$) data set, is slightly reduced to 0.59 m when the corrected data ($\dot{h}_{\boldsymbol{dyn\_dens}}$) are used instead.

If a density of 800 kg m^{-3} is applied in the firn zone and 900 kg m^{-3} is applied elsewhere on the ice cap, the resulting values of $\dot{b}, \dot{b}_{dens}, \dot{b}_{dyn}$ and $\dot{b}_{dyn\_dens}$ are -5.2 Gt a^{-1}, -4.5 Gt a^{-1}, -5.1 Gt a^{-1} and -4.4 Gt a^{-1}, respectively (Table 2.4). The mass loss for the uncorrected $\dot{h}$ data is overestimated by 3.5% over PIC if volume loss is converted to mass loss using 900 kg m^{-3}. In contrast, the $\dot{h}$ data set corrected for vertical motion is much less sensitive to a change in the assumed mean density of the firn zone, and the overestimation reduces to 0.7%.

2.5 DISCUSSION

The repeat ATM altimetry measurements should provide a good representation of mass loss over an entire ice cap if: 1) $\dot{h}$ values are obtained over a fairly uniform distribution of elevation bands across the ice cap; 2) the vertical component of ice dynamics (U_{v_dyn}) sums to zero; and 3) the firn density does not vary over time. We do not consider point 1 above to be a significant factor in our measurements as the ATM flight lines over PIC were generally well distributed with elevation (albeit with a slight bias toward higher elevations, with 53% of measurements at >1500 m). The mean ice-cap-wide U_{v_dyn} of -0.04 m a^{-1} is within error limits of the dGPS measurements (0.1 m a^{-1}) and may therefore be explained by measurement error. Nonetheless, correcting elevation changes derived from repeat ATM surveys with this rate reduces the mass loss estimates by 4% when compared with uncorrected results (Table 2.4). The negatively biased mean U_{v_dyn} may be due to compaction as the stake measurements ($U_{v_{top}}$) in the firn zone were corrected for densification from melting and refreezing, but not for dry compaction. The $\dot{\rho}$ is increasing over time (section 2.4.2.1) and correcting for this decreases the mass loss estimates by an additional 15% (Table 2.4).

Other studies have reported an over-estimation of mass loss from surface elevation change measurements (geodetic method) compared to direct surface mass balance measurements (glaciological method). For example, *Krimmel* [1999] reported a cumulative mass balance of -22 m w.e. over the period 1970-1997 with the geodetic method, and -15 m w.e. over the same period with the glaciological method for South Cascade Glacier (Western U.S.A.). Likewise, on Castle Creek Glacier (western Canada), geodetic measurements using dGPS indicated a negative glacier-wide mass balance of -1.26 ± 0.99 m w.e. for the period 2009-2011, compared to a positive balance of 0.10 ± 0.63 m w.e. from surface mass balance measurements over the same time interval [*Beedle et al.*, 2014].

The positive densification rate calculated from ice cores on PIC is supported by a near-doubling of the MF% in the top 6 m of firn near the summit between 2011-2013, coincident with an increase in the cumulative thickness of ice layers observed in GPR profiles along the 100 survey line. Similar changes in stratigraphy have been observed on other ice caps in the CAA and on Greenland, especially following the exceptional high melt summer of 2012 [*Zdanowicz et al.*, 2012; *Bezeau et al.*, 2013; *Gascon et al.*, 2013; *Machguth et al.*, 2016]. A comparison of ice core records to a modeled density profile, which assumes the density profile remains constant through time, clearly illustrates that near surface densities far exceed the constant profile by 2013 (Fig. 2.2). Densities were modeled with a Matlab program written by Aslak Grinsted based on the Herron-Langway model forced with thermistor cable measurements of temperature 10 m below the surface (-3˚C; *Zdanowicz et al.*, 2012), the average accumulation rate from ice core records (0.4 m w.e. a^{-1}; *Zdanowicz et al.*, 2015) and surface density from the 2013 core (340 kg m^{-3}). Within the top 6 m below the surface the average density in 2013 was 820 kg m^{-3}, while the average modeled density over the same depth was 450 kg m^{-3}.

The surface lowering due to densification in the top 1.25 m w.e. depth on PIC of 0.04 m a^{-1} over the period 2005-2013 is comparable to the rates of 0.02-0.12 m a^{-1} calculated by *Bezeau et al.* [2013] between 2004-2012 for cores collected near the summit of Devon Ice Cap. This study highlights the importance of also accounting for densification at greater depths, given that densification in the top 1.25 m w.e. on PIC only accounts for 16% of the total surface lowering of 0.25 m a^{-1} that occurred in the top 5 m w.e. A potential limitation in our methods is the application of a single densification rate for the entire firn zone based on measurements from a

single location near the summit. However, while it is almost certain that the near surface firn stratigraphy is heterogeneous, the GPR profiles (Fig. 2.3) do not show a noticeable change in the rate of densification with elevation, so applying a constant rate is probably a reasonable approximation.

Analysis of Envisat imagery shows that there are large areas of subsurface firn at elevations >400 vertical meters below the current ELA of 1646 m. Likewise, the dynamic equilibrium line is >300 m below the current ELA. If the ice cap was in equilibrium with the climate, the dynamic equilibrium line would be at the ELA and the firn-ice transition would be slightly upglacier at the boundary between the superimposed ice zone and wet snow zone. These discrepancies may be explained by the four-fold increase in mass loss rate since the mid-1990s and associated rapid upglacier migration of the ELA. There are few historical measurements of the ELA across PIC, but the study of *Ward and Baird* [1954] showed that it was at 1380 m a.s.l. on Highway Glacier in 1953. The current firn-ice transition at ~1300 m a.s.l. and the dynamic equilibrium line at ~1100 – 1500 m a.s.l. are much closer to this 1953 ELA, suggesting a delayed response time to the recent increase in melt rates. Similar results have been documented for Devon Ice Cap, where the ELA migrated upglacier 188 m vertically between 2003-2006, but the firn-ice transition only migrated 24 m upglacier and was 140 m below the ELA in 2006 [*Casey and Kelly*, 2010].

2.6 CONCLUSIONS

Mass loss on PIC has increased rapidly over the past two decades, with a four-fold increase in mass loss rate since the mid-1990s associated with increasingly positive temperature anomalies [*Zdanowicz et al.,* 2012] and a rapid upglacier migration of the ELA (currently at ~1646 m), leading to large areas of subsurface firn at elevations >400 vertical meters below the current ELA. The accumulation area now only covers ~20% of the ice cap and there was a near-doubling of the MF% in the top 6 m of firn near the summit from 2011-2013. The ice cap has not yet adjusted dynamically to its recent changes, with the dynamic equilibrium line corresponding to a historical ELA >300 vertical meters below the current one. If PIC were in equilibrium with current climate the vertical component of velocity (U_{v_dyn}) would be expected to be approximately zero at the ELA, and U_{v_dyn} would be equal in magnitude and opposite in

direction to the long-term mass balance. Instead, the mass balance is currently >3.5 times U_v at low elevations.

Neglecting to account for densification due to increased melt/refreezing on PIC may result in a 15% overestimation of mass loss rate from ATM $\dot{h}$ measurements, and a further 4% overestimation if emergence and submergence rates are ignored. The corrected $\dot{h}$ dataset is relatively insensitive to the assumed density in the firn zone, with a reduction in mass loss of 0.7% if a density of 800 kg m^{-3} is used instead of the usual 900 kg m^{-3}. This insensitivity reflects the relatively small firn area remaining on the ice cap. These results highlight the importance of accounting for the vertical component of ice motion when computing geodetically-derived mass balance changes.

The patterns of elevation change observed across PIC, with the largest thinning rates at low elevations on outlet glaciers and the northwestern sector of the ice cap, closely match the spatial distribution of $\dot{h}$ in previous studies [*Abdalati et al.*, 2004; *Gardner et al.*, 2012]. The rates of mass loss calculated from uncorrected ATM data continue a progression of increased mass loss rate over time (Fig. 2.7), from -1.3 ± 0.7 Gt a^{-1} between 1995-2000 [*Abdalati et al.*, 2004], to -2.9 ± 1.1 Gt a^{-1} between 2000-2005 [*Gardner et al.*, 2012] and -5.4 ± 1.9 Gt a^{-1} between 2005-2013. However, the results presented here suggest that these values may be overestimated by as much as 19%, with an adjusted value of -4.4 Gt a^{-1} probably being more realistic over the period 2005-2013. However, the lack of data on firn densification and vertical ice motion in earlier periods limits our ability to determine by how much earlier measurements should be corrected. Increased mass loss rate over the last two decades on PIC is consistent with similar trends observed over Baffin and Bylot Islands for Barnes, Grinnell and Terra Nivea Ice Caps with $\dot{h}$ derived from many independent datasets including ATM, ICESat, DEMs and mass changes from GRACE [*Gardner et al.*, 2011, 2012, *Papasodoro et al.*, 2015, 2016].

This study represents the first evaluation of the impact of vertical motion on ice-cap-wide extrapolation of altimetry data in the Canadian Arctic, and highlights the need for further investigation to determine the influence of U_v on geodetically-derived mass balance rates on other ice caps. Ideally, this would involve measurement of firn densification from ice cores over a range of elevations and dGPS measurements of U_v and horizontal displacement on a detailed ice-cap-wide grid to reduce the uncertainty associated with extrapolating across an ice mass.

Independent measurements of slope (e.g. from a kinematic dGPS survey) would be essential since the correction for down-slope movement of the stakes can significantly alter the final U_v values.

Table 2.1: Annual surface height change ($\dot{h}$) measured at 13 dGPS mass balance stakes between 2011-2014 and the average of 2005-2013 ATM altimetry data within the same elevation band (± 10 vertical meters). The standard deviation (StDev) and number (n) of ATM altimetry points within each ± 10 m elevation band, and the difference between the two data sets and RMSE, are given for each stake location. Stakes within 250 m horizontal distance of the 2005-2013 ATM altimetry lines are in bold. All values are in meters.

Stake ID	**Year (dGPS)**	**Elev-ation (dGPS)**	$\dot{h}$ **(dGPS)**	$\dot{h}$ **(ATM)**	**StDev (ATM)**	**n (ATM)**	$\dot{h}$ **(dGPS) -** $\dot{h}$ **(ATM)**	**RMSE**
P000	2011-2012	1822	-0.76	-0.52	0.04	1322	-0.24	0.24
P101	2011-2012	1804	-0.77	-0.52	0.05	934	-0.25	0.25
P102	2011-2012	1722	-0.83	-0.48	0.10	762	-0.35	0.35
P103	2011-2012	1647	-0.35	-0.48	0.09	454	0.13	0.13
P104	2011-2012	1556	-0.90	-0.62	0.07	1165	-0.28	0.28
P105	2011-2012	1472	-0.45	-0.70	0.12	677	0.25	0.25
P105	2013-2014	1472	-0.55	-0.70	0.12	677	0.15	0.15
P110	2012-2013	1075	-0.25	-1.38	0.14	262	1.13	1.13
P112	2011-2012	943	-1.68	-1.37	0.11	383	-0.31	0.31
P113	2011-2012	880	-0.98	-1.43	0.10	123	0.44	0.44
P120	2011-2012	348	-2.51					
P202	2011-2012	1716	-0.58	0.48	0.10	826	-1.07	1.07
P203	2011-2012	1662	-0.55	-0.47	0.10	455	-0.08	0.08
Average			**-0.72**	**-0.68**	**0.10**	**670**	**-0.04**	**0.39**

Table 2.2: Estimates of mass loss rates for PIC inferred from ATM altimetry data sets with respective uncertainties derived from the methodology used by *Gardner et al.* [2012]. Table entries for 1995-2000 and 2000-2005 are reproduced from *Gardner et al.* [2012].

Time period	**PIC area (km^2)**	**dM/dt ($\dot{b}$)**		**Sources of error (95% confidence interval) ($kg\ m^{-2}\ a^{-1}$)**						
		($kg\ m^{-2}\ a^{-1}$)	**$Gt\ a^{-1}$**	**Measur-ement**	**GIA**	**Glacier area**	**Extrap-olation**	**Bulk density**	**Trends in firn density**	**Total**
1995-2000	6508	-194	-1.3	95	5	19	61	4	87	**145**
2000-2005	6508	-443	-2.9	95	5	43	139	8	87	**194**
2005-2013	6316	-858	-5.4	60	5	86	266	16	87	**299**
2013-2014	6316	-526	-3.3	476	5	53	163	10	87	**514**

Table 2.3: Descriptive statistics for apparent 2005-2013 ATM elevation changes on flat bedrock, and for 2013 NASA crossover points on the ice cap <1 m apart horizontally and <10 m apart horizontally.

Statistic	**Flat bedrock**	**Crossover points (<1 m)**	**Crossover points (<10 m)**
Count	330	791	4054
Min (m)	-0.181	-0.850	-2.505
Max (m)	-0.069	0.577	2.596
Mean (m)	-0.033	-0.005	-0.011
RMSE (m)	0.052	0.149	0.267

Table 2.4: Total mass loss rate over PIC (dM/dt) calculated from uncorrected (ATM) and corrected (ATM_{cor}) 2005-2013 airborne altimetry $\dot{h}$, using density scenarios of 900 and 800 kg m^{-3} in the firn zone and 900 kg m^{-3} elsewhere. The differences between the mass loss rates calculated from the uncorrected and corrected ATM data are expressed as a percentage of the unadjusted data ($\dot{b}$) using a density of 900 kg m^{-3} over the entire ice cap.

Scenario	**dM/dt ($\rho = 900$) (Gt a^{-1})**	**Percentage (ATM_{cor}/ATM)**	**dM/dt ($\rho = 800$) (Gt a^{-1})**	**Percentage (ATM_{cor}/ATM)**
$\dot{b}$	-5.41	---	-5.22	96.5
$\dot{b}_{dens}$	-4.61	85.2	-4.49	83.0
$\dot{b}_{dyn}$	-5.20	96.1	-5.10	94.3
$\dot{b}_{dyn\_dens}$	-4.40	81.3	-4.36	80.6

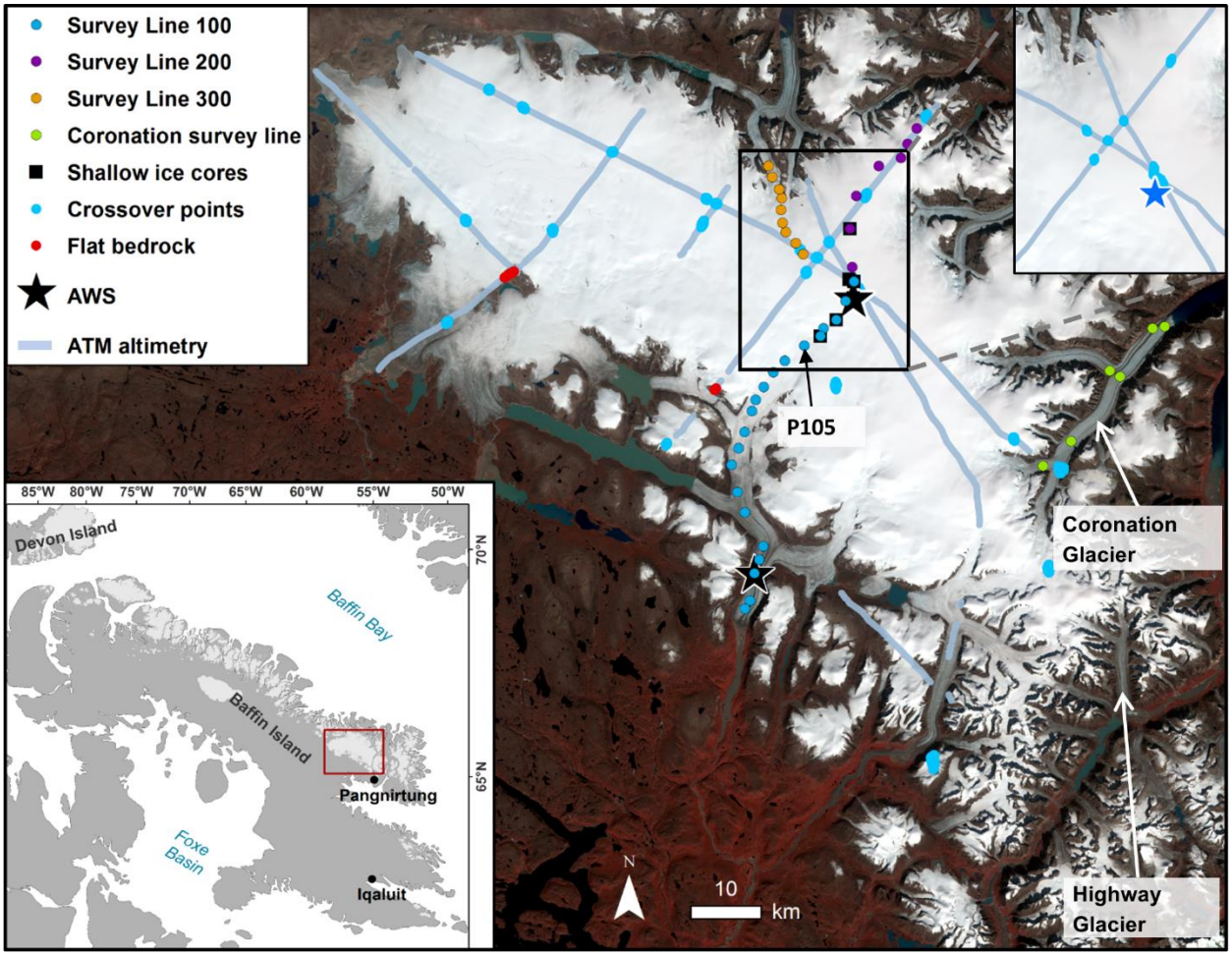

Figure 2.1: Map of Penny Ice Cap (67°N, 66°W) with mass balance survey lines, location of shallow ice cores, automatic weather station (AWS), ATM altimetry flight lines, 2013 ATM altimetry crossover points and location where 2005-2013 $\dot{h}$ (elevation change) was computed over flat bedrock. Crossover points outside the glacier boundary were excluded from the error analysis. Background image: Landsat 5, 19 August 1985.

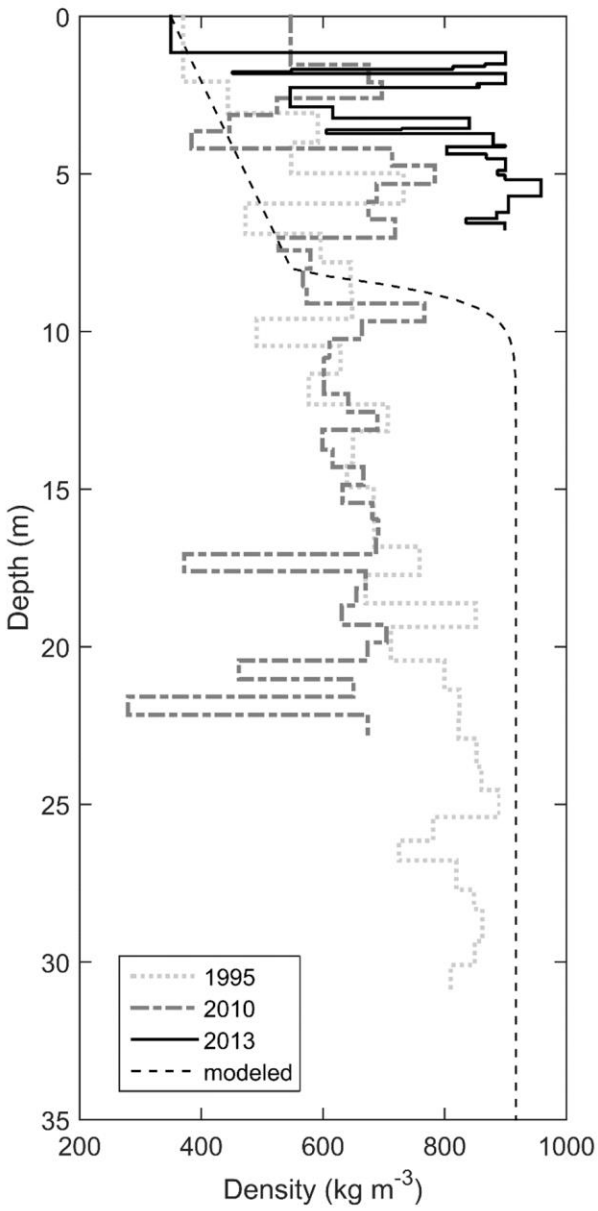

Figure 2.2: Density profile of ice cores from 1995, 2010 and 2013. The 2013 core was drilled adjacent to the AWS (Fig. 2.1), while the two older cores were drilled 4.6 km east of the AWS. A modeled profile, which assumes a constant density profile through time, is plotted with a dashed line.

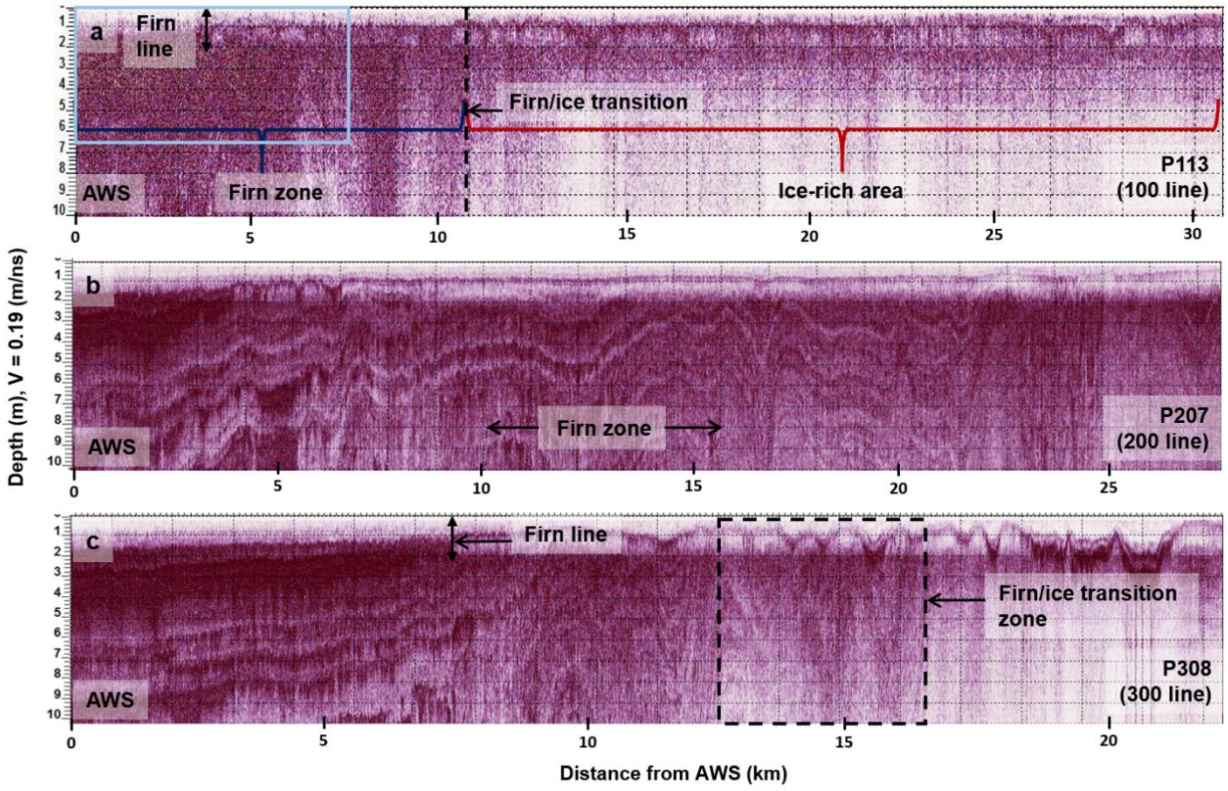

Figure 2.3: (a) April 2011 GPR radargrams for transects along the 100 line, (b) 200 line, and (c) 300 line (Fig. 2.1). All transects start at the AWS (left) and terminate down-glacier at the designated stake location (right). Dashed black lines or arrows denote GPR-derived transition points or zones (firn line or firn/ice transition). An expanded version of the radargram outlined with a blue rectangle in (a) is shown in Figure 2.4.

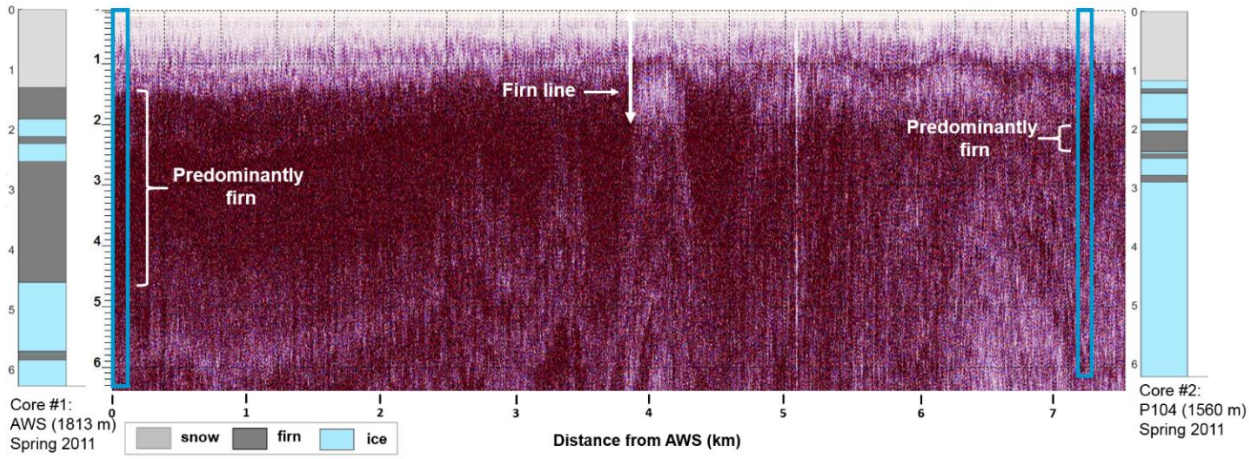

Figure 2.4: April 2011 GPR radargram along the 100 line (Fig. 2.3a) between core #1 at the AWS (1813 m) and core #2 (1560 m) drilled 10-12 May 2011. Hollow blue rectangles represent the ice core locations and length (m). The composition is illustrated in adjacent ice core plots and the white line denotes the GPR-derived firn line.

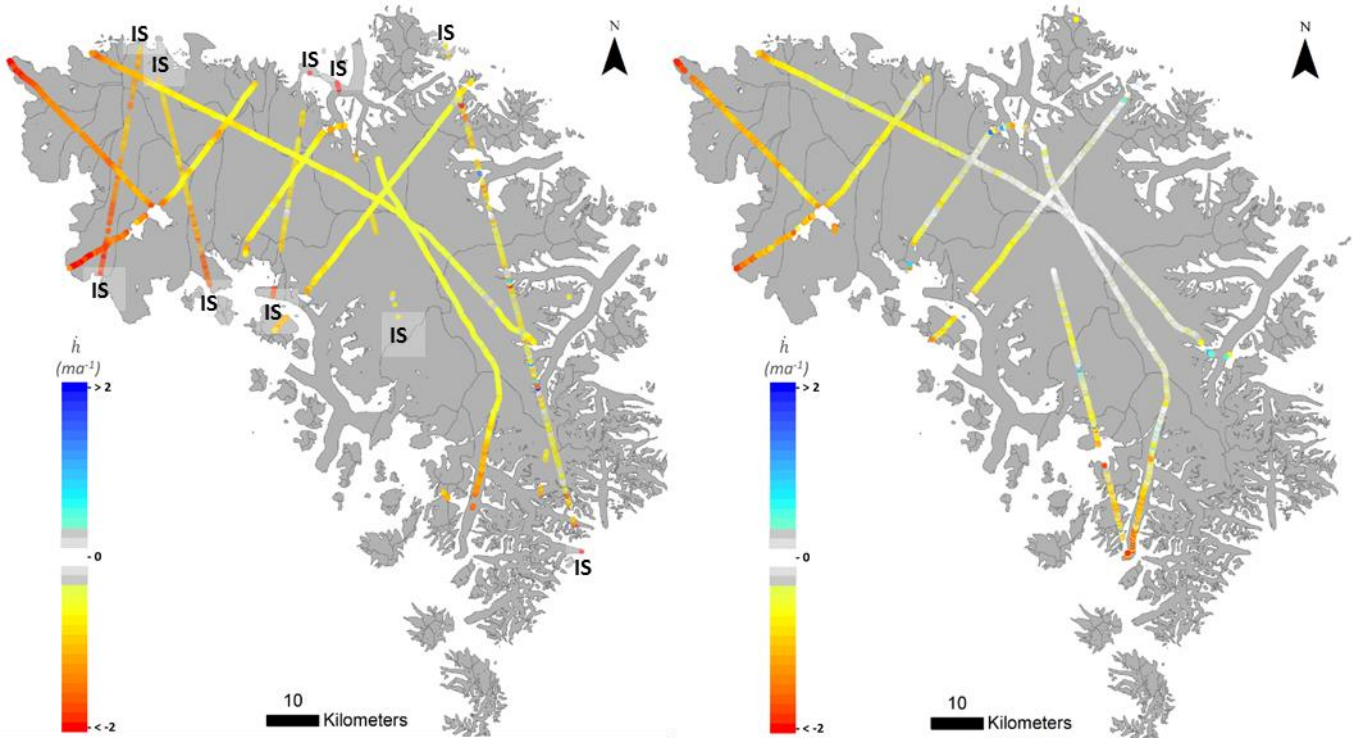

Figure 2.5: ATM altimetry surface elevation change ($\dot{h}$) along ATM flight lines between: a) 11 May 2005 – 23 April 2013 and b) 12 April 2013 – 23 April 2014. In part a) $\dot{h}$ from 2009 ICESat and 2013 altimetry data on ICESat lines is also plotted, with ICESat lines lighter in colour and labeled IS at both ends.

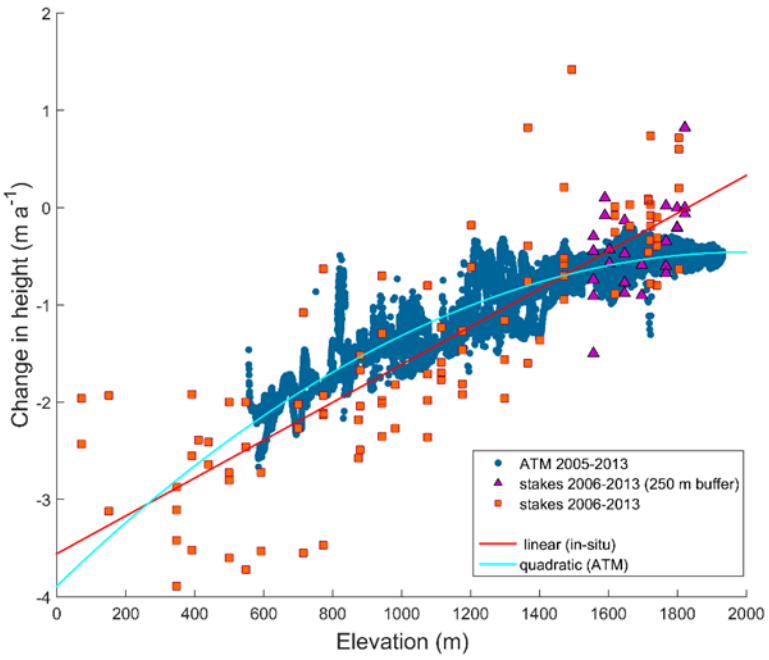

Statistic	Mass balance stakes	ATM 2005-2013
Regression type	Linear	Quadratic
Intercept	-3.56	-3.92
Coefficient (z)	0.0019	0.0035
Coefficient (z^2)		-8.77×10^{-7}
Adjusted R^2	0.72	0.88
p-value	< 0.001	< 0.001

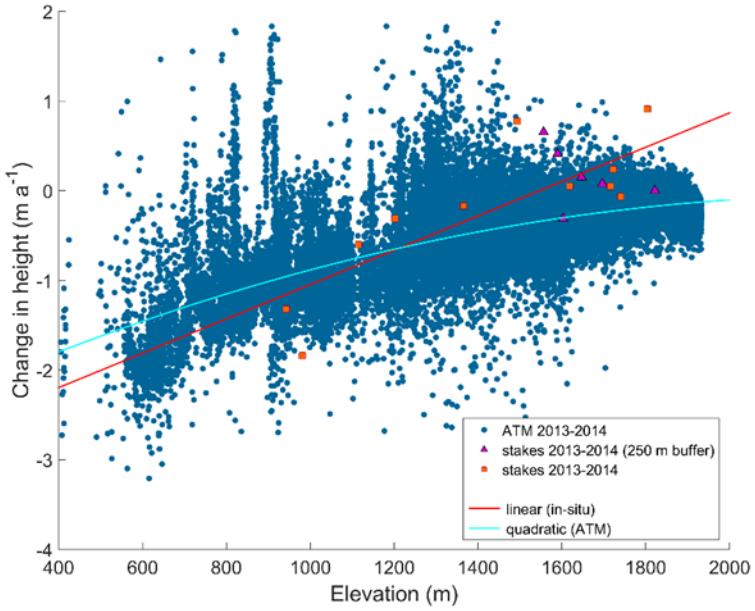

Statistic	Mass balance stakes	ATM 2013-2014
Regression type	Linear	Quadratic
Intercept	-2.96	-2.59
Coefficient (z)	0.0019	0.0022
Coefficient (z^2)		-4.65×10^{-7}
Adjusted R^2	0.58	0.46
p-value	<0.001	<0.001

Figure 2.6: ATM altimetry surface elevation changes ($\dot{h}$; blue dots) over PIC for: a) 2005-2013 and b) 2013-2014, compared with in situ measurements of surface height change due to mass balance ($\dot{h}_b$; red squares and purple triangles, which indicate measurements within 250 m horizontally of the 2005-2013 NASA data). Least squared best-fit lines are shown for the mass balance and ATM altimetry datasets. The associated regression coefficients for elevation (z) against the change in height ($\dot{h}_b$ for in situ mass balance stake data or $\dot{h}$ for ATM data) are provided in tables adjacent to each plot.

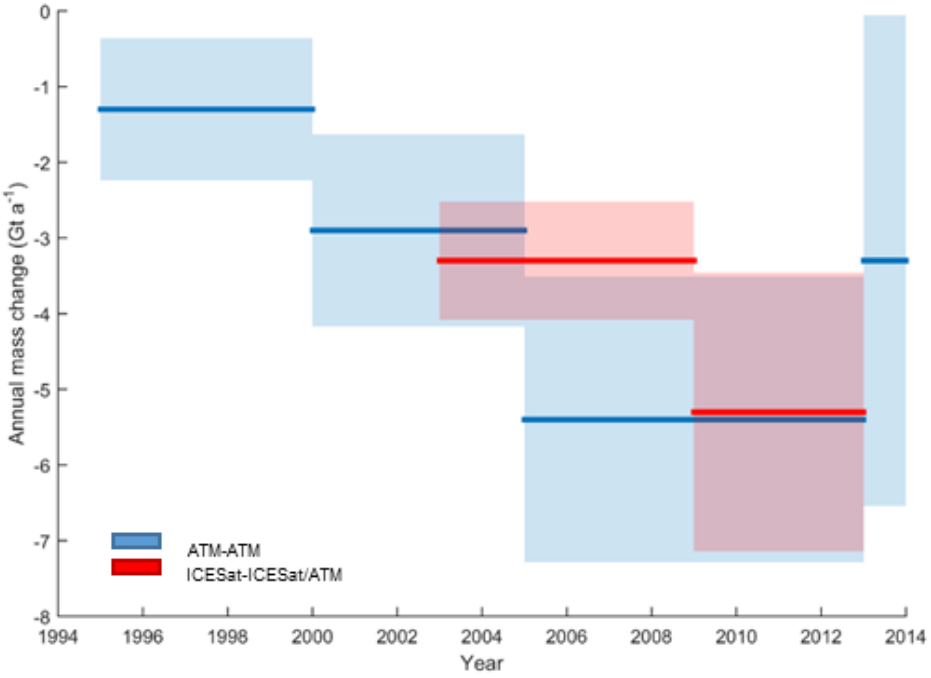

Figure 2.7: Estimates of mass change rates over PIC from 1995-2014 with 95% confidence intervals (shaded portion), uncorrected for firn densification or vertical ice motion. Estimates in blue are ice-cap-wide mass loss rates derived from ATM altimetry measurements (1995-2005 from *Gardner et al.* [2012]; 2005-2014 from this study). The 2003-2009 estimate in red is from ICESat data only (from *Gardner et al.*,2012), whereas the 2009-2013 estimate is derived for this study from a combination of ICESat (2009) and ATM altimetry data (2013).

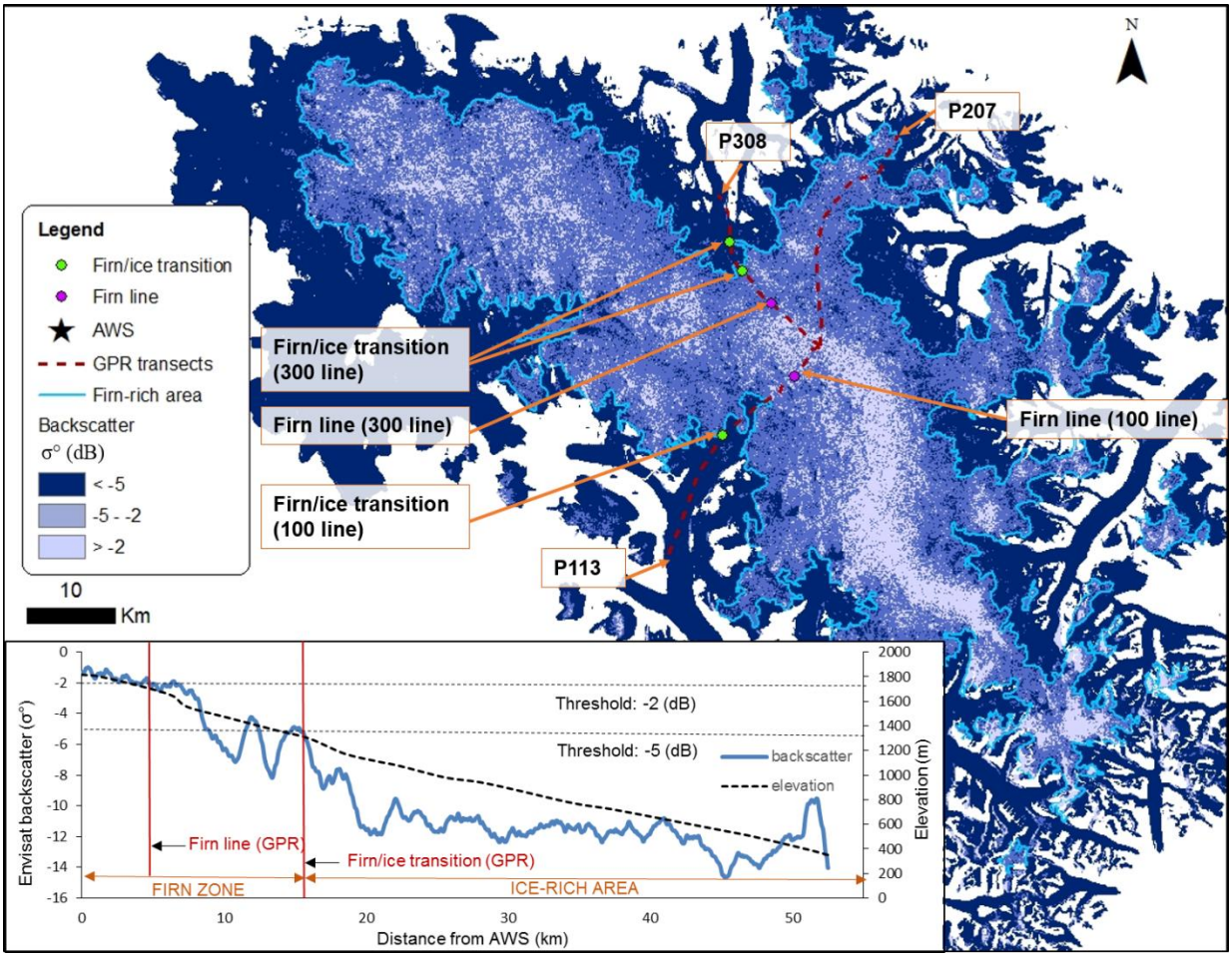

Figure 2.8: Backscatter in Envisat ASAR wide swath image from 19 October 2010 binned into three categories. The firn zone is defined as areas where backscatter is > -5 dB. Location of GPR transects shown in Fig. 2.3 are marked by red dotted lines, and GPR-derived transition locations (firn line and firn/ice transition) are plotted. Inset graph indicates change in Envisat backscatter values along a transect from the AWS to P113. Firn line and firn/ice transition points labeled on the map are marked with a red line.

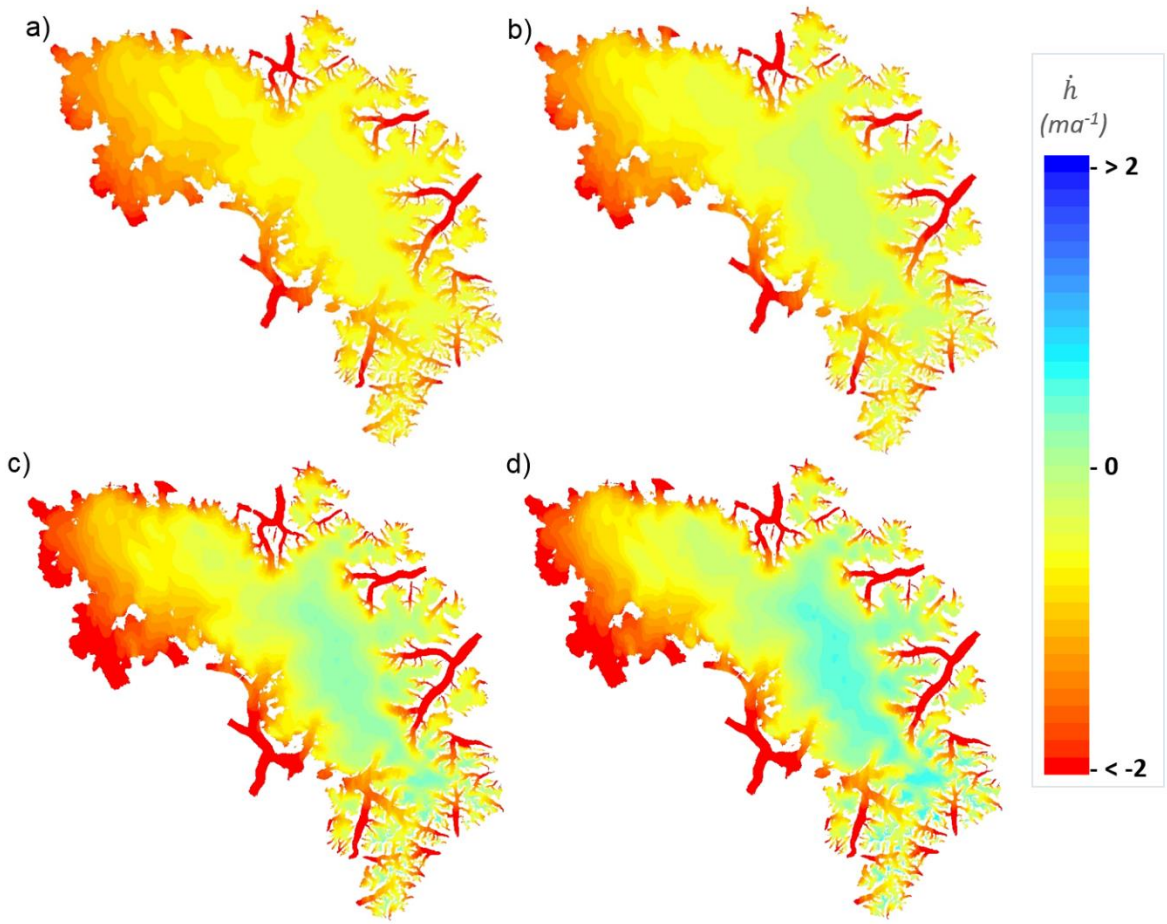

Figure 2.9: (a) Extrapolated 2005-2013 NASA $\dot{h}$ data over PIC, (b) corrected for firn densification ($\dot{h}_{dens}$), (c) corrected for dynamics ($\dot{h}_{dyn}$), and (d) corrected for both densification and dynamics ($\dot{h}_{dyn\_dens}$).

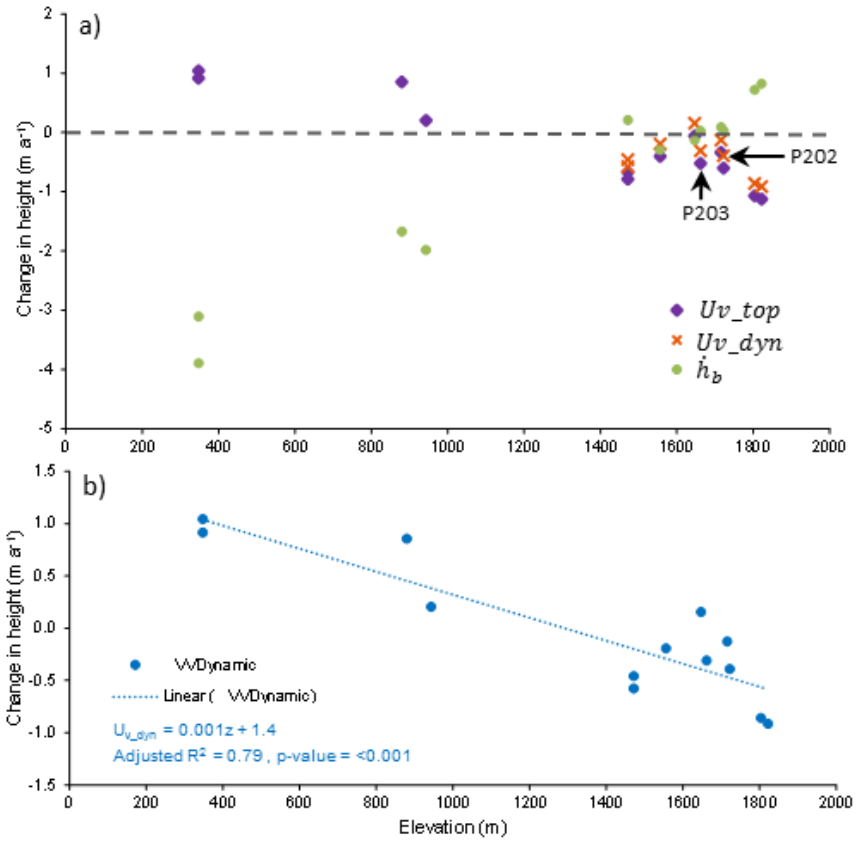

Figure 2.10: Vertical velocity against elevation derived from in situ dGPS measurements: (a) U_{v_top} measured from the top of the stake, U_{v_dyn} adjusted to remove the firn densification component in the firn zone, $\dot{h}_b$ mass balance data from corresponding stake locations (all stake locations, except for P202 and P203, are along the 100 line transect; Table 2.2); (b) vertical velocities (U_{v_dyn}) with a least squares best fit linear regression line.

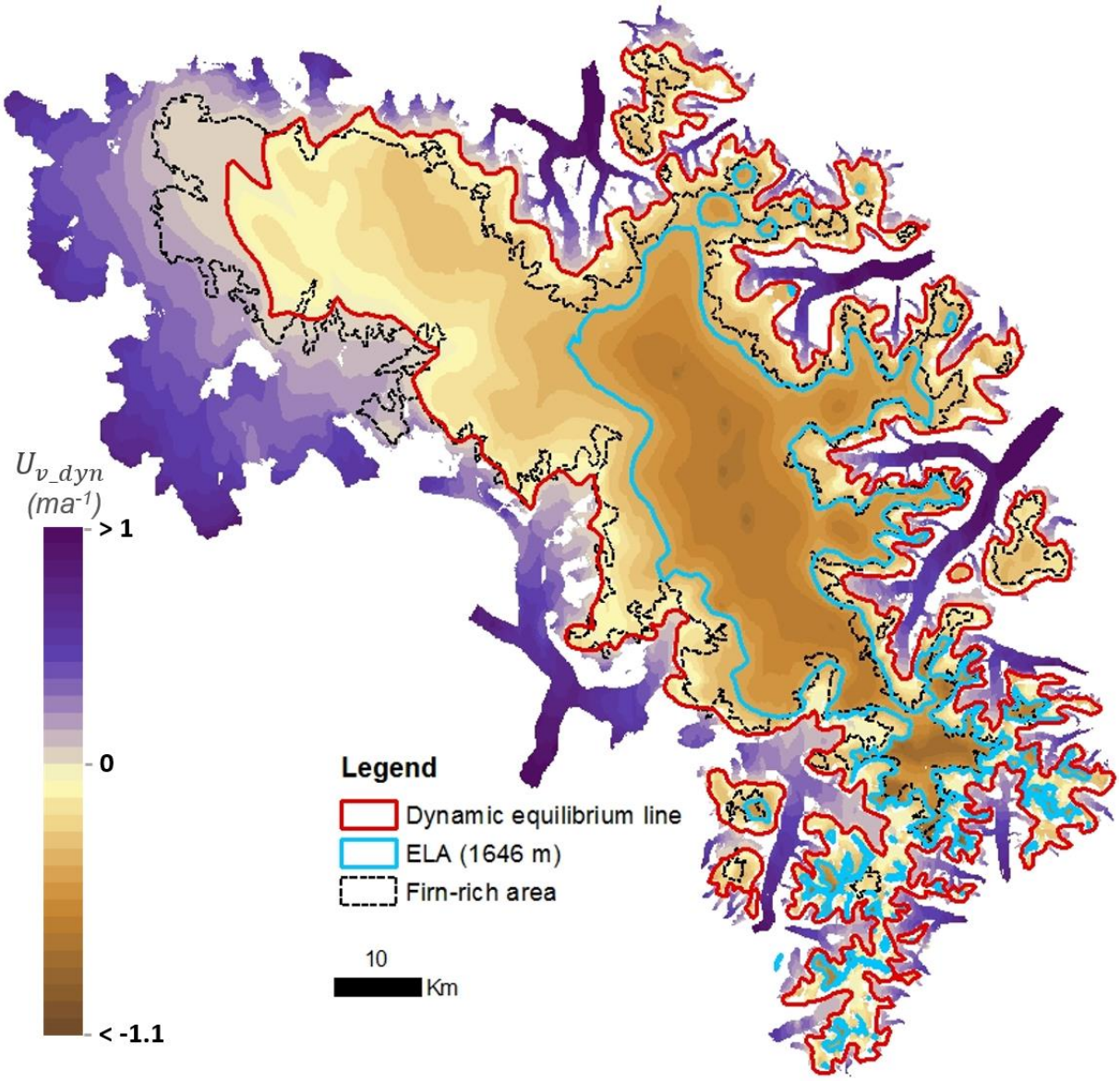

Figure 2.11: Calculated dynamic component of vertical velocity (U_{v_dyn}) showing the dynamic equilibrium line (U_{v_dyn}= 0), ELA and firn zone boundary for reference. U_{v_dyn} was calculated from in situ stake measurements of U_v extrapolated across the ice cap using the CDED DEM.

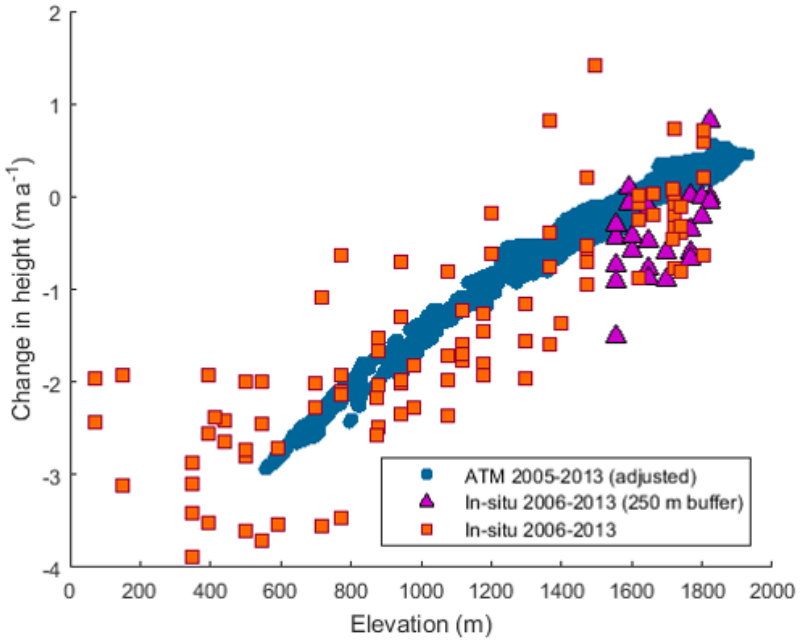

Figure 2.12: ATM altimetry elevation change from 2005-2013 (blue dots) adjusted for both densification and dynamics against elevation. In situ surface mass balance measurements are included for reference with measurements within 250 m horizontally of the 2005-2013 NASA cloud shown as purple triangles.

CHAPTER 3: ICE VELOCITY CHANGES ON PENNY ICE CAP, BAFFIN ISLAND, SINCE THE 1950s

ABSTRACT

Predicting the velocity response of glaciers to increased surface melt is a major topic of ongoing research with significant implications for accurate sea level rise forecasting. In this study we use optical and radar satellite imagery, as well as comparisons with historical ground measurements, to produce a multi-decadal record of ice velocity variations on Penny Ice Cap, Baffin Island. Over the period 1985-2011, the six largest outlet glaciers on the ice cap decelerated at an average rate of 21 m a^{-1} over the 26 year period (0.81 m a^{-2}), or 12% per decade. The change was not monotonic, however, as most glaciers accelerated until the 1990s, then decelerated. A comparison of recent imagery with historical velocity measurements on Highway Glacier, on the southern part of Penny Ice Cap, shows that this glacier decelerated by 71% between 1953 and 2009/11, from 57 m a^{-1} to 17 m a^{-1}. The recent slowdown of outlet glaciers has coincided with increases in mass loss, terminus retreat and an inferred reduction in basal sliding. Measured decelerations are greater than the total short-term variability measured from both seasonal and interannual fluctuations, and supports the hypothesis that glacier thinning and/or increased meltwater production promotes a long-term reduction in ice motion.

3.1 INTRODUCTION

Anomalously high summer temperatures over the last few decades have resulted in sharply increased mass loss of glaciers and ice caps in the Canadian Arctic Archipelago (CAA), particularly since 2005 [*Gardner et al.*, 2011; *Harig and Simons*, 2016]. Baffin and Bylot Islands lost ice mass at an area-averaged rate 1.6 times greater than glaciers in the northern CAA between 2003-2009 [*Gardner et al.,* 2012]. Projections by a coupled atmosphere/snow model forced with the IPCC's moderate RCP4.5 greenhouse gas emission scenario forecasts sustained and irreversible glacier mass losses in the CAA, increasing from -51 ± 26 Gt a^{-1} over 2000-2011 to -144 ± 33 Gt a^{-1} by the end of the 21st century, resulting in a projected 18% loss of the current ice volume [*Lenaerts et al.,* 2013].

A major unresolved question in assessing the response of Arctic glaciers to climate change is whether they will speed up or slow down in response to increased surface melt. Observations of short-term high velocity events on the Greenland Ice Sheet (GIS) in summer [*Zwally et al.*, 2002] have led to concerns that accelerated ice motion may occur as the climate warms and surface melt increases. In turn, this could produce dynamic thinning [*Alley et al.*, 2005] and greater drawdown of ice from the interior, resulting in a greater sensitivity to future warming [*Parizek and Alley*, 2004]. Several studies support the short-term speedup mechanism initially proposed by *Zwally et al.* [2002], in that rapid drainage of surface meltwater to the ice-sheet bed results in an over-pressurized basal drainage network, reduced basal friction and a short-term increase in ice motion. For example, *Bartholomew et al.* [2012] measured pronounced multiday speed-up events believed to be forced by rapid variations in meltwater input into the subglacial system from diurnal and weather-related fluctuations. Similarly, *Fitzpatrick et al.* [2013] measured continued acceleration at Russell Glacier, Greenland, during periods of melt well in excess of the critical rate proposed by *Schoof* [2010] for the formation of subglacial channels. These findings build on earlier studies that found similar positive relationships between melt and short-term velocity variations on temperate and polythermal valley glaciers, such as *Iken* [1981], *Nienow et al.* [1998], *Copland et al.* [2003b] and *Mair et al.* [2003].

However, other recent studies indicate that the relationship between increased surface melt and glacier velocities is not straightforward. For example, *Sundal et al.* [2011] found a positive correlation between surface melt and peak velocities for land-terminating glaciers in southwestern Greenland over a five year period, but that mean summer velocity was lower during high melt years. A slow-down occurred when a critical amount of meltwater entered the ice sheet, causing a switch to a channelized subglacial drainage network. In years with increased surface melting this switch occurred earlier in the summer, resulting in a lower summer ice velocities compared to years with less melt. Simulations using a hydrological model of subglacial drainage system evolution performed by *Schoof* [2010] support this pattern as they show that when subglacial water inputs exceed a critical rate of ~1.4 cm d^{-1}, subglacial channelization occurs rapidly. Other studies have also identified a relationship between high summer melt and the evolution of a more efficient subglacial drainage system, which results in lower velocities the following winter [*Burgess et al.*, 2013; *Sole et al.*, 2013; *Tedstone et al.*, 2013]. Long-term (>= 8 years) ice motion measurements from a land-terminating region of the

western GIS [*Tedstone et al.*, 2015] and many other non-surging glaciers elsewhere [*van de Wal et al.*, 2008; *Heid and Kääb*, 2012b; *Waechter et al.*, 2015] also reveal decreasing ice velocities despite an overall increase in temperature and surface melt rates.

In the northern CAA, *Van Wychen et al.* [2016] found a deceleration of several major tidewater-terminating glaciers since ~2011, but two more than doubled their speed between 1999-2015, and now account for ~62% of the total dynamic (iceberg) discharge from all ice masses in the northern CAA. Other measurements in the same region have identified ice velocity variations on timescales of years to decades, some of which are related to glacier surging (e.g. *Copland et al.*, 2003; *Williamson et al.*, 2008; *Van Wychen et al.*, 2012, 2014). Together, these studies indicate that glacier velocities vary considerably across the Canadian Arctic, but it is currently unclear if observed long-term variations are related to contemporary changes in climate. Large Arctic ice masses can take hundreds of years to respond dynamically to a change in mass balance [*Oerlemans*, 2005], so it is possible that the recent changes in ice motion may represent a delayed response to climate variations in the distant past, rather than an immediate response to current changes in surface melt rates. Understanding this connection is important for projecting future changes in ice motion, and resulting glacier mass changes.

In this study, we present a multi-decadal record of ice velocity variations since the 1950s on Penny Ice Cap (PIC), the largest land ice mass on Baffin Island, using optical and radar remote sensing imagery updated to 2014, as well as comparisons of these data with earlier, historical field measurements. In an earlier study, *Heid & Kääb* [2012b] used repeat satellite optical imagery to assess velocity changes for parts of 12 outlet glaciers on PIC between 1985 and 2011. The present study examines velocity variations across the whole of PIC in much greater detail over the same period by producing a complete ice-cap-wide velocity map for 2011/2012 and mapping ice motion along the centre flow line and several transverse profiles for key outlet glaciers, rather than over at limited set of point locations, as was done by *Heid & Kääb* [2012b]. The acquired velocity data are also compared to in situ mass balance data, and to estimates of ice mass loss obtained with a time-varying mass balance model. These comparisons provide insights into the causes and patterns of ice velocity variability on one of the largest ice caps in the CAA over the past 30-60 years.

3.2 STUDY SITE

PIC (67°N, 66°W) is the southernmost large Canadian Arctic ice cap, covering an area of ~6300 km^2 (Fig. 3.1). Higher topography and relief dominate the eastern side of the ice cap, which reaches a maximum elevation of ~1930 m at its summit. Toward the west, elevations decrease gradually and PIC terminates in a broad, gently sloping lobe-like region. Major outlet glaciers radiate from the ice cap interior through deeply-incised valleys toward the north, east and south. Two of these outlet glaciers are tidewater terminating: Coronation Glacier in the south-east, and an unnamed glacier in the north-central sector (Glacier 3). These glaciers discharge ~11 and ~9 Mt a^{-1}, respectively [*Van Wychen et al.*, 2015], which accounted for ~0.2% of the total mass loss over PIC in 2011. The mean, maximum and minimum air temperatures measured by an automatic weather station (AWS) at the PIC summit between Aug. 1 2007 – July 31 2008 were -15.4°C, 2.9°C and -42.9°C, respectively. Annual surface mass balance (SMB) measurements have been conducted on PIC since 2006 along three survey lines (designated 100, 200 and 300; Fig. 3.1). Based on these measurements, the mean equilibrium line altitude (ELA) between 2006-2014 was ~1646 m, varying between ~1320 m in low mass loss years to 1820 m during high mass loss years. The average surface mass balance along the 100 survey line (Fig. 3.1) which covers an elevation range of 329 m to 1817 m, was -1.3 m w.e. a^{-1} between 2007-2014, but varied from -0.8 to -1.7 m w.e. a^{-1} during low and high mass loss years, respectively. The maximum ice thickness measured on PIC by a NASA airborne radar in 2013 was 880 m, ~5.5 km northwest of P106 [*Shi et al.*, 2010]. The average dates for the onset and end of the summer melt period between 2007-2010, determined from passive microwave data, were ~May 23rd and ~September 3rd, respectively (F. Dupont, personal communication, 2015). According to these same data, the average melt season length on PIC nearly doubled between 1979 and 2010 [*Zdanowicz et al.*, 2012]. Examination of shallow cores also show that the mean density in the accumulation area of the ice cap has been increasing since the mid-1990s due to the formation of thick infiltration ice layers in the firn. Deep meltwater percolation has caused the 10 m firn temperatures to rise by ~10°C between the mid-1990s and 2011. In situ SMB measurements from 2007-2011 indicate thinning rates of 3-4 m a^{-1} near the ice cap margin, which are amongst the largest rates reported in the Canadian Arctic [*Zdanowicz et al.*, 2012].

The first ice velocity measurements on PIC were carried out by the Arctic Institute of North America (AINA) using a theodolite during July and August 1953 at 8 mass balance stakes on Highway Glacier [*Baird*, 1953]. Surface velocity was also inferred from the location of a moraine on 1948 air photos and field observations in 1953. These studies showed that Highway Glacier was moving at ~60 m a^{-1} in the early 1950s. Between 1962-1965, surface velocities measured near the current location of the summit AWS (Fig. 3.1) were found to be just over ~1.3 m a^{-1} [*Weber and Cooper*, 1993]. The first ice-cap-wide assessment was completed by *Heid & Kääb* [2012] using approximately annually separated optical satellite image pairs from late summer (July or August) from 1985/1987 and 2009/2010 over parts of 12 outlet glaciers. Their results showed a mean decrease in ice motion of 25% per decade, with the greatest change of more than -20 m a^{-1} on Coronation Glacier, Glacier 1 and Glacier 4 (Fig. 3.1). *Heid & Kääb* [2012] also investigated ice motion during an intermediate period (1997/1998) and found that speeds had increased by 1.5 m a^{-1} since 1985/87, then decreased by 11.3 m a^{-1} by 2009/2010. A more recent study by *Van Wychen et al.* [2015] used speckle-tracking of winter 2010-2011 ALOS PALSAR Synthetic Aperture Radar satellite data to show that the interior and the western sectors of PIC are slow-moving (<40 m a^{-1}). Topographically constrained outlet glaciers that connect with large areas of accumulation in the interior had the highest velocities, ranging from ~100-120 m a^{-1}, with the fastest movement in areas of highest relief. In contrast to Barnes Ice Cap (central Baffin Island) and Bylot Island Ice Caps, none of the outlet glaciers on PIC appear to be surge-type [*Van Wychen et al.*, 2015], making this ice cap a more suitable site to investigate the relationship between climate and ice motion.

3.3 DATA AND METHODS

In this study, we calculated surface ice velocity on PIC for each decade from the mid-1980s to 2014 via feature tracking of approximately annually-separated optical satellite imagery and, for winter 2011/2012, via speckle tracking of RADARSAT-2 data. The seasonal and interannual variability was quantified (section 3.3.5), and ice velocity changes were compared to mass balance changes (section 3.3.6). In addition, we compared our measurements to those made on Highway Glacier in the 1950s (section 3.5).

3.3.1 *Feature tracking (optical imagery)*

Surface velocities on PIC were derived from the mid-1980s to 2014 by comparing pairs of late summer (July 9th – Sept 1st), cloud-free images from both Landsat TM (30 m resolution) and ETM+ (15 m resolution). Whenever possible, the higher resolution ETM+ imagery was used (Table 3.1). Images approximately 1 year apart were preferentially selected to minimize the effect of seasonal velocity fluctuations on estimates of mean annual displacement. All Landsat images were downloaded from the United States Geological Survey data portal (http://earthexplorer.usgs.gov) in orthorectified (Level 1T) format, and image pairs were always matched with the same path and row to minimize distortion errors. Feature tracking requires good visual contrast in the images, so the analysis was generally restricted to the ablation area and crevassed parts of the accumulation area.

Features visible in two Landsat images were tracked using automatic matching of image pairs with a cross-correlation method that operates in the frequency domain (CCF-O), called orientation correlation [*Fitch et al.*, 2002]. This method performed best in a global evaluation of glacier feature tracking methods that are effective on striped Landsat 7 images [*Heid and Kääb*, 2012a]. The outer portions of Landsat 7 images are striped from May 31 2003 onwards due to the failure of the scan line corrector (SLC-off) (http://www.lta.cr.usgs.gov/LETMP). The image correlation software CIAS [*Kääb and Vollmer*, 2000; *Heid and Kääb*, 2012a], which includes CCF-O, was used for the optical image analyses (http://www.mn.uio.no/geo/english/research/projects/icemass/cias).

CCF-O converts Landsat images to *oriented images*, where each pixel is a complex number that represents the orientation of the intensity gradient [*Fitch et al.*, 2002; *Heid and Kääb*, 2012b]. The oriented images are matched by systematically correlating a block of pixel values in the first image with the same size block moved repeatedly within a larger window size in the second image. Cross-correlation is operated in the frequency domain and a cross-correlation surface representing matches between the reference block (first image) and block position within the window in the second image is produced. The peak of this cross-correlation surface represents the best match from which the displacement between the blocks is calculated

We determined an optimal image matching block size and Landsat band for each image pair after testing various options on a trial area of ~40 km^2 (Fig. 1; Table 3.1). A search area twice the

block size and a velocity vector spacing of 120 m was used for all image pairs. Point velocity mismatches were removed from the dataset (section 3.3.3) and the remaining vectors were interpolated to a raster with 120 m grid spacing using the point to raster conversion tool in ArcMap 10.3.1. Velocities along centre flow line and transverse profiles on the major outlet glaciers of PIC were extracted from the rasters for every decade of the study period to illustrate changes in ice motion through space and time.

3.3.2 *Speckle tracking (radar imagery)*

To investigate the variability in ice motion in areas where optical image matching does not work (e.g., accumulation area), we produced an ice-cap-wide map of glacier motion from speckle tracking of RADARSAT-2 data. Scenes were acquired from the Canadian Space Agency every 24 days between February 5 to April 28 2011 and March 13 to April 26 2012. Images from a period of below-freezing conditions (hereafter: "winter") were selected to maximize coherence, which can be hampered when there is surface melt or snowfall between scenes. In total, 11 image pairs from 2011 (fine beam; 8 m resolution) and 5 image pairs from 2012 (ultrafine beam; 3 m resolution) were used to cover the entire ice cap (Table 3.2; Fig. 3.1).

Ice surface motion was determined using a custom-written Matlab speckle-tracking code based on that used by *Short & Gray* [2005], modified to process RADARSAT-2 data [*Van Wychen et al.*, 2014]. The program tracks the relative displacement of small image chips by applying a two-dimensional cross-correlation algorithm to accurately co-registered image pairs (co-registration was completed using an area cross-correlation technique; *Gray et al.*, 2001). If there is good coherence between image pairs, the radar speckle in the two image chips will be correlated and a calculation of relative displacement can be made. If obvious features are present (e.g. crevasses), the program will track the displacement of these features instead [*Short and Gray*, 2005]. Displacements were calculated for both azimuth and range directions using chip sizes of ~453 m in azimuth and ~688 m in range for the fine beam imagery and ~177 m in azimuth and ~188 m in range for the ultrafine beam imagery. The Canadian Digital Elevation Dataset (1:250,000, Level 1) was used to remove the topographic component of the slant-range displacement. Displacements were calibrated using manually selected areas of zero motion, such as bedrock outcrops, to remove systematic biases due to inaccuracies in the baseline or squint effects during image acquisition [*Gray et al.*, 2001].

Final displacements were converted to annual velocities. Image pair results with the least number of mismatches were selected, prioritizing the higher resolution 2012 results for fast flowing areas (Fig. 3.1). Point velocities were filtered to remove mismatches (section 3.3.3), merged into one file and interpolated to 100 m grid spacing using the inverse-distance weighting method with a fixed 500 m search radius in ArcMap 10.3.1. The final raster was clipped to the area of PIC using the outline provided by the Randolph Glacier Inventory version 4.0 [*Pfeffer et al.*, 2014].

3.3.3 *Filtering velocity vectors*

Incorrect matches are occasionally produced by the feature tracking and speckle-tracking algorithms when there are no repeatable patterns to track or if there is a pattern shift not associated with glacier movement. For example, a lack of patterning can occur if there is snow cover present for feature tracking, or if there is a lack of coherence due to snowfall or melt between repeat images used for speckle tracking. Velocity vector outputs from feature and speckle tracking were therefore checked manually and filtered in ArcMAP, following the methodology of Copland et al. (2009), Van Wychen et al. (2014) and Waechter et al. (2015):

(a) The direction of ice motion should follow surface flow features (e.g. medial moraines) and topography where motion is constrained;
(b) The ice motion direction or magnitude should not change dramatically (approximately $\geq 45°$) over short distances;
(c) Motion should generally be faster at the centre of the glacier than at the margins.

The filtering was partially automated by finding the area with the highest velocities in a region of interest (e.g. an outlet glacier) and calculating the 99% confidence interval for the fastest flowing part of the region. Point velocities with a magnitude above the 99% confidence interval were automatically removed. Remaining vectors were then manually filtered using the criteria outlined above and incorrect matches were deleted.

3.3.4 *Error analysis*

The accuracy of the CCF-O matching method is stated as ~1/10 of a pixel [*Heid and Kääb*, 2012a]. In Landsat images, the pixel noise limits the image-to-image registration accuracy of ~5 m for the ETM+ sensor [*Lee et al.*, 2004] and ~6 m for the TM sensor [*Storey and Choate*, 2004]. In this study, the apparent motion of 703,902 points located on unglaciated stable ground

was on average 5.4 m a^{-1}, ranging from 3.5 – 9.2 m a^{-1} depending on the image pair (Table 3.3). We assume that this provides a representative error for our study, and encompasses the effects from all sources. This error level enables an effective determination of glacier motion since the speed of most outlet glaciers on PIC (~100-120 m a^{-1}) far exceeds this amount.

Errors associated with the speckle tracking method and associated cross-correlation technique are discussed in *Gray et al.* [2001], *Joughin* [2002], *Short & Gray* [2004] and *Van Wychen et al.* [2012]. For 24 day repeat imagery with good coherence, speckle tracking provides velocity errors of 2-10 m a^{-1} in the Canadian Arctic [*Short and Gray*, 2005]. In heavily crevassed, faster-flowing regions, the program switches to feature tracking with errors of ~10-20 m a^{-1} [*Short and Gray*, 2005]. Based on 130,727 measurements of apparent motion over bedrock areas, our error analysis for speckle tracking of RADARSAT-2 data was on average 5.6 m a^{-1}. For 13,233 measurements along ice divides where zero motion was assumed, the average error was 10.4 m a^{-1} (Table 3.3). Ice divides delineated in version 4.0 of the Randolph Glacier Inventory were used for this analysis.

3.3.5 *Seasonal and interannual variability*

Glacier motion varies seasonally and from year to year in response to short-term fluctuations in meltwater availability, among other factors. To evaluate if the observed long-term (decadal) velocity changes exceeded the short-term variability, we quantified this variability on interannual and seasonal time scales.

The interannual variability was calculated from in situ dual-frequency GPS (dGPS) measurements collected between 2011-2014 along three mass balance transects (Fig. 3.1; Table 3.4) and optical matching of Landsat images from 2008-2014 (Table 3.1). Velocities measured using these methods along a glacier centre flow line profile were used to compute the standard deviation (σ), corrected for the total number of measurements (n) at each location. The 95% confidence interval, representing the interannual variability, was then calculated from $1.96(\sigma/\sqrt{n})$.

To determine seasonal variability, we computed the difference between the annual motion derived from the in situ dGPS measurements and the winter synthetic aperture radar (SAR) velocities derived from the RADARSAT-2 (2011/2012) data processed for this study and from

the ALOS PALSAR (2010/2011) data processed by *Van Wychen et al.* [2015]. The SAR velocity values at each dGPS measurement location were extracted and the difference between the annual dGPS and winter SAR velocities standardized to annual values were calculated. The total short-term variability was then calculated from the root sum of squares of the interannual and seasonal variability.

3.3.6 *Mass balance*

To assess potential controls on long-term variations in ice motion, we calculated annual in situ SMB from the 100 survey line between 2007-2014 (Fig. 3.1), and also used estimated SMB outputs from 1958-2014 from the regional atmospheric climate model RACMO2.3 [*Lenaerts et al.*, 2012; *Noël et al.*, 2015]. The RACMO2.3 model is forced by the most recent reanalysis data from the European Centre for Medium-Range Weather Forecasts, called ERA-interim. It includes a scheme for snow redistribution, and outputs SMB data at a grid resolution of 11 km.

We assessed how well the model represents measured mass balance at PIC by extracting RACMO2.3 SMB at grid cells overlapping each 100 line stake over the period 2007-2014. SMB measurements along this line were averaged for in situ and RACMO2.3 data and plotted against time (Fig. 3.2). We found that the RACMO2.3 data captured the interannual variability of SMB well, but underestimated the actual magnitude of mass loss. This is likely due to the model averaging of elevation over each 11 km grid cell, which leads to an overestimation of the mean elevation for grid cells with low-lying outlet glaciers, where melt rates are greatest (B. Noel, personal communication, 2016). We therefore multiplied the RACMO2.3 SMB data by a correction factor of 1.92, which provided the best match to the in situ measurements (r value = 0.89) (Fig. 3.2). The ice-cap-wide average SMB was extracted for all grid cells covering PIC and the output was similar in magnitude to the 2007-2014 measurements extrapolated from the 100 survey line, and captured the interannual variability well, providing confidence that our RACMO2.3 SMB provides an effective way to derive the ice-cap-wide SMB since the 1950s.

3.4 RESULTS

3.4.1 *Ice-cap-wide velocity patterns*

The SAR-derived velocity map of PIC shows that most of the ice cap is slow-moving (<20 m a^{-1}), particularly in high elevation regions in the accumulation area, with faster motion limited to topographically constrained outlet glaciers (Fig. 3.3). The highest velocities occur in areas of high relief on the upper reaches of outlet glaciers and range from ~100 - 250 m a^{-1}. Low velocities over much of PIC suggest that the ice is frozen to the bed and flowing by internal deformation only, whereas areas of increased velocity likely represent a transition from cold to warm basal conditions as the ice is channeled into topographically constrained valleys [*Burgess et al.*, 2005; *Van Wychen et al.*, 2016].

3.4.2 *Velocity changes through time*

The annual velocities derived from optical image matching showed clear patterns and temporal changes over most of the major outlet glaciers (Fig. 3.4, Fig. 3.5). Individual velocity vectors aligned well with glacier flow features, such as medial moraines, which provides confidence in the results (Fig. 3.4 insets). To illustrate the patterns, centre flow line velocities were extracted for the ablation area of the six outlet glaciers with best coverage between 1985-2014: four land-terminating (Glaciers 1, 4, 8, 11) and two tidewater-terminating (Glaciers 3, 6) (Fig. 3.3, 3.5). For most glaciers, velocities were highest near the top of their ablation areas. The main exception was Glacier 11, which had relatively low overall velocities and did not have a distinct area of high velocity up-glacier. On Glaciers 1, 3 and 6 there was a noticeable decrease or leveling of velocities at 20 km, 15 km and 17 km from the terminus, respectively, associated with an area of relatively flat topography. On Glacier 3, the large peak in velocity at ~17 km likely arose due to the merging of a tributary with the main glacier trunk. Tidewater-terminating glaciers showed a pronounced increase in velocity at their termini, while land-terminating glaciers showed decreasing velocities at their termini.

Most glaciers showed clear changes over time. For example, velocities over the majority of the ablation area of Glacier 1 showed a significant decrease between 1985/1987 and 2013/2014 (Fig. 3.4). When analyzed in more detail, however, it is clear that the glacier velocity changes were not uniform through the study period. For all glaciers except Glacier 6, velocities increased from 1985/1987 to 1997/1998, and decreased thereafter. For example, Glacier 1 velocities increased

by an average of 13.0 m a^{-1} between 1985/1987 to 1997/1998, and decreased by 34.5 m a^{-1} or 41% between 1997/1998 to 2009/2010. On Glacier 4, velocities increased by 9.9 m a^{-1} in the first 12 year period and decreased by 32.4 m a^{-1} or 44% in the second 12 year period. In contrast, velocities on Glacier 6 decreased by 6.2 m a^{-1} in the first period and further decreased by 19.7 m a^{-1} or 31% in the second period.

For the three glaciers with the most complete velocity records, this temporal variability is illustrated in Figure 3.6. In general, velocities initially increased until 1998, and decreased thereafter for the two land-terminating glacier (Glaciers 1 and 4) and also between 25 and 35 km upglacier from the terminus of Glacier 6. Lower portions of Glacier 6 showed a different pattern, with decreasing velocities from 1985 to 2014 between 5 and 25 km from the terminus, and an increase in velocities after 1998 within 5 km of the terminus. For all six glaciers, the overall velocity trend from 1985 – 2011 was negative. This deceleration has coincided with 1985-2014 terminus retreat of land-terminating glaciers of 178 m, 380 m, 840 m and 939 m for Glaciers 1, 4, 8 and 11, respectively, and retreat of tidewater-terminating glaciers of 973 m and 820 m for Glaciers 3 and 6, respectively.

Transverse profiles for the upper, middle and lower sections of the ablation area of three glaciers (Glaciers 1, 8, 6) showed an increase in motion between 1985/1987 to 1997/1998, followed by a decrease thereafter (Fig. 3.7). The transverse profiles also aid in identifying the relative importance of basal sliding vs internal deformation. Where basal sliding dominates, ice tends to move with high and relatively constant velocities near the glacier centre and velocities decrease rapidly close to the margins [*Kamb et al.*, 1985; *Fatland et al.*, 2003; *Copland et al.*, 2009]. This has been termed *blockschollen* (or plug flow) by *Kick* [1962]. In contrast, lower velocities with a gradual reduction in flow with distance from the centre flow line in a parabolic shape are more likely to represent motion dominated by internal ice deformation. On Glaciers 1 and 6 in higher velocity years (e.g. 1997/1998) and higher velocity areas (e.g. upper cross section), the transverse patterns show a rapid decrease in velocity near the glacier margins typical of flow dominated by basal sliding. In contrast, lower velocity years and locations are characterized by a more parabolic transverse profile typical of flow dominated by ice deformation. Glacier 8 maintains a block type flow from 1985-2011 in its upper and middle regions.

3.4.3 *Total short-term velocity variability*

To quantify the interannual variability of ice motion, we compared annual in situ dGPS measurements collected within 500 m of the centre flow line on Glaciers 1 and 6 with the optical feature tracking results (Fig. 3.8). All dGPS points showed comparable velocities to the nearest centre flow line point (< 4 m a^{-1} difference calculated from the RADARSAT-2 velocity results for each location), with the exception of the points near the terminus of Glacier 1 which were ~ 7-10 m a^{-1} slower than the nearest centre flow line location. The estimated mean 95% confidence interval for interannual velocity variations on Glaciers 1 and 6 were ± 8.9 m a^{-1} and ± 3.7 m a^{-1}, respectively. The minimum confidence interval for Glacier 1 was found at the terminus, and for Glacier 6 it was ~10-25 km from the glacier terminus.

To calculate the seasonal variability, speckle tracking velocities were extracted along a transect that started at each glacier terminus and connected the dGPS points (Fig. 3.9, Table 3.4). The average difference between all the dGPS annual point velocities and SAR-derived winter velocities at the same location was 2.2 m a^{-1} (st. dev. = 8.0 m a^{-1}) for Glacier 1. This figure is within the error limits of the SAR data (± 5.6 m a^{-1}), indicating that there was no significant difference between winter and annual velocities for this glacier. In contrast, on Glacier 6 the differences averaged -10.0 m a^{-1} (st. dev. = 12.4 m a^{-1}) which was outside of the SAR error limits, indicating that winter velocities were significantly lower than annual velocities on this glacier. The deviation between winter and annual velocities was greatest in the centre of Glacier 6, ~10-25 km from the terminus.

The total short-term variability was estimated from the root sum of squares of the seasonal and interannual variability. For land-terminating Glacier 1, this was ± 8.9 m a^{-1} and for tidewater-terminating Glacier 6 it was ± 12.9 m a^{-1}.

3.5 DISCUSSION

Between 1985-2014 all six PIC outlet glaciers decelerated. The mean deceleration for the four land-terminating glaciers (-25.5 m a^{-1}) and for the two tidewater-terminating glaciers (-20.3 m a^{-1}), exceeded the recent short-term variability in motion observed for these glaciers (8.9 m a^{-1} and 12.9 m a^{-1}, respectively). All glaciers except Glacier 6 accelerated from 1985/1987 to

1997/1998, and all decelerated from 1997/1998 and 2009/2011. The velocity changes in the first 12 year period for all six glaciers were within the range of total short-term variability, whereas the changes in the second 12 year period exceeded the short-term variability for Glaciers 1, 4, 6 and 11. When averaged over all glaciers, velocity changes in the second period exceeded the short-term velocity variability for both land (-23.6 m a^{-1}) and tidewater-terminating (-14.5 m a^{-1}) glaciers.

Ward [1955] calculated the speed of Highway Glacier (Glacier 8) to be 57 m a^{-1} in 1953 from eight stake measurements at 760 m a.s.l. made over a 38 day period during July and August (Fig. 3.3, 3.10). He also calculated annual ice motion from the change in position of a moraine (situated between stakes A and B; Fig. 3.10) between 1948 air photos and 1953 field measurements. A mean annual ice velocity of 60 m a^{-1} was calculated from this analysis, which compared well with equivalent annual speeds of 50 m a^{-1} and 74 m a^{-1} measured at stakes A and B, indicating that the stake measurements were representative of annual motion. Our own measurements show that the average ice motion over these two historical transects slowed by ~71% from 57 m a^{-1} in 1953 to 17 m a^{-1} in 2009/2011, with consistent velocity decreases at all stakes (Fig. 3.10).

This widespread deceleration across PIC between 1985-2014 suggests that the change in ice motion is primarily driven by factors common to all glaciers, rather than local effects such as individual glacier thicknesses, localized slope gradients, or melt patterns. The RACMO2.3 SMB output indicates a general long-term decrease in mass balance (Fig. 3.11), consistent with increases in summer and winter temperature anomalies reported in this region since 1985 [*Zdanowicz et al.*, 2012; *Vincent et al.*, 2015] and increased mass losses over PIC determined from NASA Airborne Topographic Mapper (ATM) altimetry elevation changes from 1995-2013 [*Schaffer et al.*, in review-b]. ATM altimetry changes from 2005-2013 resulted in an estimated mass loss rate of -5.4 ± 1.9 Gt a^{-1}, four times greater than the 1995-2000 rate of -1.3 ± 0.72 Gt a^{-1} estimated by *Gardner et al.* [2012]. Increased melt is also evidenced by a near doubling of the melt feature percent (volumetric percentage of a core occupied by infiltration ice) in the top 6 m of the firn strata near the summit between 2011 and 2013, and by a rapid recent upglacier migration of the ELA (currently at ~1646 m), leading to large areas of remnant firn at elevations >400 vertical meters below the present day ELA [*Schaffer et al.*, in review-b]. Precipitation over

PIC since the 1950s has been relatively constant, so the main driver of mass loss is most likely greater summer melt [*Gardner et al.*, 2012; *Vincent et al.*, 2015].

The connection between ice motion variations and surface mass balance changes is clear when comparing the RACMO2.3 SMB model output to glacier velocities (Fig. 3.11). Between 1985-2014 increasingly negative SMB was associated with an overall decrease in ice motion. Within that time period there was an increase in velocities between 1985-1998 after several years of positive surface mass balance between the late 1960s and late 1970s. This period of positive mass balance coincided with anomalously low regional temperatures in both summer and winter measured at weather stations close to PIC [*Bradley*, 1973; *Zdanowicz et al.*, 2012]. In contrast, after 1998 there was a marked decrease in motion for all glaciers, during a period when there was a 325% increase in mass loss from 280 mm w.e. a^{-1} between 1985-1994 to 1191 mm w.e. a^{-1} between 2005-2014. These patterns suggest that the outlet glaciers of PIC respond quickly to increases in surface melt rates by decelerating, and accelerate in response to mass accumulation at times of positive mass balance.

The transverse velocity profiles at PIC provide insights into the relationships between mass loss and ice motion as they record a transition from block flow associated with high basal sliding rates and high basal water pressure, to motion increasingly influenced by internal deformation and likely lower water pressure as velocities decrease from 1985 to 2014 (Fig. 3.7). This suggests a shift from a distributed to a more efficient channelized subglacial hydrological system as mass loss increases, supporting the findings of *Sundal et al.* [2011] and *Schoof* [2010]. The lack of variability between our winter and annual velocity measurements toward the end of our study period (2009-2014) also supports this contention (Fig. 3.8).

To assess the relative importance of internal deformation at different periods, we used historical and current measurements of ice thickness and surface slope at Highway Glacier [*Ward*, 1955] to compute expected deformation rates using a simplified form of Glen's flow law [*Glen*, 1955]:

$$\dot{\varepsilon} = A\tau^{n_g} \quad (1)$$

Where $\dot{\varepsilon}$ is the strain rate, A is a parameter dependent on the ice temperature, τ is the basal shear stress, and n_g is a constant that describes the flow of a material. The surface velocity due to

creep (U_i) was calculated by replacing τ with the equation for driving stress and integrating with respect to height to obtain:

$$\boldsymbol{U_i = 2A(\rho_i tan\alpha)^{n_g} H} \quad (2)$$

where ρ_i is the density of ice, g is the gravitational constant , α is the surface slope, and H is the ice thickness. These calculations were made for 1953 and 2010 at two stakes closest to the glacier centreline (B and β in Fig. 3.10) using ρ_i = 910 kg m^{-3}, α = 3.5° (measured in 1953), and n_g = 3.3. Measurements of summer ice temperatures near the surface in 1953 at altitudes of 440 m and 1010 m were -5.5°C and -6°C, respectively, so a mean value of -5.75°C was used to calculate A = 0.011 a^{-1} bars$^{-3.3}$. The measured ice thickness on Highway Glacier was 270 m in 1953. The current ice thickness (251.5 m) was estimated from the cumulative SMB obtained by RACMO2.3 over the period 1953-2010, subtracted from the 1953 ice thickness. The calculated values of U_i for Highway Glacier were 21.9 and 16.2 m a^{-1}, respectively, for 1953 and 2010. Based on these results, internal ice deformation would have accounted for 31% of the total centreline surface velocity in 1953 (71.2 m a^{-1}), compared with 72% in 2010 (22.3 m a^{-1}). This suggests that the basal sliding component of glacier motion must have decreased significantly over the 57 year interval. The calculated reduction in surface velocity due to internal deformation of (5.7 m a^{-1}) would only account for 12% of the observed change in total surface velocity of 48.9 m a^{-1}, also suggesting a significant decrease in basal sliding.

Sensitivity analyses were performed with respect to slope and ice temperature. A present-day slope of 3.7° between the two 1953 transects was obtained from the ArcticDEM (http://pgc.umn.edu/arcticdem) based on imagery from 2015. The values of U_i for 1953 and 2010, recalculated with this slope, were 24.6 and 18.1 m a^{-1}, respectively. Velocities were also calculated for ice temperatures 1°C above and below the measured 1953 temperature of -5.75°C with a slope of 3.5°. For these temperatures, the corresponding values of U_i in 1953 would have been 25.1 and 18.5 m a^{-1}, respectively, while in 2010 they would be 19.3 and 14.3 m a^{-1}.

Our long-term velocity results for PIC are consistent with those found by *Heid and Kääb* [2012b], who reported an increase in velocities between 1985/1987 to 1997/1998 and a decrease between 1997/1998 to 2009/2011. Results of the two studies are comparable wherever there is spatial overlap, but we report higher mean velocities due to the greater spatial coverage of our

data. For example, in 1985/1987 we found that the mean velocity over PIC was 53 m a^{-1}, compared to 21 m a^{-1} reported by *Heid and Kääb* [2012b]. We also calculated a deceleration rate of 12% $decade^{-1}$ between 1985-2011, compared to a deceleration of 25% $decade^{-1}$ by *Heid and Kääb* [2012b] over the same period. Our deceleration rate was 15% per decade from 1985-2014, but this excludes Glaciers 8 and 11 as there are no data available during 2013/2014 for these glaciers.

The multi-decadal slowdown pattern found at PIC is similar to that observed over the predominantly land-terminating western margin of the GIS by *Tedstone et al.* [2015], where a 12% decrease in ice velocities was observed in conjunction with a ~50% increase in surface meltwater production between 1985-2014. There, sustained high production of surface meltwater is thought to have been responsible for the observed slowdown due to the expansion of a channelized subglacial drainage system resulting in increased drainage efficiency and lower basal water pressures. As on PIC, thinning only accounted for a small percentage (17-33%) of the slowdown [*Tedstone et al.,* 2015]. Likewise, *Heid & Kääb* [2012b] found that glacierized regions dominated by land-terminating glaciers with negative mass balance experienced decreasing ice velocities over the past few decades, with reported decadal mean decelerations of 43% in the Pamir (50 glaciers studied), 8% in the Caucasus (16 glaciers) and 11% in the Alaska Range (9 glaciers). The same is true for Glacier d'Argentière in France [*Vincent et al.*, 2009], Glacier Universidad in the Andes [*Wilson et al.*, 2016], Franz Josef Glacier in New Zealand [*Anderson et al.*, 2014], White Glacier on Axel Heiberg Island [*Thomson and Copland*, 2017] and the lowermost 10 km of the Kaskawulsh Glacier in the Yukon [*Waechter et al.*, 2015].

3.6 CONCLUSIONS

This study has confirmed that most of PIC is slow-moving (<20 m a^{-1}), with faster motion restricted to areas of high relief where the broad accumulation area in the interior connects to topographically constrained outlet glaciers. Velocities on land-terminating outlet glaciers range from ~100 – 250 m a^{-1} and generally decrease down-glacier. In contrast, tidewater-terminating glaciers showed a distinct increase in velocities in their lower terminus region. The six outlet glaciers examined in detail as part of this study showed an overall deceleration between 1985-2014, with an early period of moderate speedup for most glaciers from 1985/1987 to 1997/1998,

followed by a pronounced slowdown thereafter. The deceleration after 1998, as well as the long-term slowdown over the entire study period (1985 to 2014) for PIC, were beyond the estimated short-term ice motion variability. Historical measurements on Highway Glacier show that velocities there have decreased by 71% since 1953.

We postulate that decreased ice motion on PIC is correlated with increased mass loss and with a transition from motion dominated by basal sliding to movement increasingly influenced by internal deformation. This is confirmed for Highway Glacier, where the estimated rate of internal deformation could only account for 50% of the surface velocity in 1953, but increased to 100% by 2010. Our findings support the hypothesis of *Schoof* [2010] that increased surface melt enhances the formation of an efficient channelized subglacial drainage system, which results in lower basal water pressures and reduced ice velocities. Our results add to the growing body of literature which indicates that the majority of land-terminating glaciers are decelerating in response to a warming climate. The response of tidewater-terminating glaciers is more variable as they are controlled by marine influences and changes in backstress, in addition to changes in ice thickness and subglacial hydrology. On PIC, tidewater-terminating glaciers are decelerating, but this has not been the recent pattern for all tidewater-terminating glaciers in the CAA, where Trinity and Wykeham Glaciers (Ellesmere Island) have more than doubled in speed over the past 15 years [*Van Wychen et al.*, 2016], and neither has it been in Greenland, where widespread acceleration of outlet glaciers occurred in the early- to mid-2000s [*Luckman et al.*, 2006; *Howat et al.*, 2008].

Further work is needed to better confirm the cause of deceleration observed across PIC. Thickness change and ice temperature measurements over the most dynamically active outlet glaciers (e.g. Glacier 1) are required to accurately determine the contribution of internal deformation versus basal sliding to the changes observed. For tidewater-terminating glaciers, measurements of sea surface temperatures and bathymetry in Baffin Bay, as well as continued monitoring of glacier motion and runoff are required.

Table 3.1: Optical image pairs used in this study. Path/row refers to the Landsat Worldwide Reference System 2 (WRS-2). The optimal band and block size used for the velocity matching of each image pair were obtained from a ~40 km^2 test area covering Glacier 1 (see Fig. 3.1 for location).

Sensor	Image t = 1 (YYYY/MM/DD)	Image t = 2 (YYYY/MM/DD)	WRS-2 path/row	Band	Block size
Landsat TM	1985/07/09 & 1985/08/19	1987/07/24	18/13	3	960
Landsat TM	1997/07/19	1998/07/22	18/13	3	720
Landsat ETM+	2001/07/31	2002/08/03	17/13	8	600
Landsat ETM+	2009/07/28	2010/09/01	18/13	8	600
Landsat ETM+	2009/08/06	2011/08/12	17/13	8	600
Landsat ETM+	2013/07/23	2014/07/26	18/13	8	600

Table 3.2: RADARSAT-2 image pairs used in this study. The 2011 imagery is fine beam (8 m resolution), while the 2012 imagery is ultrafine beam (3 m resolution). See Figs. 3.1a and 3.1b for image footprints.

Image t = 1 (YYYY/MM/DD)	Image t = 2 (YYYY/MM/DD)	Image segment
2011/02/08	2011/03/04	2
2011/02/15	2011/03/11	1
2011/02/15	2011/03/11	2
2011/02/15	2011/03/11	3
2011/02/15	2011/03/11	4
2011/03/04	2011/03/28	1
2011/03/04	2011/03/28	3
2011/03/20	2011/04/13	1
2011/03/20	2011/04/13	2
2011/03/21	2011/04/14	1
2011/03/21	2011/04/14	2
2012/03/13	2012/04/06	1
2012/03/15	2012/04/08	1
2012/03/20	2012/04/13	1
2012/03/20	2012/04/13	2
2012/04/06	2012/04/30	2

Table 3.3: Error estimates for surface ice velocities on PIC determined from apparent motion over stationary areas (bedrock (BR) and ice divides (ID)) for both feature tracking (optical imagery) and speckle tracking (SAR). Values represent the average ice motion, while error values are the standard deviation. All values in m a^{-1}.

Imagery	**1985/1987**	**1997/1998**	**2001/2002**	**2009/2010**	**2011/2012**		**2013/2014**
	BR	BR	BR	BR	BR	ID	BR
Optical	9.2 ± 3.6	3.5 ± 5.1	3.9 ± 4.0	4.8 ± 3.7			5.5 ± 4.3
SAR					5.6 ± 4.8	10.4 ±7.9	

Table 3.4: Comparison of displacements derived from in situ dGPS (annual) and satellite derived ice motion (winter) for Glaciers 1 and 6 (location of dGPS stations denoted in Fig. 3.1). The latitude (lat.), longitude (long.), distance from the glacier terminus (dist.), velocities at each stake location (dGPS), corresponding SAR velocity (SAR), and the difference in velocity between the dGPS and SAR data sets (diff.) are provided.

Lat.	**Long.**	**Dist.**	**dGPS (m a^{-1})**		**SAR (m a^{-1})**		**Diff. (m a^{-1})**
(°N)	(°W)	(km)	2011-2012	2012-2013	2010-2011	2011-2012	SAR-dGPS
Glacier 1 (land-terminating)							
67.28	-65.85	57	1.5	2.4	1.8	14.1	6.0
67.25	-65.88	54	1.7	2.4	1.1	11.1	4.1
67.23	-65.91	51	9.0	9.6	9.2	14.0	2.4
67.22	-65.96	49	16.1	16.7	18.9	19.4	2.7
67.21	-65.97	48	20.8	20.7	17.9	22.8	-0.4
67.20	-66.02	45	34.8	35.8	47.9	40.6	9.0
67.18	-66.09	42	-	32.6	-	-	-9.3
67.16	-66.13	39	9.4	-	9.1	44.4	17.3
67.15	-66.16	37	80.9	-	91.6	74.7	2.3
67.13	-66.19	35	102.5	96.6	103.4	84.3	-5.7
67.12	-66.21	33	-	102.1	-	-	-0.5
67.09	-66.23	30	82.7	81.0	82.8	80.2	-0.4
67.07	-66.26	27	80.1	-	84.0	83.7	3.8
67.05	-66.28	25	50.9	-	53.8	39.4	-4.3
66.86	-66.26	2	38.4	34.8	34.4	34.2	-2.3
67.29	-65.85	60	2.3	6.9	6.9	15.1	6.3
67.34	-65.85	65	1.6	-	1.4	4.3	1.3
67.39	-65.83	70	1.6	-	8.0	7.7	6.2
67.42	-65.75	75	1.3	-	7.7	6.4	5.8
67.43	-65.67	79	0.2	2.7	6.7	3.9	3.9
67.47	-65.61	83	-	6.9	7.9	4.3	-0.8
		Mean					**2.2**
Glacier 6 (water-terminating)							
67.03	-65.26	29	91.4	-	105.2	90.9	6.7
67.06	-65.16	23	58.3	-	37.0	39.7	-20.0
67.13	-64.99	11	43.9	-	21.9	29.5	-18.2
67.19	-64.83	2	47.8	-	34.8	44.2	-8.4
		Mean	-	-	-	-	**-10.0**

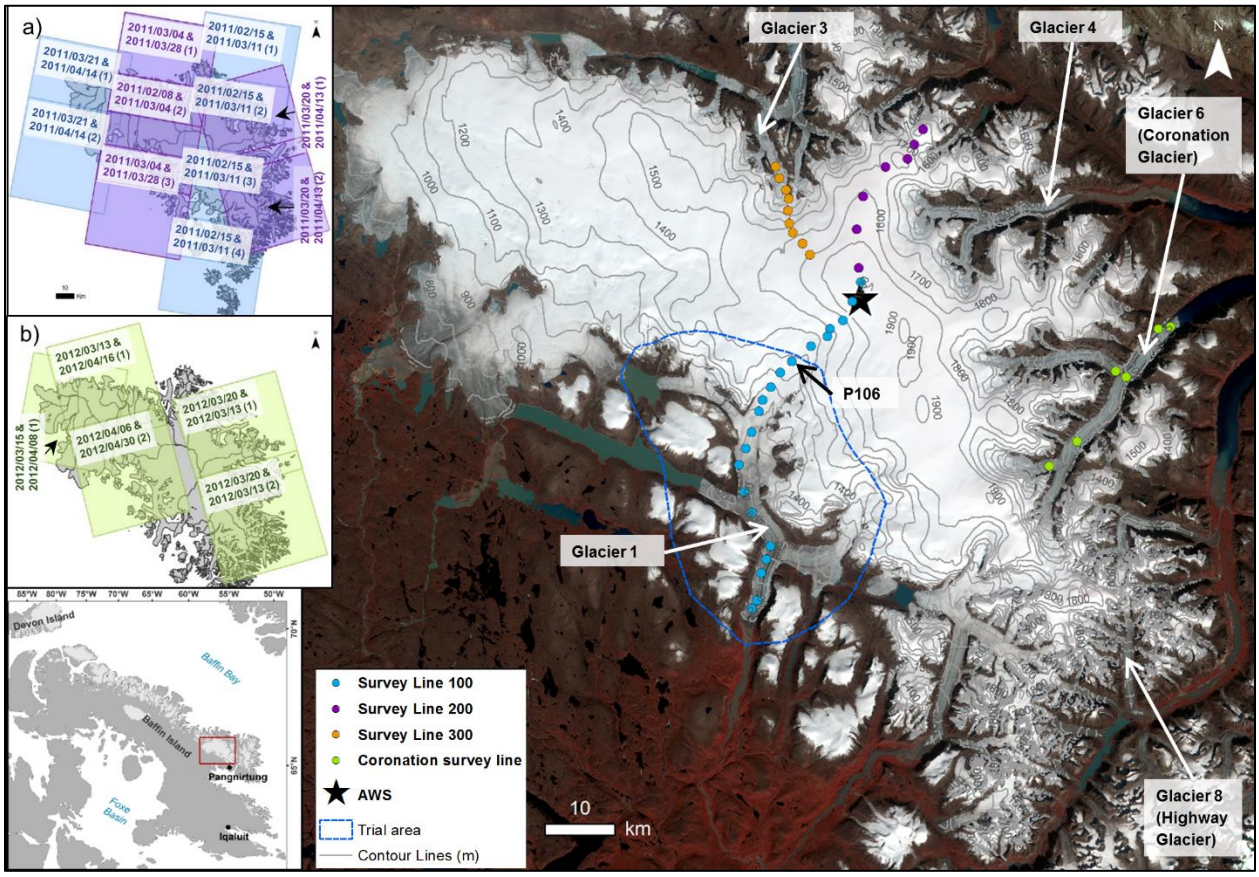

Figure 3.1: Map of Penny Ice Cap (67°N, 66°W) with mass balance survey lines and automatic weather station (AWS). RADARSAT-2 image pair footprints used to produce the velocity map shown in Fig. 3.3 are included as insets for the: a) 2011 fine beam, and b) 2012 ultrafine beam images. Whenever possible, the higher resolution 2012 images were prioritized for fast flowing areas. Background image: Landsat 5, August 19, 1985.

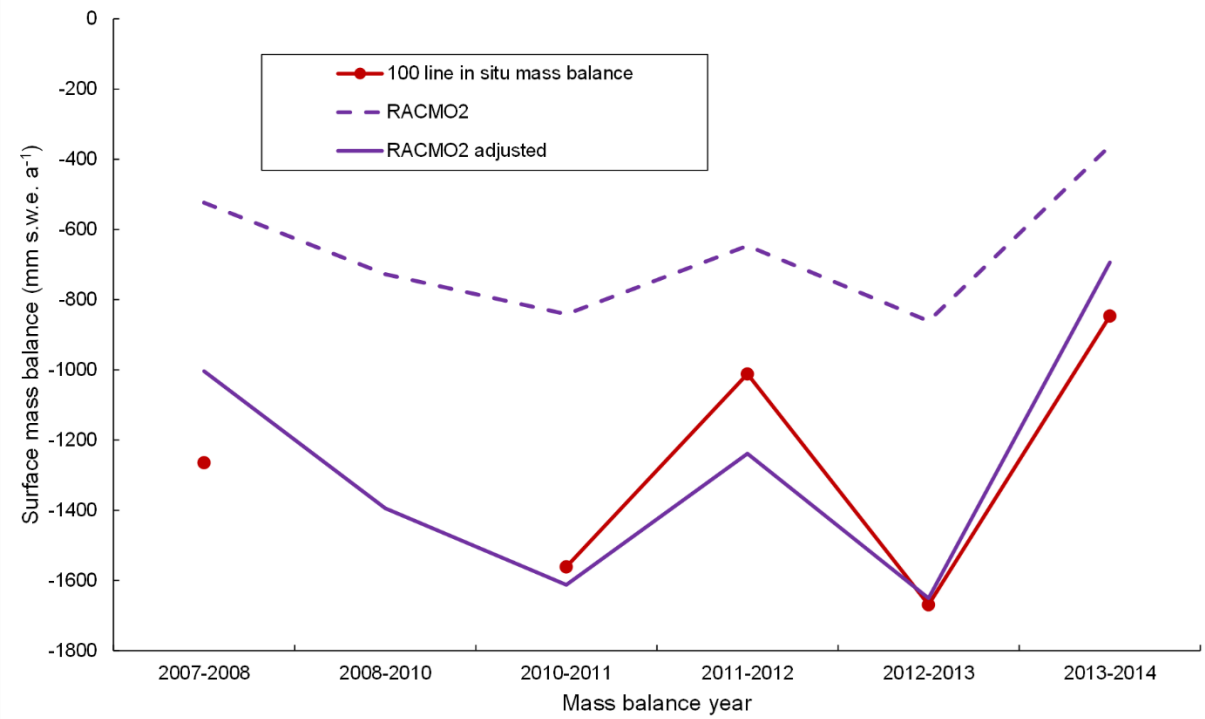

Figure 3.2: Comparison of annual mean in situ mass balance measurements along the 100 survey line on PIC, RACMO2.3 mass balance outputs for grid cells overlapping each stake on this survey line, and the same data multiplied by a correction factor of 1.92 (= average in situ SMB / average RACMO2 SMB).

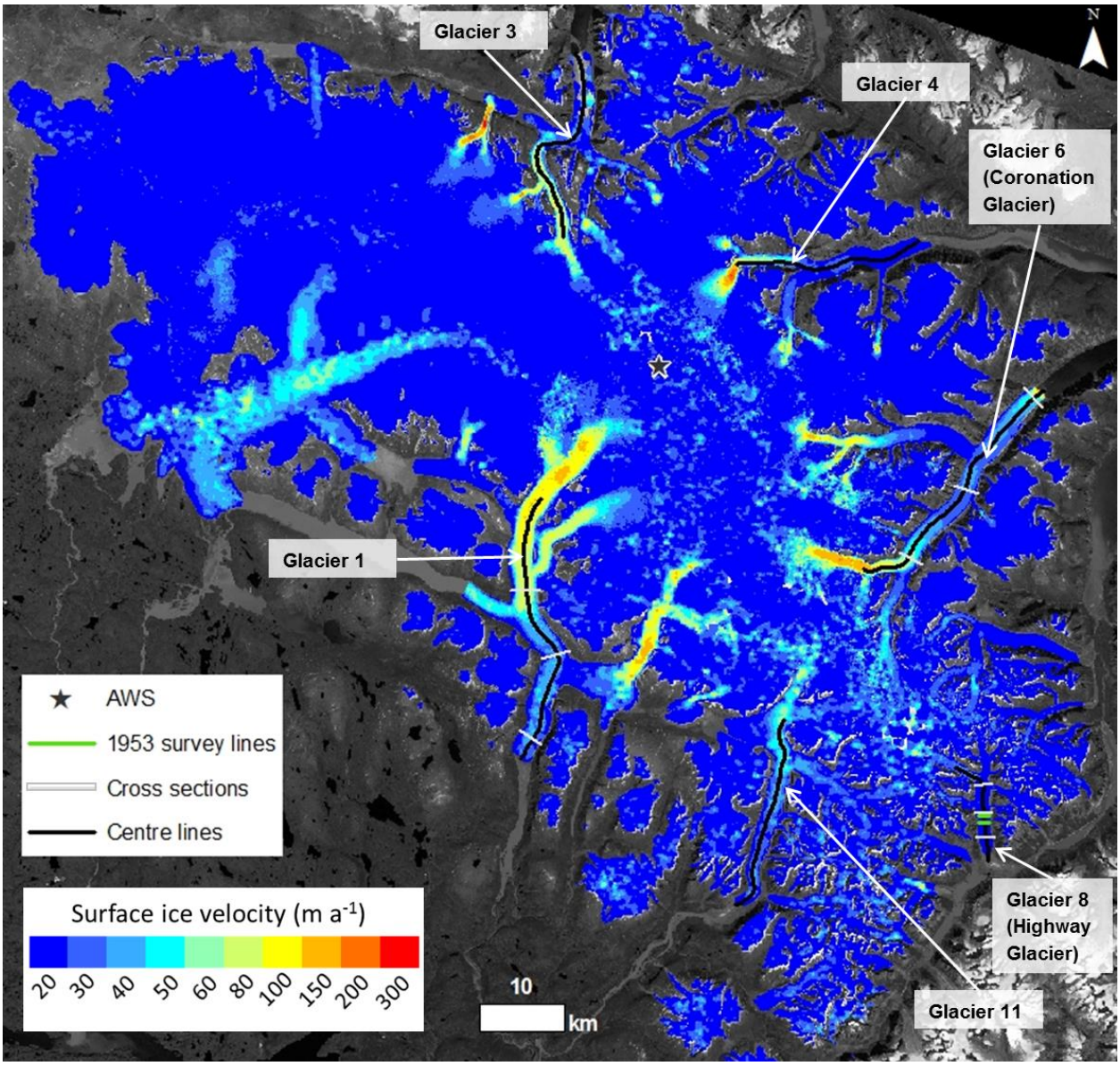

Figure 3.3: RADARSAT-2 derived surface velocity map of PIC from images acquired in winter 2011 and 2012 (see Fig. 3.1). The location of the automatic weather station (AWS), glacier cross sections, centre flow lines, and sites of velocity measurement from 1953 on Highway Glacier [*Ward*, 1955] are indicated. Background image: Landsat 5, July 22, 1998.

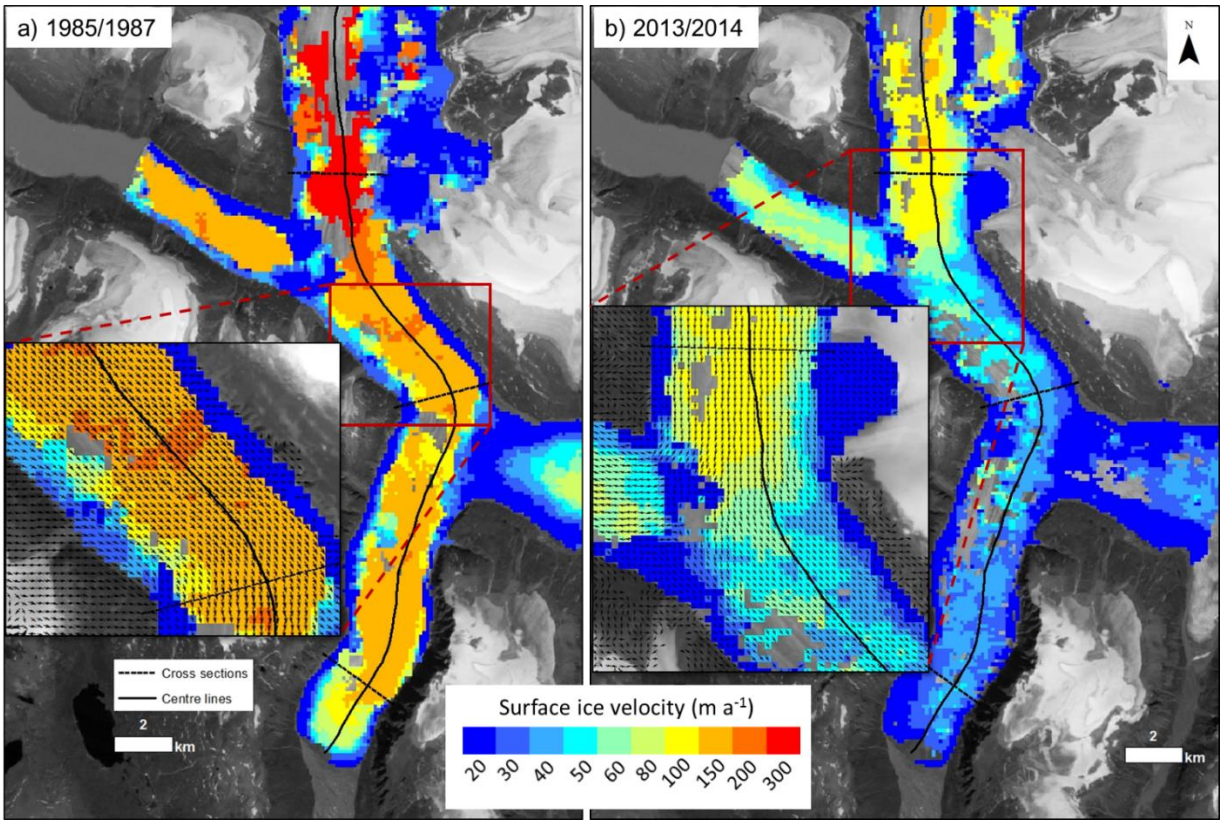

Figure 3.4: Spatial distribution of surface velocities on Glacier 1 between a) 1985-1987 and b) 2013-2014 from feature tracking of optical image pairs. Insets show individual velocity vectors.

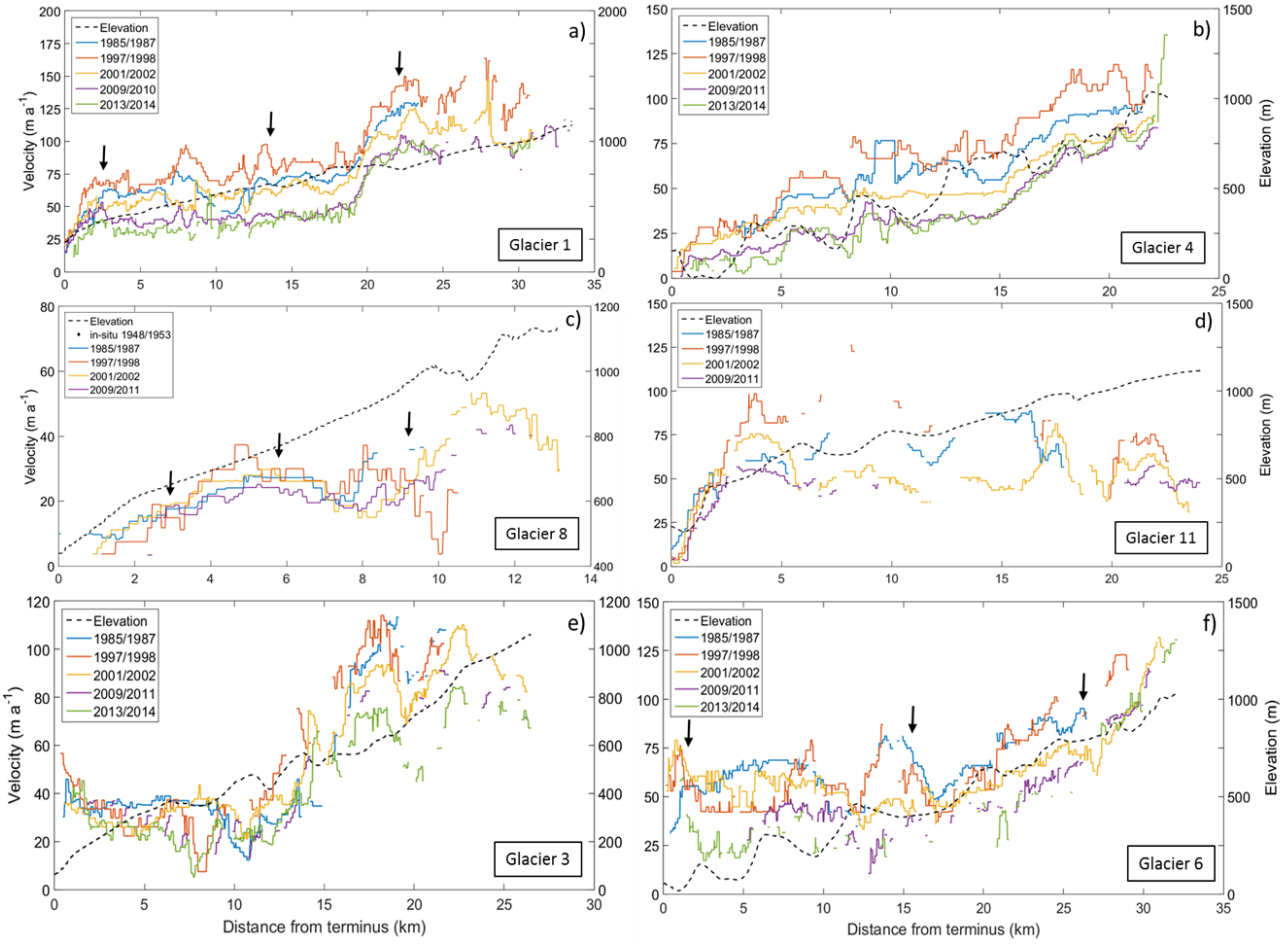

Figure 3.5: Surface velocity changes from 1985-2014 for land-terminating (Glaciers 1, 4, 8, 11) and tidewater-terminating (Glaciers 3, 6) centre flow lines on PIC derived from feature tracking of optical image pairs. The location of transverse profiles shown in Fig. 3.7 are indicated with black arrows.

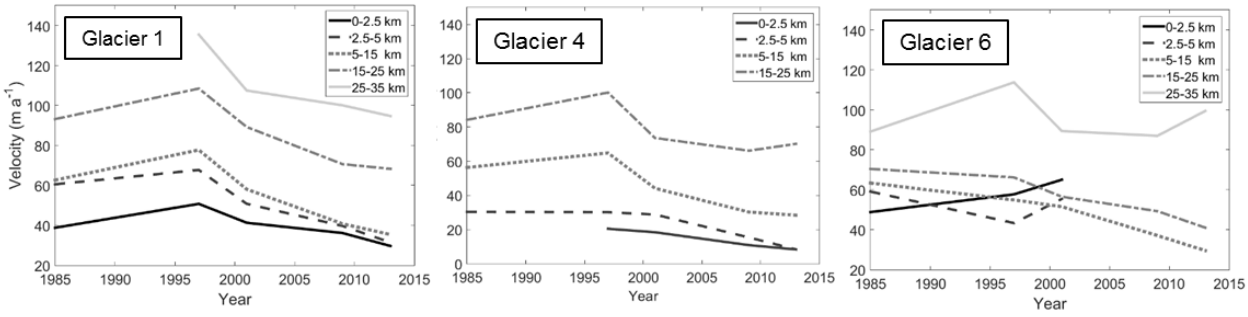

Figure 3.6: Surface velocity changes from 1985-2014 on PIC for the three outlet glaciers with the most continuous data coverage. Each series represents the averaged velocity over a section of the centre flow line profile identified by its distance from the terminus.

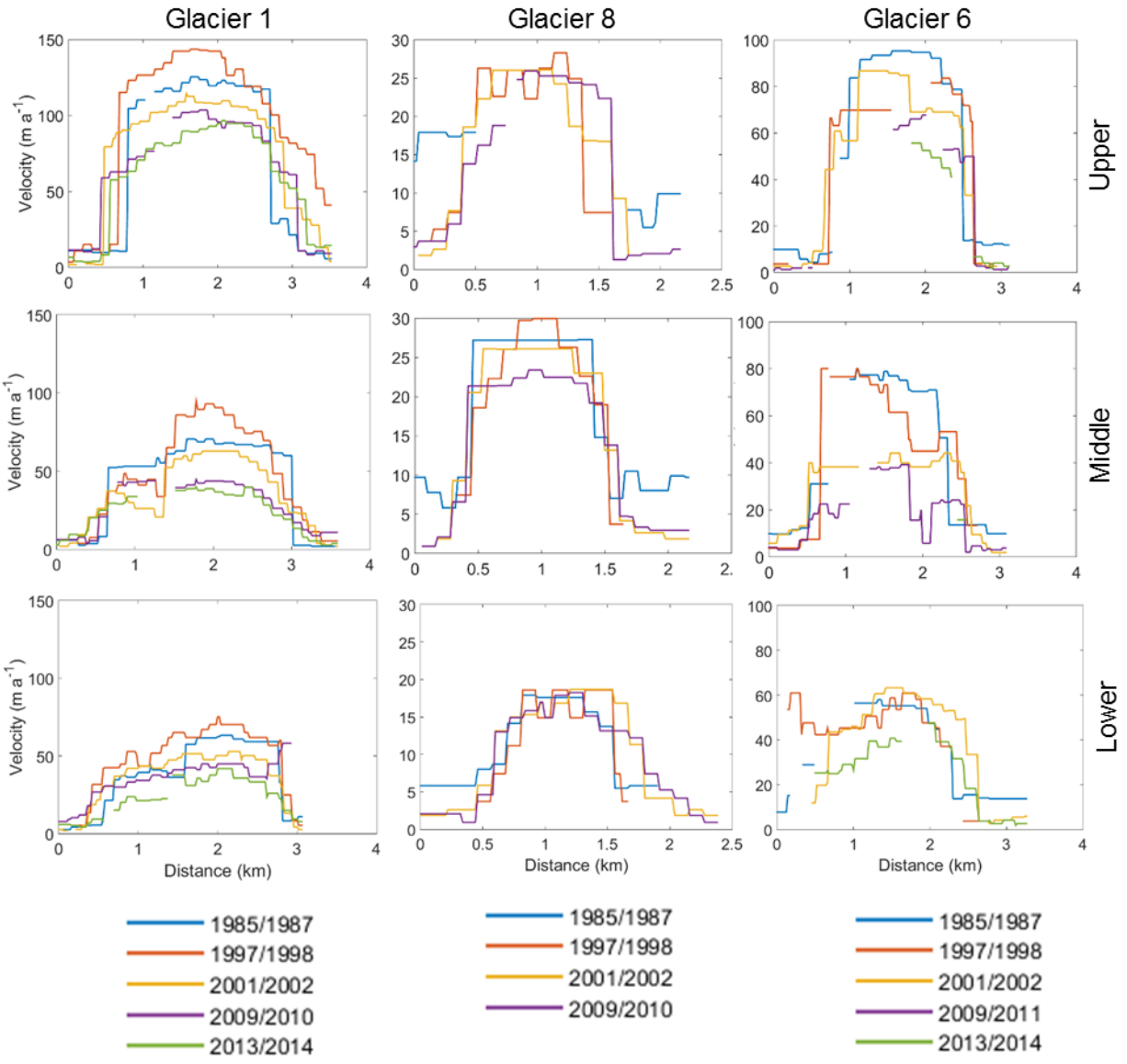

Figure 3.7: Cross-sectional surface ice velocities from feature tracking of optical image pairs for the upper, middle and lower ablation areas of Glaciers 1, 8 and 6 on PIC (1985-2014). Distance was measured looking in an upglacier direction, from left to right across each glacier.

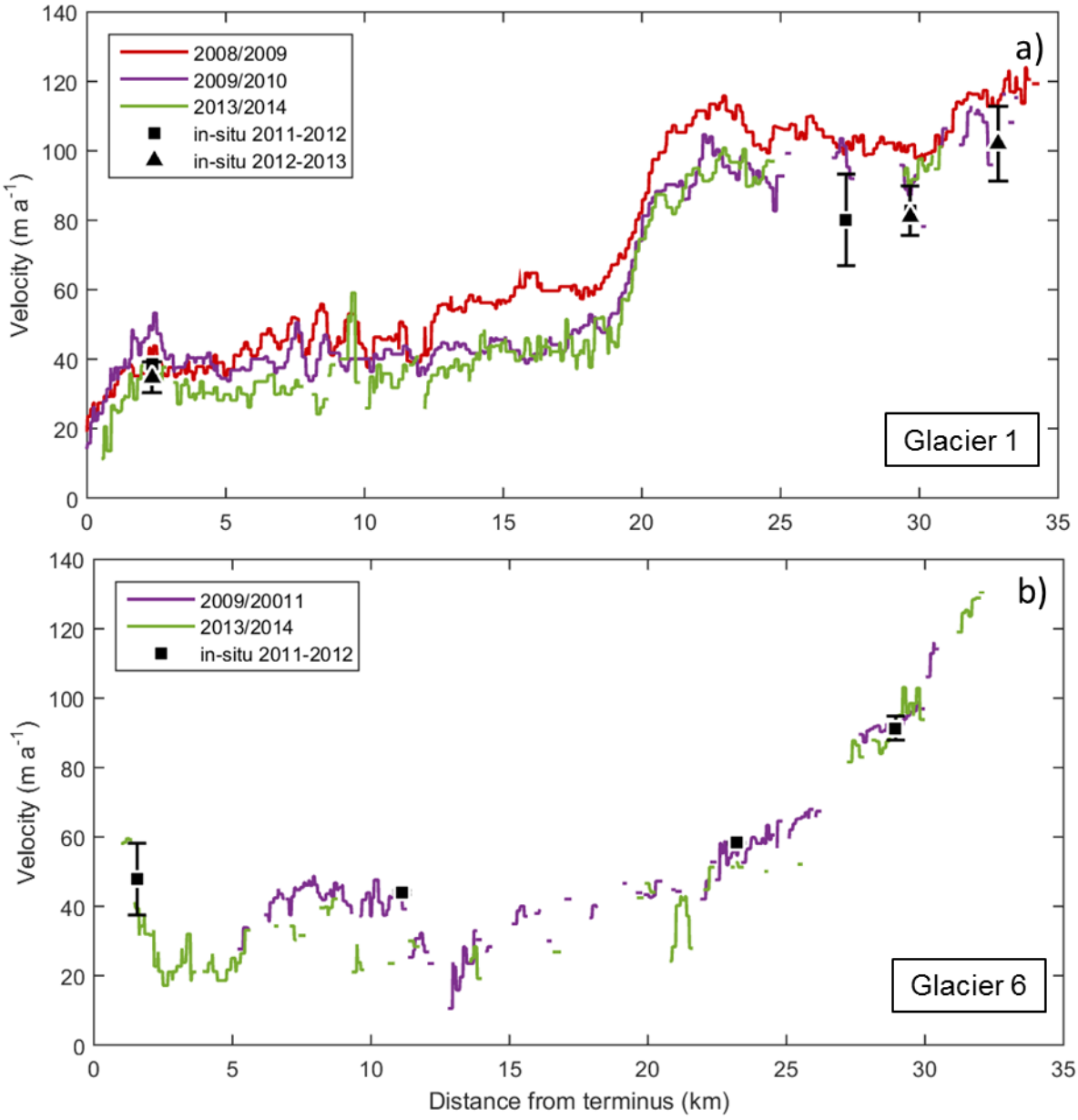

Figure 3.8: Annual variability in surface ice velocities on PIC along glacier centre lines captured with optical imagery (coloured lines) and in situ dGPS measurements (black triangles or squares) from 2008-2014, including 95% confidence interval error bars for: a) Glacier 1 (land-terminating); b) Glacier 6 (tidewater-terminating). The 95% confidence interval for dGPS points at ~11 km and ~23 km for Glacier 6 are < ±0.6 m a^{-1} and are therefore not visible on this graph.

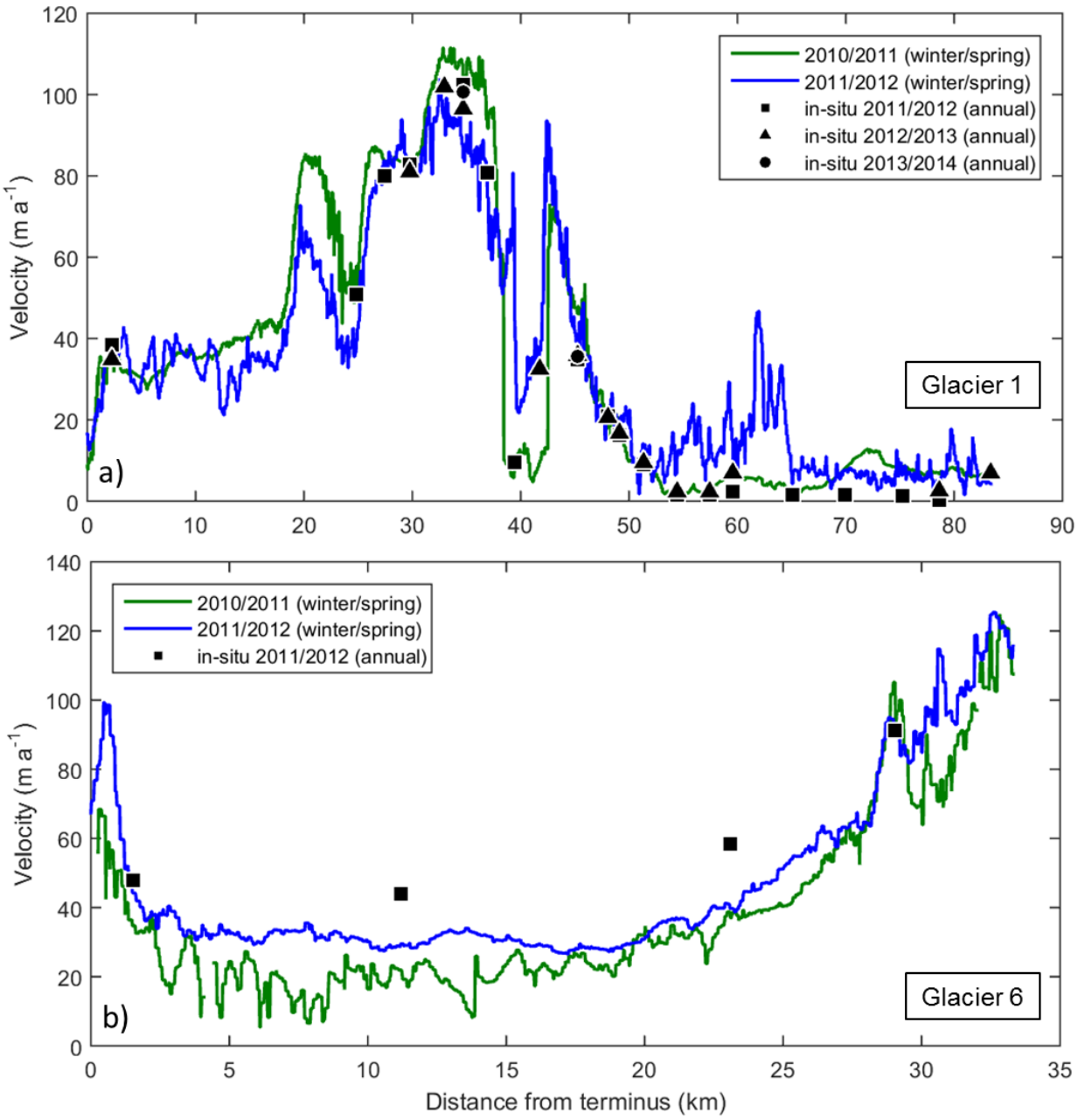

Figure 3.9: Winter SAR-derived surface ice velocities (coloured lines) and annual in situ dGPS velocity measurements along the central flow line of PIC outlet glaciers (Fig. 3.3) connecting the dGPS point locations on: (a) Glacier 1 (land-terminating); (b) Glacier 6 (tidewater-terminating). 2010/2011 and 2011/2012 SAR velocities were derived from ALOS PALSAR and RADARSAT-2 data, respectively.

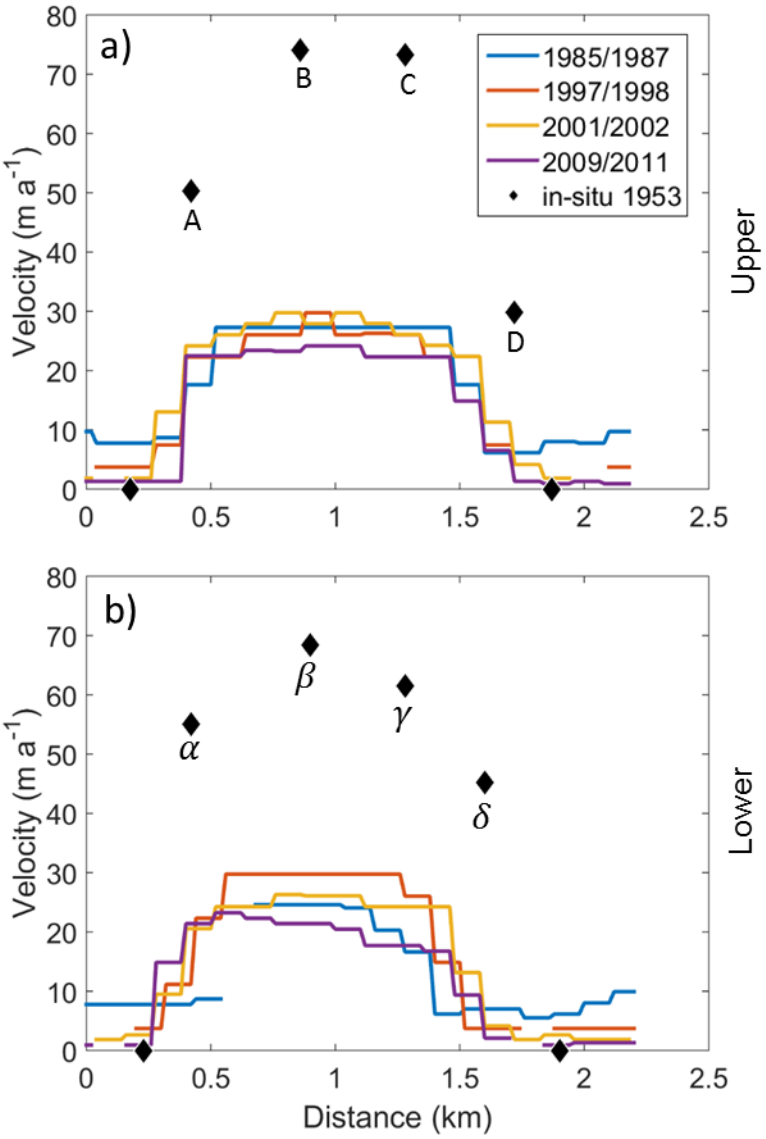

Figure 3.10: Velocity stake measurements from 1953 on two Highway Glacier transverse transects (Fig. 3.3) with annual optical imagery results extracted along the same transect. Zero motion in 1953 was assumed to occur at the glacier edge defined using the oldest Landsat image available (August 16th, 1975).

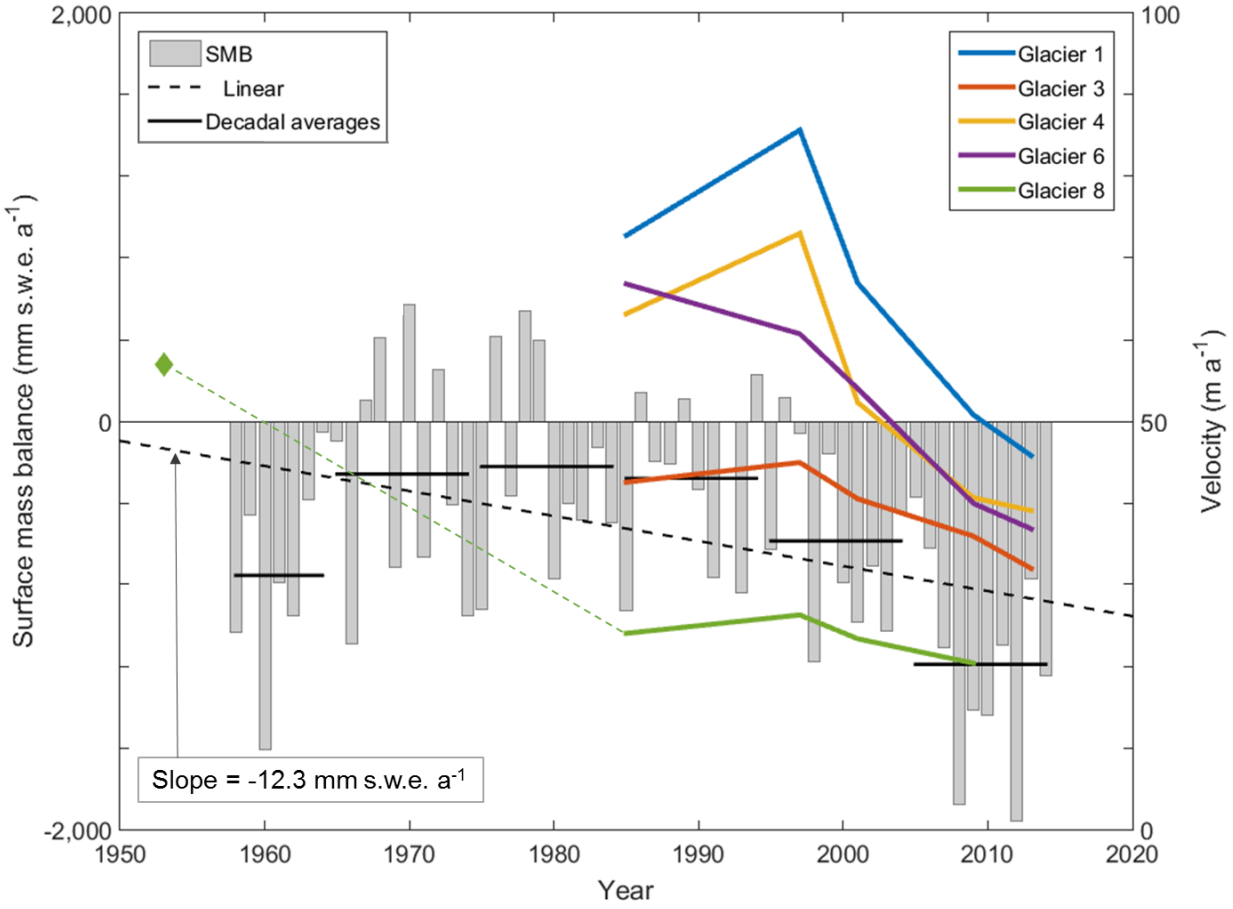

Figure 3.11: Comparison of measured velocity and modeled mass balance changes observed on PIC since the early 1950s: Average glacier annual velocities derived from optical imagery (1985-2014), the ice-cap-wide average annual and decadal mean surface mass balance (SMB) simulated by RACMO2 (1958-2014), linear SMB trends over the same period, and the average 1953 velocity on Highway Glacier (Glacier 8) calculated from eight stake measurements (green diamond; Ward, 1955).

CHAPTER 4: MODELING THE SURFACE MASS BALANCE OF PENNY ICE CAP, BAFFIN ISLAND, 1958-2099

ABSTRACT

Projections of mass change over the next century for glaciers in the southern Canadian Arctic are limited as there are no studies to date that have used spatially distributed data to calibrate or validate mass balance models there, despite rapid mass loss observed over the past few decades. In this study we model the surface mass balance of the largest ice cap in the southern Canadian Arctic from 1958 to 2099 with an enhanced temperature index model calibrated with in situ data from 2006-2014. Since the mid-1990s mass balance rates over Penny Ice Cap (PIC) have become increasingly negative, with a pronounced increase in the mass loss rate since 2005. Peak mass loss is projected to occur in the late 2070s and PIC is expected to lose 16-20% of its initial 2014 ice volume by 2099 assuming a moderate climate warming scenario (RCP4.5). If a +2°C offset is applied to this scenario, the ice cap is expected to lose 30-40% of its initial ice volume by 2099. Assuming the average mass loss rate between 2015-2099 continues into the future, PIC will disappear in ~530 years for the RCP4.5 scenario and in ~290 years for a +2°C increase above this.

4.1 INTRODUCTION

Glaciers in the southern Canadian Arctic Archipelago (CAA; Baffin and Bylot islands) have experienced increasing mass loss rates in recent decades, particularly since 2005 [*Gardner et al.*, 2011; *Harig and Simons*, 2016]. The area-averaged mass loss there was 1.6 times greater than in the northern part of the CAA (Queen Elizabeth Islands) over the period 2003-2009 [*Gardner et al.*, 2012]. There is no evidence of significant decrease in precipitation in the southern Canadian Arctic since the 1950s, while temperatures have increased [*Gardner et al.*, 2012; *Vincent et al.*, 2015], so the main driver of mass loss is most likely greater summer melt. How this rapid warming will affect the future surface mass balance (SMB) of ice caps across this region is an important question. The largest ice cap in the southern CAA is Penny Ice Cap (hereafter: PIC; Fig 4.1). *Lenaerts et al.* [2013] used a coupled atmosphere/snow model forced with the IPCC's moderate RCP4.5 greenhouse gas emission scenario to model the future response of ice caps in

the CAA. Their model forecasts sustained and irreversible glacier mass losses in the southern CAA, increasing from -29 ± 6 Gt a^{-1} over 2000-2011 to -62 ± 10 Gt a^{-1} by the end of the 21st century. Prior to the *Lenaerts et al.* [2013] study, PIC was only modeled as part of global-scale assessments of glacier losses, which can have major uncertainties due to the lack of local model calibration or validation (e.g. *Radic and Hock*, 2011; *Marzeion et al.*, 2012; *Slangen et al.*, 2012; *Huss and Hock*, 2015). None of these studies were supported by spatially-distributed data from PIC itself, and their projections for the future of this ice cap therefore remain approximate.

In this study we modeled the daily SMB of PIC from 1958 to 2099 using an enhanced temperature-index model calibrated with in situ data collected from the ice cap between 2006 and 2014. Model outputs were compared to historical data, were used to quantify contributions to sea level rise, and to determine when PIC will reach its peak melt output. The latter results are locally relevant since one of the most important hydrological outlets of PIC is in a valley (Akshayuk Pass; Fig. 4.1) which is a popular hiking route in Auyuittuq National Park. This valley has experienced sudden and dramatic increases in streamflow over the past decade due to increased glacier melt and rainfall, resulting in the evacuation of hikers [*Anon*, 2008]. Planning for safe passage in the valley therefore requires projections of glacier meltwater contributions to streamflow.

An enhanced temperature index model was chosen since there is insufficient data to calibrate a full energy balance model. Temperature index models have been shown to produce realistic simulations of glacier SMB and meltwater output, especially at the catchment scale and on seasonal to interannual time scales [*Hock*, 2003]. For example, *Hock* [1999] modeled hourly melt and discharge at Storglaciären, a small glacier in Sweden, using a traditional and a modified temperature index model. Including potential radiation in the temperature index model greatly improved simulations of diurnal discharge fluctuations, but applying a physically based energy balance model showed only minimal improvement [*Hock*, 1999]. Likewise, *Huss and Hock* [2015] found that to produce global estimates of glacier mass loss, a classical degree-day model performed better than a simplified energy balance model. Furthermore, glacier SMB in the CAA is highly correlated to summer temperatures [*Gardner et al.*, 2011; *Sharp et al.*, 2011]. A temperature-index model is therefore expected to provide a good estimate of glacier mass loss in this region.

4.2 STUDY SITE

Located on Cumberland Peninsula, PIC (67°N, 66°W) covers an area of ~6300 km^2 (Fig. 4.1). The eastern side of the ice cap has the greatest relief and highest topography with a summit elevation of ~1930 m a.s.l. Elevations gradually decrease toward the west where the ice cap terminates in a broad, gently sloping lobe-like region. Major outlet glaciers flow from the ice cap interior down deeply-incised valleys toward the north, east and south. Two of these are tidewater terminating: Coronation Glacier in the south-east sector, and an unnamed glacier in the north-central sector (Fig 4.1). The ice cap has a maximum ice thickness of ~880 m, measured with a NASA airborne radar near its summit [*Shi et al.*, 2010]. The majority of the ice cap moves slowly (<20 m a^{-1}), particularly in the interior, with faster motion limited to the upper reaches of outlet glaciers, where velocities may range from ~100-250 m a^{-1} [*Schaffer et al.*, in review-a.; *Van Wychen et al.*, 2015]. Since 1985 all of the major outlet glaciers have decelerated by an average rate of 12% $decade^{-1}$ [*Schaffer et al.*, in review-a]. In contrast to Barnes Ice Cap (central Baffin Island) and Bylot Island Ice Cap, there is no evidence of surging [*Van Wychen et al.*, 2015].

Annual SMB measurements have been conducted on PIC since 2006 along four survey lines (designated 100, 200, 300 and Coronation; Fig. 4.1). These measurements were used to calculate a mean equilibrium line altitude (ELA) of ~1646 m between 2006-2014, with a variation between ~1320 m in low mass loss years to 1820 m during high mass loss years. Line 100 on Glacier 1 covers the largest range of elevations (329 m to 1817 m). The average SMB along this line was -1.3 m w.e. a^{-1} between 2007-2014, but varied from -0.8 to -1.7 m w.e. a^{-1} between low and high mass loss years, respectively. Thinning rates are 3-4 m a^{-1} at the ice cap margin, amongst the highest rates in the Canadian Arctic [*Zdanowicz et al.*, 2012]. On average, the summer melt period begins ~May 23rd and ends ~September 3rd according to spaceborne passive microwave measurements from 2007-2010 (F. Dupont, personal communication, 2015). Air temperature measurements at an automatic weather station (AWS) at the ice cap summit (see Fig. 4.1) between August 1, 2007 and July 31, 2008 recorded mean, maximum and minimum annual air temperatures of -15.4°C, 2.9°C and -42.9°C, respectively, based on hourly means [*Zdanowicz et al.*, 2012].

There has been a four-fold increase in mass loss on PIC between 2005-2013 compared to the mid-1990s [*Schaffer et al.*, in review-b]. The passive microwave data reveal that the average melt season length on the ice cap nearly doubled between 1979 and 2010 [*Zdanowicz et al.*, 2012]. Infiltration of surface meltwater has resulted in increased firn density since the mid-1990s and caused the 10 m firn temperatures to rise ~10°C between the mid-1990s and 2011 [*Zdanowicz et al.*, 2012]. There has been a relatively rapid upglacier migration of the ELA, resulting in large areas of firn at depth below the current ELA which has far outpaced the dynamic response of the ice cap [*Schaffer et al.*, in review-b]. Recent surface melt rates are comparable to those last experienced over 3000 years ago [*Zdanowicz et al.*, 2012].

4.3 METHODS

The mass balance (b) over PIC was calculated from the sum of ablation (a), accumulation (c), and iceberg calving(d):

$$b = a + c + d \quad (1)$$

The two SMB terms *a* and *c* were calculated with the Distributed Enhanced Temperature Index Model (DETIM; *Hock*, 1999) (section 4.3.1) calibrated using in situ SMB data from PIC collected between 2006-2014, and NASA Airborne Topographic Mapper (ATM) altimetry elevation (hereafter: ATM altimetry) changes from 2005-2013 (section 4.5). DETIM is fully distributed, meaning that the SMB is calculated for each grid cell in the digital elevation model (DEM) over PIC, and it also incorporates volume-area scaling (section 4.3.2). The d term only accounts for calving and neglects mass loss due to submarine melting. A constant value of d of 0.02 Gt a^{-1} [*Van Wychen et al.*, 2015] was used rather than incorporating a separate calving model [e.g. *Trussel et al.* 2015], since calving is a minor component of the mass budget of PIC, accounting for only ~0.2% of its total mass loss in 2011, and it is not known how this may have varied over time.

DETIM was used to calculate SMB from 1958 to 2014 with climate forcing provided by daily simulations of temperature and precipitation generated by the RACMO2.3 climate model [*Lenaerts et al.*, 2012; *Noël et al.*, 2015]. Changes in glacier area over time were accounted for

by providing DETIM with updated glacier outlines for 1975, 2001 and 2014. Likewise, changes in firn cover were updated with end of summer surface cover grids (snow, ice or firn) for 1975, 2001 and 2014. To project future mass loss of PIC to the year 2099, DETIM was forced with RACMO2.1 output [*Noël et al.*, 2015] under a mid-range climate warming scenario (RCP4.5). The model was first run with a constant glacier area, and again with an evolving glacier area over time (section 4.3.2). The 2014 firn cover was applied until the surface was projected to become free of firn (section 4.3.3). Projections were made for the best measured and most representative outlet glacier, Glacier 1 (Fig. 4.1), and upscaled to the entire ice cap. Glacier mass loss was converted to sea level rise equivalent by assuming an ice density of 900 kg m^{-3} and a global Ocean area of 3.625×10^8 km^2 [*Cogley et al.*, 2011].

4.3.1 *Surface mass balance*

The two main components of the SMB $(a + c)$ are parameterized in DETIM as follows (*Hock*, 1999; http://regine.github.io/meltmodel/):

$$a = \begin{cases} (M_f + R_{f\ snow/ice} I)T, & T > 0 \\ 0, & T \leq 0 \end{cases} \quad (2)$$

where M_f is a melt factor (mm d^{-1} °C^{-1}), $R_{f\ snow/ice}$ is a radiation factor for snow or ice (mm m^2 W^{-1} °C^{-1} d^{-1}), I is the potential clear-sky direct solar radiation (W m^{-2}) and T is the daily mean air temperature (°C). Specific values of M_f and R_f were derived for PIC (section 4.5). For each day of the year, I was calculated from solar geometry and topographic shading [*Hock*, 1999] determined from the Canadian Digital Elevation Data (CDED) DEM (section 4.4.1). Calculating the solar radiation is computationally intensive, so we used the same daily values for each year of the model run. Temperature input data (T) were supplied by the daily RACMO2 output at the location of the summit AWS, and were extrapolated to each grid cell over the ice cap using a monthly lapse rate (section 4.4.4). Likewise, daily total precipitation data (P) were supplied by RACMO2 for the ice cap summit and extrapolated using a precipitation gradient (section 4.4.4). A threshold temperature (T_{snow}) distinguishes between solid precipitation (snow accumulation) and rainfall (when $T \geq T_{snow}$):

$$c = \delta P \begin{cases} \delta = 1, & T < T_{snow} \\ \delta = 0, & T \geq T_{snow} \end{cases} \quad (3)$$

4.3.2 *Volume-area scaling*

Glacier mass loss is often accompanied by a reduction in glacier extent, resulting in a negative feedback. Ice is typically lost at the lowest elevations first, so the remaining glacier mass has a higher mean elevation and smaller area, which then reduces the overall mass loss rate. We accounted for changes in glacier extent by using a classical volume-area scaling approach (equation 4) included in DETIM.

$$\Delta V = C(\Delta A)^{\gamma} \quad (4)$$

For each daily time step, the change in glacier volume (ΔV), known from the modeled SMB, was used to calculate the change in glacier area (ΔA). For the scaling parameter γ we used a value of 1.25, as suggested for ice caps [*Bahr et al.*, 2015]. Parameter C was derived by solving eq. (4) for Glacier 1, using the total volume obtained from ice thicknesses provided by *Huss and Farinotti* [2012], and the associated glacier area, to yield a value of 2.37. The glacier area was adjusted in DETIM by calculating the number of grid cells represented by ΔA, then removing grid cells sequentially starting with those at the lowest elevation. Currently, the model does not account for glacier advance; if the mass balance is positive, the area is kept constant. This method of calculating C assumes that all the volume loss is compensated for by retreat (rather than elevation change) and provides a theoretical upper limit for retreat.

4.3.3 *Refreezing*

With increasing temperatures, the refreezing of meltwater has become an increasingly important mass accumulation process on PIC [*Zdanowicz et al.*, 2012; *Schaffer et al.*, in review-b]. Borehole and shallow core measurements from the ice cap's summit show that the firn density has been increasing since the mid-1990s due to the formation of thick infiltration ice layers in the firn [*Zdanowicz et al.*, 2012]. In the future it is expected that the firn zone will be replaced completely with superimposed ice. To determine when this will occur, we modeled the refreezing process separately, since DETIM does not currently include a refreezing routine. Four different refreezing parameterizations and variations outlined in *Reijmer et al.* [2012] (equations 5, 6 and 7) and *Janssens and Huybrechts* [2000] (equation 7) were tested using a proxy record of annual surface melt on PIC [melt feature %; *Zdanowicz et al.*, 2012] over the period 1963-2010, developed from firn cores collected near the ice cap summit. The parameterizations that were

tested varied in complexity, with the most complex ones accounting for refreezing either based on the firn cold content or by the filling of pore spaces within the firn. All trials were started in 1963 as this year is identifiable by a radioactive layer in the firn on PIC [*Zdanowicz et al.*, 2012]. The best fit to the firn core proxy melt record was obtained using a simple parameterization that only accounts for the cold content:

$$R = min[P_r, W_r] \quad (5)$$

where the refrozen mass (R) is equal to the minimum of either the available water mass (W_r) or the maximum potential refrozen mass (P_r). The latter is given by:

$$P_r = \frac{C_i}{L_f} h_a |T_s| \quad (6)$$

where C_i is the heat capacity of ice (2050 J kg^{-1} K^{-1}), L_f is the latent heat of fusion (0.334 x 10^6 J kg^{-1}), h_a is the thickness of the thermally active layer and T_s is the annual mean glacier surface temperature which was obtained from RACMO2. The thickness of the thermally active layer is the maximum depth of the 0˚C isotherm layer in summer. The value of W_r was assumed to equal the mean annual snowfall, also obtained from RACMO2.3 near the ice cap summit. Values of h_a were calculated from thermistor string measurements made in boreholes near the PIC summit in 1953 and 2011 [*Zdanowicz et al.*, 2012]. In 1953, h_a was ~1.4 m and the firn temperature at ~10 m depth was ~ -13˚C. For 2011, it was ~3.1 m, and the 10-m temperature was -3 ˚C.

Equation 5 was calibrated to estimate values of the summer melt percentage from firn cores by varying h_a through time within a realistic range of values informed by the thermistor string measurements. The best fit was obtained for values which varied linearly between 1.3 m in 1963 and 3.1 m in 2014. A simulation of refreezing at the summit of PIC for 1963-2014 using the optimal parametrization (Fig. 4.2a) reproduces the observed long term trend recoded in firn cores (difference < 1%, and within the 95 % confidence limits). While the model does not accurately capture the interannual variations, this is less important for long-term projections.

4.4 SUPPORTING DATA

4.4.1 *Digital elevation model*

We used the 1:250 000 Canadian Digital Elevation Data (CDED) DEM, created from 1956 to 1982 air photos, which has a resolution of 3-12 arc seconds (http://geogratis.gc.ca). Over PIC, the average grid cell size is ~93 x ~37 m. The CDED was used to calculate the potential direct solar radiation for each day of the year [*Hock*, 1999] and the SMB. Other DEMs such as the ASTER Global DEM (GDEM V2) and Canadian DEM (CDEM) showed unrealistic artifacts, so these were not used.

4.4.2 *In situ data*

The SMB measurements used to calibrate the model were made annually on a fixed-date system [*Cogley et al.*, 2011] at stakes along three survey lines in spring (100, 200, 300 lines), and on Coronation Glacier during the summer, between 2006-2014. In total, 140 measurements were taken at elevations ranging from 71-1822 m a.s.l. (Fig. 4.1). Measurements of winter accumulation were used as a proxy for winter mass balance (section 4.4.4). Annual and winter mass balance measurements are shown in Figure 4.3.

The DETIM model run from 1958 to 2014 was compared to historical geodetic and SMB data. The Arctic Institute of North America (AINA) carried out the first expedition to PIC in 1953, and collected SMB measurements on Highway Glacier at 11 locations ranging in elevation from 440 to 2050 m a.s.l. (*Ward and Baird*, 1954; Fig. 4.1, 4.3). Geodetic measurements were taken from 1962 to 1965, which revealed a surface elevation increase of ~0.7 m over that time period at ~1800 m a.s.l. [*Weber and Andrieux*, 1970; *Weber and Cooper*, 1993].

4.4.3 *Elevation change*

In spring 1995, 2000, 2005, 2013 and 2014, repeat ATM altimetry measurements were performed over PIC by NASA prior to the start of the ablation season [*Schaffer et al.*, in review-b; Fig. 4.1]. We used the change in surface elevation ($\dot{h}$) between flights for 2005-2013 to calibrate the model, and those from 1995-2000 and 2000-2005 to independently evaluate the DETIM model outputs. Values of $\dot{h}$ for 1995-2000, 2000-2005, 2005-2013 were computed by *Abdalati et al.* [2004], *Gardner et al.* [2012] and *Schaffer et al.* [in review-b], respectively.

4.4.4 *Climate data*

Air temperatures have been recorded intermittently at the PIC summit AWS since 2007 (Fig. 4.1 and 4a). The AWS has a Campbell Scientific 107F model thermistor positioned approximately 2.5 m above the snow surface with an accuracy of $\pm 0.4^0$C. Temperatures were recorded every 5 minutes and averaged daily. In April 2012, a second AWS was installed on Glacier 1 at ~490 m a.s.l. (AWS2; Fig. 4.1). It recorded temperature and snow height twice daily, with the same specifications as the summit AWS, from April 2012 to February 2013. Measurements of the winter snowpack at each stake along three survey lines (Fig. 4.1 and 4.3b) have also been collected in early spring since 2006, and were used as a proxy for the annual precipitation and winter mass balance. Snow pits were dug at most SMB stake locations, and a known volume of snow or firn from each stratigraphic layer was weighted to determine the density. Infiltration ice lenses and layers were assumed to have a density of 900 kg m^{-3}.

To obtain a continuous record of site-specific temperature and precipitation from 1958 to 2099 we used the RACMO climate outputs for the grid cell closest to the AWS at the summit of PIC. For the period 1958-2014, we used the output from RACMO2.3 forced by the most recent reanalysis data from the European Centre for Medium-Range Weather Forecasts (ECMWF), called ERA-interim, with a grid resolution of 11 km [*Lenaerts et al.*, 2012; *Noël et al.*, 2015]. For the period 2015-2099, we used climate outputs from an earlier version of the model, RACMO2.1 [*Lenaerts et al.*, 2013; *Van Angelen et al.*, 2013], because RACMO2.3-generated climate fields presently do not extend beyond 2015. The main difference between RACMO2.3 and RACMO2.1 is that RACMO2.3 has been improved with major changes in the description of cloud microphysics, surface and boundary layer turbulence and radiation transport [*Noël et al.*, 2015]. Precipitation outputs have also been modified to be exclusively snowfall under freezing conditions, but this update does not impact our results since we provided DETIM with the total precipitation and with a calibrated, PIC-specific snow/rain threshold temperature. RACMO2.1 was forced with output from a Coupled Model Intercomparison Project Phase 5 (CMIP5) general circulation model HadGEM2-ES [*Lenaerts et al.*, 2013]. The general circulation model was itself forced using a midrange climate warming scenario (RCP4.5) where the radiative forcing of ~4.5 W m^{-2} stabilizes by 2100. The RCP4.5 scenario leads to a global mean warming of 1.8°C at 2 m, and a 3.6% increase in precipitation over the period 2081-2100, relative to the 1986-2005 average. Under this scenario, temperatures and precipitation in the Baffin Island region, are

expected to increase by ~3°C and ~15%, respectively, by 2100 [*IPCC*, 2013]. Projected temperatures in the Arctic regions are higher than global averages largely due the lowering of surface albedo as sea-ice and snow coverage decreases (e.g. *Serreze et al.*, 2007).

The RACMO2.3 temperature outputs were highly correlated with temperatures recorded at the PIC AWS over the control period 2007-2014 (Pearson's correlation coefficient r = 0.98, p-value < 0.01; Fig. 4.4b). However, the modeled temperatures were slightly cooler than actual temperatures, with an average offset of -0.28^0C. An offset of +0.28°C was therefore added to each RACMO2.3 data point and the resulting mean annual air temperature at the summit of the ice cap over the period 2007-2014 was ~ -15.3°C. This agrees well with the estimated mean temperature based on AWS data of -16 ± 1.5°C between 2007-2011 [*Zdanowicz et al.*, 2012].

The RACMO2.3 precipitation outputs were compared to: a) late winter measurements of snowpack depth on PIC to calculate the difference between modeled and measured values over the period 2007-2014, and b) ice core data to assess the validity of RACMO2.3 precipitation data over longer time periods. Hereafter, "winter" refers to the span of time from the end of the melt season (typically early September, determined from passive microwave data) to the time when the snowpack measurements were taken, usually mid-April. The RACMO2.3 cumulative winter precipitation captured the interannual variability in the winter snowpack depth (r = 0.65, p-value = 0.021; Fig. 4.4c-d), but underestimated winter precipitation by 21% on average. The RACMO2.3 precipitation values were therefore increased by 21% for use in DETIM.

The average RACMO2.3 precipitation between 1963 – 2011 was also compared to the average accumulation recorded in firn cores taken near the PIC summit over the same time period. The firn cores recorded an average accumulation of 0.40 ±0.05 m w.e. a^{-1} [*Zdanowicz et al.*, 2015] which is equal, within error limits, to the unadjusted RACMO2.3 value of 0.45 m a^{-1} w.e., but less than the adjusted precipitation of 0.54 m a^{-1} w.e.

The RACMO2.1 temperature outputs were well correlated with temperatures recorded by the PIC AWS between 2007-2014 (r = 0.79, p-value < 0.01), but less correlated than RACMO2.3 and cooler, with an average offset of -2.05^0C. RACMO2.1 precipitation outputs did not correlate with interannual variations in snowpack depth, and underestimated the winter precipitation by 31% on average over the period 2007-2014. The RACMO2.1 data were therefore adjusted to match in situ data from the PIC by applying the RACMO2.3 offsets (0.28°C and 21% increase in

precipitation) since the modeled SMB over the calibration period using RACMO2.1 and RACMO2.3 data modified with the same offsets were approximately equal (section 4.6).

4.4.5 *Glacier outlines*

The DETIM simulations were initiated in 1958 using a PIC outline from 1959. This outline was created by Evelyn Dowdeswell (University of Bristol) from aerial photographs taken in 1959, with minor modifications including orthorectification, and the addition of ice masses connected to the ice cap completed for this paper. The model was updated through time with outlines from 2001 (29- 1 July) and 2014 (26 July) delineated from Landsat images by Evelyn Dowdeswell and by Frances Delaney (University of Ottawa), respectively. The 2001 outline was automatically generated and modified to correct for errors such as misclassification in areas of low contrast (e.g. in shadow) or to remove artifacts. The 2014 outline was manually generated and the outline was improved in areas of low contrast and redrawn for many areas with complex terrain. The calibration process was completed using the 2014 outline of PIC.

4.4.6 *End of summer snowline*

As part of its simulations, DETIM models the evolution of the snow cover through time. At the end of winter most, if not all, of the ice cap is covered by snow. As the melt season progresses and the snow cover melts away, glacier ice and firn are exposed. Different albedo values are applied to grid cells with snow, firn or ice, so an end of summer surface cover grid must be provided to define whether ice or firn is present below the winter snow cover. We used the end of summer snowline manually delineated using the latest suitable Landsat imagery as a proxy for the firn area. Images from 1975 (16 Aug. and 2 Sept.), 2001 (29-31 July), and 2014 (26 July) were used, corresponding to the model runs with the 1959, 2001 and 2014 ice cap outlines. A Landsat image surface reflectance threshold of 180 (band 4 for 1975; band 8 for 2001 and 2014) was chosen to delineate the snow patches. This threshold excluded some snow patches with a low reflectance which would very likely disappear by the end of the melt season. All snow patches and snow-free areas within snow patches larger than 0.5 km^2 were delineated (Fig. 4.5).

4.4.7 *Ice thickness data*

Ice thicknesses were required to determine the ice volume and solve for parameter C in equation 4. We used modeled ice thicknesses provided by *Huss and Farinotti* [2012] who calculated these by converting estimates of SMB to balance fluxes and then ice thicknesses by applying Glen's

flow law. Modeled ice thicknesses were compared to those measured using the airborne Multichannel Coherent Radar Depth Sounder (MCoRDS L2) by NASA in conjunction with the 2013 ATM data. Modeled thicknesses were extracted at each airborne measurement point (Figure 4.6). The data sets have a similar distribution of ice thickness with elevation (Fig. 4.6b) and, on average, the MCoRDS thicknesses are 5.8 m greater than modeled thicknesses. While individual measurement can differ by nearly 800 m (Fig. 4.6c) we decided to use the modeled data as it is the only available continuous ice thickness grid for PIC. There are obvious discontinuities between the Randolph Glacier Inventory (RGI; *Arendt et al.*, 2012) drainage basins which are unrealistic (Fig. 4.6a), so we restricted use of the modeled data to the largest RGI basin overlapping Glacier 1.

4.5 CALCULATED INPUTS AND MODEL CALIBRATION

DETIM was customized for PIC by using a site-specific lapse rate, initial snow cover grid, precipitation gradient, and by calibrating four parameters. The RACMO2.3 data were used to calculate monthly temperature lapse rates over PIC. The AWS and AWS2 data overlapped during July 2010, and for that month, a mean lapse rate of 4.69°C km^{-1} was calculated. The lapse rate is equal, within error limits ($\pm 0.4^0$C), to the RACMO2.3 lapse rate of 4.66°C km^{-1} obtained from grid cells overlapping AWS and AWS2 over the same time period (Fig. 4.7, Table 4.1). Daily lapse rates were held constant within a particular month.

DETIM requires as an input an estimate of the ice-cap-wide snow cover (extent and thickness) at the start of a simulation. We used the average winter s.w.e. (snow water equivalent) measured at each stake along SMB survey lines on PIC from 2006-2014 to create a linear model of changes in snow cover with respect to elevation (z), after applying a square-root transformation to the snow cover data in order to obtain normally distributed residuals (coefficient of determination R^2 = 0.16, F-test p = <0.001, standard error of coefficient p-value = <0.001; Fig. 4.8). This model was then used to create a snow cover map over the entire ice cap using the CDED DEM, which was in turn used for initializing the calibration process. Subsequently, the snow cover was set to zero automatically by DETIM on the first day of the winter mass balance season each year (JD 247).

The precipitation gradient was calculated from total annual precipitation near the ice cap summit and close to sea level. The total precipitation near the summit of PIC (~1817 m a.s.l.) was obtained from the mean net accumulation recorded in ice cores between 1963-2011 (0.40 m a^{-1} w.e.). At low elevations on the ice cap, late winter snowpack measurements only represent a fraction of the total accumulated precipitation. Using historical weather station data from the nearby town of Pangnirtung (23 m a.s.l.; Fig. 4.1), we determined that 48% of the annual precipitation falls in winter. Accordingly, using the snowpack gradient model we calculated the theoretical snowpack depth at 23 m a.s.l. (~0.12 m w.e.), and added 52% to obtain the total annual precipitation (~0.24 m w.e.). The two endpoints at 23 and 1817 m a.s.l. were then used to calculate a precipitation gradient of +3.8 % per 100 m increase in elevation. Above 1900 m a.s.l., the precipitation was left constant to account for reduced air moisture content and increased wind erosion at higher elevations.

Four parameters in DETIM (M_f, R_{fsnow}, R_{fice} and T_{snow}) were calibrated using in situ SMB and ATM altimetry data from PIC. The calibration was accomplished using a Monte Carlo approach and the optimal values for each parameter were found by systematically varying all parameters over a range of physically plausible values. We required that the cumulative SMB over PIC simulated by DETIM over the period 2005-2013 match the $\dot{h}$ value of -0.72 ± 0.1 m a^{-1} obtained from ice-cap-wide ATM altimetry for that period, after correction for firn densification [*Schaffer et al.*,in review-b]. To ensure a physically realistic model we also required that M_f be > 0 mm d^{-1} $°C^{-1}$, that R_{fice} be 0.2 mm m^2 W^{-1} $°C^{-1}$ d^{-1} greater than R_{fsnow}, and that T_{snow} be ≤ 3°C. The optimization was further constrained by the requirement that the RMSE between the modeled and in situ 2006-2014 SMB data be ≤ equal ± 0.25 m w.e. a^{-1} , which is the estimated in situ SMB measurement error [*Cogley et al.*, 1996]. Daily DETIM SMB outputs were summed over each mass balance year for comparison with annual in situ SMB measurements. This calibration method forces a good fit of the model output to the decadal geodetic balance to ensure that the long-term ice cap response to climate is realistically captured.

With M_f, R_{fsnow}, R_{fice} and T_{snow}, initial increments of 0.5, 0.2, 0.2 and 1, respectively, a total of 13 parameter combinations were identified that met the aforementioned criteria (Fig. 4.9, Table 4.2). Additional model runs were completed to find the single optimal parameter combination with the lowest RMSE. This step used increments of 0.02, 0.02, 0.02 and 0.5 for

$M_f, R_{f\ snow}, R_{fice}$ and T_{snow}, respectively, and iterative convergence was achieved when there was no futher change in RMSE to three decimal places. The optimal parameter combination that was obtained had an RMSE of 0.45 m w.e. and an r^2 of 0.77 (Fig. 4.10; Table 4.2).

4.6 VALIDATION

The output of the DETIM model obtained with the 14 parameter combinations (13 with initial increments and the optimal combination) using the RACMO2.3 data were compared against historical data not used in the calibration process. Figure 4.11 compares the DETIM model SMB output for PIC over the period 1995-2005 to mass changes inferred from ATM altimetry elevation changes ($\dot{h}$) over the same time period. Modeled results closely replicate the ATM-derived mass loss rate between 2000-2005, but overestimate the mass loss rate between 1995-2000. Over the entire 10 year period, the range of model results lie entirely within the error limits of the ATM altimetry data.

Figure 4.12 compares the 1953 SMB measurements on Highway Glacier to the optimal model parameter combination output for SMB at the same locations for 1959. The agreement is excellent with an r^2 of 0.93 and RMSE of 0.21 m w.e.

Modeling forward in time requires the use of RACMO2.1 data. The mean SMB output obtained using these data over the 2005-2013 calibration period is -4.56 Gt a^{-1}, which is nearly identical to that obtained using the RACMO2.3 data (-4.59 Gt a^{-1}). This provides confidence that RACMO2.1 results for 2015-2099 will be similar to those that would have been obtained with RACMO2.3 input data if the latter were available after 2015.

4.7 MODEL RESULTS (1959-2099)

A range of simulations of the SMB of PIC for the period 1959 to 2013 were generated using DETIM (Fig. 4.13a). Overall, the simulations show a relatively stable, albeit negative, SMB until the mid-1990s, followed by an increasingly negative SMB. The spatial pattern of simulated SMB changes over the entire ice cap is shown in Figure 4.14. As can be seen, the western sector and low-lying outlet glaciers show the largest losses, >2.5 m w.e. a^{-1} by 2010-2014.

The refreezing model was applied until 2098 using the RACMO2.1 data (Fig. 4.15). The 5 year running mean (Fig. 4.2b) shows an obvious trend of increasing MF% over time, approaching 95% by 2098, indicating that by that time firn at the surface has nearly disappeared. The MF% does not reach 100% within our modeling period (1958-2099), so we applied the 2014 surface cover grid for all future DETIM runs.

As described above, in view of the computational time requirements, and lack of spatially consistent ice thickness data, we restricted our forward simulations (2014-2099) to Glacier 1. We first ran DETIM to simulate the SMB of Glacier 1 over the period 1958-2014, and compared the results to those obtained for the entire ice cap. The correlation of the modeled SMB mass balance was nearly perfect ($r = 0.9995$), implying that the SMB trends for Glacier 1 can be considered representative of the whole of the PIC. The simulated mass losses for Glacier 1 over the period 1958-2014 represent 10.4% of the ice-cap-wide losses, calculated from the average of daily outputs between 1958-2014. Accordingly, we used this ratio to upscale the simulated future SMB changes for Glacier 1 to the entire ice cap. Figure 4.16 shows the simulated spatial pattern of SMB changes over the Glacier 1 catchment from 2010 to 2099. The greatest surface height change occurs at the glacier terminus, but the greatest total mass losses will occur within elevation bands that cover a large area and have a relatively high surface height change. To determine the variability in total mass loss with altitude (Fig. 4.17b), the SMB (m w.e. a^{-1}) was multiplied by the area (km^2) for each 20 m elevation band (Fig. 4.17a). Results show that largest mass losses are expected to occur between 600-1400 m a.s.l. (Fig. 4.17b).

The projected SMB variations over the period 2014 to 2099, upscaled to the entire ice cap, are shown in Figure 4.13b for simulations with a constant glacier area, and for simulations that include a changing glacier area (by volume-area scaling) over time. The predicted SMB decreases over most of the simulated period, reaching a maximum SMB loss in the late 2070s. The lowest 10-year mean SMB values are -9.42 and -7.16 Gt a^{-1}, for the two simulations, which are 2.1 and 1.6 times lower, respectively, than the average SMB of -4.56 Gt a^{-1} over the calibration period (2005-2014). Both simulations shown in Fig. 4.13 use the same initial SMB for the present day, but the volume-area scaling produces a lesser rate of SMB decrease, which results in important differences in the projected SMB at the end of the simulation period.

By 2099 PIC is predicted to lose between 16 and 20% of its present-day volume (2014) for the constant area and volume-area scaling approaches, respectively. Adding the mass loss due to calving (1.7 Gt by 2099) slightly increases the volume loss by 2099 to 17 and 21%. These mass losses, including both SMB and calving, translate to 1.3 to 1.7 mm of sea level rise. The predicted mean surface elevation change over PIC by 2099 is 59 to 80 m. If the average rate of mass loss between 2015-2099 is assumed to continue into the future, PIC will disappear entirely by 2435 for the constant area option, and by 2542 for the volume-area scaling option.

4.8 DISCUSSION

Results of our simulations show that the SMB on PIC has become increasingly negative since the mid-1990s (Fig. 4.13), in agreement with in-situ observations and with modeled SMB data on other ice caps in the northern CAA [*Lenaerts et al.*, 2013]. A pronounced increase in the modeled mass loss rate occurred after 2005, which also agrees with ATM altimetry measurements over PIC (Fig. 4.11) and with patterns of mass change over the entire CAA derived from satellite elevation changes (ICESat), gravity measurements (GRACE) and SMB modelling results [*Gardner et al.*, 2011]. Ten-year running means of the modeled SMB for PIC are negative for the entire study period (1959-2099), supporting projections of irreversible mass losses of Canadian Arctic Archipelago glaciers [*Lenaerts et al.*, 2013]. PIC is expected to lose 16-20% of its present-day volume by 2099. This matches the bulk glacier volume loss of 18% for the whole southern CAA predicted by *Lenaerts et al.* [2013] using the same RCP4.5 scenario and RACMO2 climate data set.

To assess the sensitivity of the projected SMB for PIC to climatic factors, simulations were performed over the period 2014 to 2099 for four different temperature and precipitation scenarios. Temperature offsets (+1°C, +2°C, -1°C, -2°C) were added to each daily temperature in the adjusted RACMO2.1 dataset. Likewise, precipitation offsets (+10%, +20%, -10%, -20%) were applied to the RACMO2.1 precipitation dataset. Results of these experiments (Fig. 4.18) show that the future SMB is far more sensitive to temperature changes than to precipitation changes. The cumulative SMB varies by a maximum of 1067 Gt by 2099 between the most extreme temperature scenarios (Fig. 4.18a), but by only 104 Gt between the most extreme precipitation scenarios (Fig. 4.18c).

When volume-area scaling is implemented in the model, the projected cumulative SMB for 2099 is reduced by 20% under the RCP4.5 scenario (from -592.8 to -472.9 Gt), and by 26% with the additional +2°C perturbation (from -1183.0 to -874.2 Gt). If the average rate of mass loss between 2015-2099 for the +2°C perturbation scenario is assumed to continue into the future, PIC is expected to disappear sometime between 2225 and 2300.

Regardless of the climate scenario considered or model configuration, the melt rate on PIC is projected to peak in the late 2070s (Fig. 4.13b). For comparison, *Radic and Hock* [2011] predicted that mass losses for glaciers and ice caps worldwide will peak in the 2040s, and *Marzeion et al.* [2012] predict a globally-averaged glacier peak melt rate between ~2050-2060 under RCP4.5. A later peak melt compared to PIC is logical since *Radic and Hock* [2011] used a climate forcing (A1B scenario) where temperature stabilizes earlier (~2060) and they modelled glaciers, as opposed to ice caps, which are more sensitive to volume area feedbacks [*Bahr et al.*, 2015].

The SMB model in this study performed well in comparison to: (a) measured SMB during the calibration period (r^2 = 0.77, RMSE = 0.45 m w.e.), (b) historical SMB measurements on Highway Glacier (r^2 = 0.93, RMSE = 0.21 m w.e.), and (c) ATM altimetry data measurements over the period 1995-2005 (Fig. 4.10, 4.11, 4.12). The rapid upglacier migration of the end of summer snowline over the period 1975-2014 (Fig. 4.5) provides an independent validation that the increased melt predicted by DETIM over the last few decades is realistic.

While the model performed well when compared to historical and recent observations, it does have several limitations, and further work is required to improve DETIM and expand its application. Two significant issues are that the present version of the model does not properly account for the two most important feedbacks for long-term SMB modeling: retreat (negative feedback) and elevation change (positive feedback). Detailed studies on White Glacier (Axel Heiberg Island) over the period 1960-2014 suggest that on this glacier, retreat has had a larger impact on SMB than elevation changes [*Thomson et al.*, 2016]. In the future, elevation change may have a larger influence. For the Yakutat Glacier in Alaska, the positive elevation change feedback dominates in a warming climate [*Trussel et al.*, 2015]. In the present study, we accounted for retreat with a volume-area scaling method (section 4.3.2) that assumes that all volume loss is compensated through marginal retreat. For more realistic results, the scaling

parameter C could be optimized to match glacier outlines. The elevation feedback was not included in the version of DETIM used here, but a parameterization by *Huss et al.* [2010] has since been incorporated into the latest version. The parameterization has not been tested on ice caps, however, so thorough validation against measured data on PIC would be required prior to applying this new model version.

Additional data are also required to improve ice thickness inputs and refreezing parameterizations. The modeled ice thicknesses for PIC [*Huss and Farinotti*, 2012] used here provide thicknesses with a spatial distribution similar to measured values, but individual measurements can differ by up to 800 m compared to measured thicknesses, and obvious discontinuities exist between individual drainage basins (Fig. 4.6). Ice thicknesses derived from NASA IceBridge flights are available from transects across the upper part of PIC, but not along major outlet glaciers. Additional measurements along these glaciers are therefore needed for improved elevation feedback parameterization and for calibrating the theoretical maximum retreat with volume-area scaling. Given that refreezing of meltwater has become an increasingly important process on PIC in recent decades [*Zdanowicz et al.*, 2012; *Schaffer et al.*, in review-b], estimates of the mass loss should account for internal accumulation via refreezing. A distributed model of refreezing would be needed, and additional ice cores collected at various elevations would be required to calibrate it. A model based on the cold content and pore space (e.g. *Reijmer et al.*, 2012), or a more complex one including the physics to describe the temperature profile in firn, could be applied (e.g. *Huss and Hock*, 2015).

This study is based on the RCP4.5 mid-range greenhouse gas emission scenario under which the resulting radiative forcing (and temperature) stabilizes by 2100. In future runs, DETIM should also be tested using alternative climate scenarios to capture the full range of possible outcomes. If the RACMO2.3 data become available, these should be used to model forward, since these temperature and precipitation data are better correlated than RACMO2.1 with the in-situ measurements on PIC. As shown earlier, the modeled SMB for Glacier 1 is highly correlated with that of PIC as a whole ($r = 0.9995$). However, in order to estimate the future contribution of ice cap surface melt to a particular catchment (e.g. Akshayuk Pass), other outlet glaciers would need to be modeled.

4.9 CONCLUSIONS

This study is the first to model the SMB over PIC using spatially-distributed data obtained from the ice cap itself. To calibrate DETIM, a comprehensive dataset of in-situ SMB measurements covering a representative range of elevations, slopes and aspects was used, as well as ATM altimetry data. DETIM inputs and SMB outputs were validated with several independent datasets including SMB data, ATM altimetry and firn cores covering the entire historical modeling period (1959-2004). The spatial resolution of the SMB outputs (~60 m) is a significant improvement over the 11 km resolution provided in an earlier, regional-scale study [*Lenaerts et al.*, 2013]. Ice marginal retreat was also accounted for using a volume-area scaling approach. The SMB model in this study performed well when compared to SMB measurements during the calibration period (r^2 = 0.77, RMSE = 0.45 m w.e.), 1953 (r^2 = 0.93, RMSE = 0.21 m w.e.), and gave SMB estimates that were identical, within error limits, as those inferred from the 1995-2005 ATM altimetry data.

Simulations on PIC show that the SMB has become increasingly negative since the mid-1990s (Fig. 4.13) with a pronounced increase in the modeled mass loss rate since 2005. Peak mass loss is predicted to occur in the late 2070s (Fig. 4.13) and PIC is expected to lose 16-20% of its present-day volume by 2099. The majority of predicted surface mass losses on PIC will occur at elevations between 600 and 1400 m. The refreezing parameterization developed in this study predicts that the surface of PIC will be nearly firn-free by 2100. If the average rate of mass loss between 2015-2099 is assumed to continue into the future, PIC will disappear sometime between 2435 and 2542, under the RCP4.5 scenario.

Sensitivity experiments reveal that the modeled SMB of PIC is far more sensitive to changes in temperature than precipitation. For example, a temperature perturbation of +2°C from the RCP4.5 scenario results in a cumulative increase in mass loss of 590 Gt by 2099, compared to a cumulative increase in mass loss of 52 Gt by 2099 for a 20% reduction in precipitation (Fig. 4.18a, c). Including a volume-area scaling feedback reduces the SMB loss by 20% for the regular scenario and 26% for the +2°C perturbation experiment. For the +2°C perturbation experiment, the ice cap is expected to disappear between 2225 and 2300, >200 years earlier than the regular RCP 4.5 scenario.

Table 4.1: Monthly lapse rates for PIC derived from RACMO2.3 data from 2007-2014. The negative sign indicates a decrease in temperature with increasing elevation.

Month	Jan.	Feb.	Mar.	April	May	June	July	Aug.	Sept.	Oct.	Nov.	Dec.
Lapse rate (°C km^{-1})	-3.9	-4.0	-3.4	-4.5	-5.1	-4.2	-3.8	-4.3	-5.7	-4.9	-5.1	-4.7

Table 4.2: Parameter values for the optimal, maximum (max.) and minimum (min.) parameter combinations for PIC that met the calibration requirements (section 4.5). Modeled outputs were compared to in situ SMB measurements to calculate the RMSE and r^2. The max. and min. correspond to the parameter combinations with the max. and min. ice-cap-wide mass loss rate selected from a range of 13 parameter combinations (Fig. 4.9), respectively. The ice-cap-wide mass loss rate over the same time period derived from ATM data was -4.55 Gt a^{-1} ± ~1.9 Gt a^{-1} using a density of 850 kg m^{-3}.

Month	M_f (mm d^{-1} °C^{-1})	R_{fsnow} (mm m^2 W^{-1} °C^{-1} d^{-1})	R_{fice} (mm m^2 W^{-1} °C^{-1} d^{-1})	T_{snow} °C	**RMSE**	**r^2**	**Mass loss** Gt a^{-1}
Optimal	0.4	0.82	0.62	0	0.45	0.77	-4.43
Max.	1	0.8	0.6	1	0.49	0.73	-4.96
Min.	2.5	0.4	0.2	1	0.5	0.72	-3.88

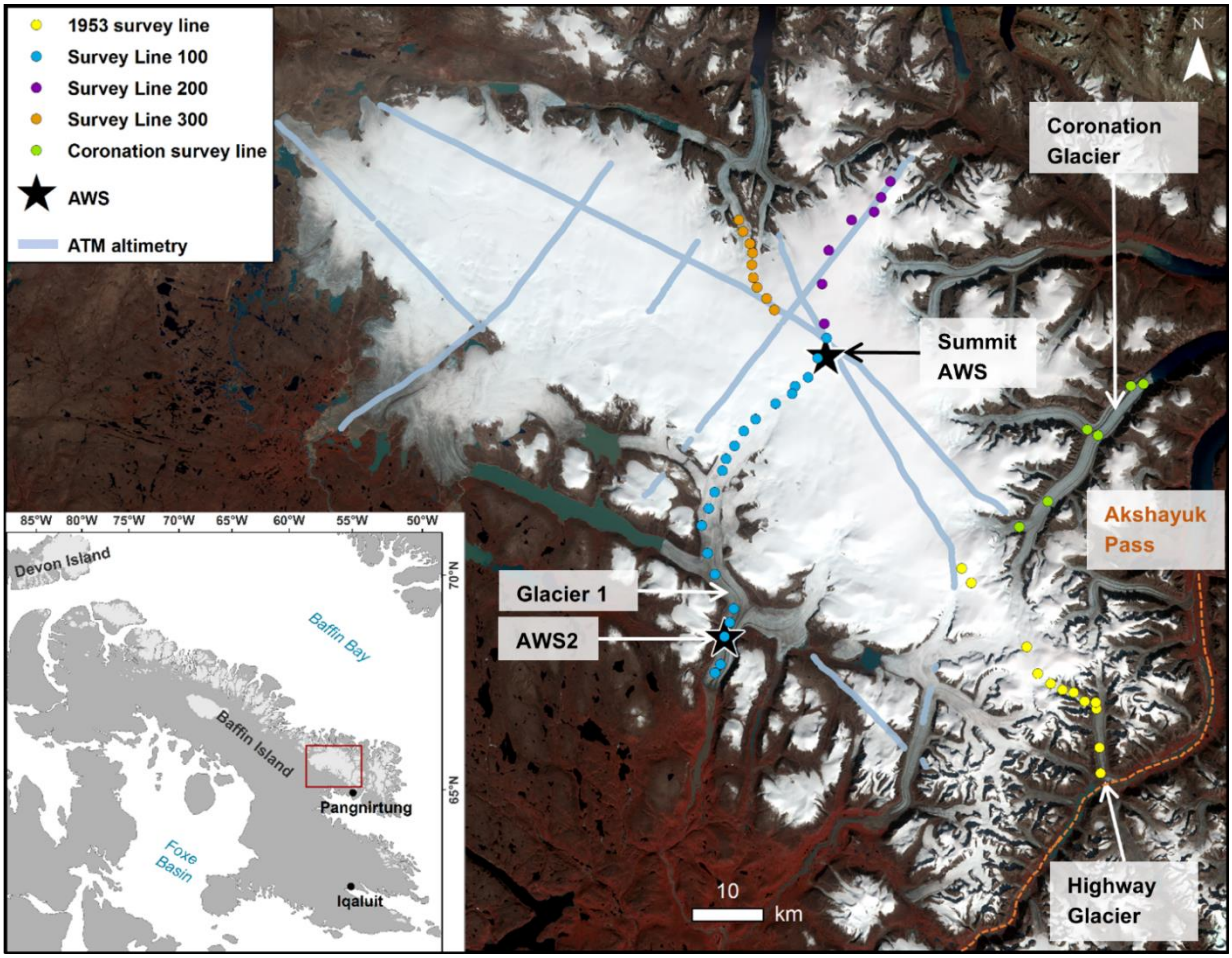

Figure 4.1: Map of Penny Ice Cap (PIC; 67°N, 66°W) showing the five surface mass balance (SMB) survey lines, automatic weather stations (AWS) and ATM altimetry lines. Background image: Landsat 5, August 19, 1985.

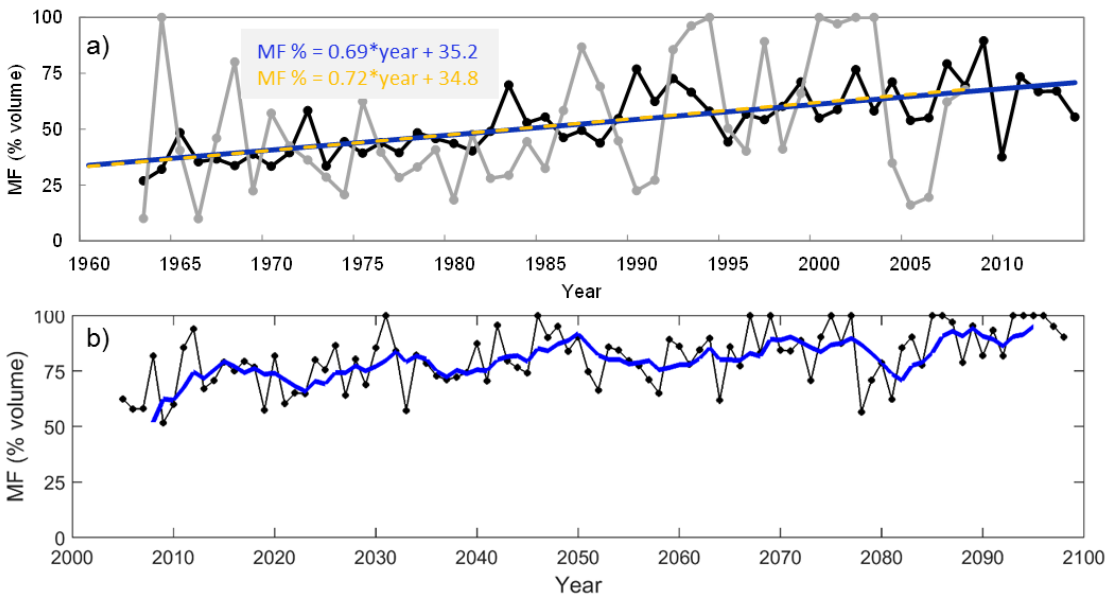

Figure 4.2: Refreezing parameterization outputs for PIC, expressed as a percentage (R / W_r) for: (a) 1963-2014 forced with RACMO2.3 data (black line) and (b) 2005-2098 forced with RACMO2.1 data (5 year running mean in blue). Outputs in (a) are compared to the volumetric percentage of refrozen meltwater ice in firn cores collected near the summit of PIC from 1963-2014 (grey line). The linear regression lines for the modeled (blue line) and measured ice core data (yellow dashed line) are shown.

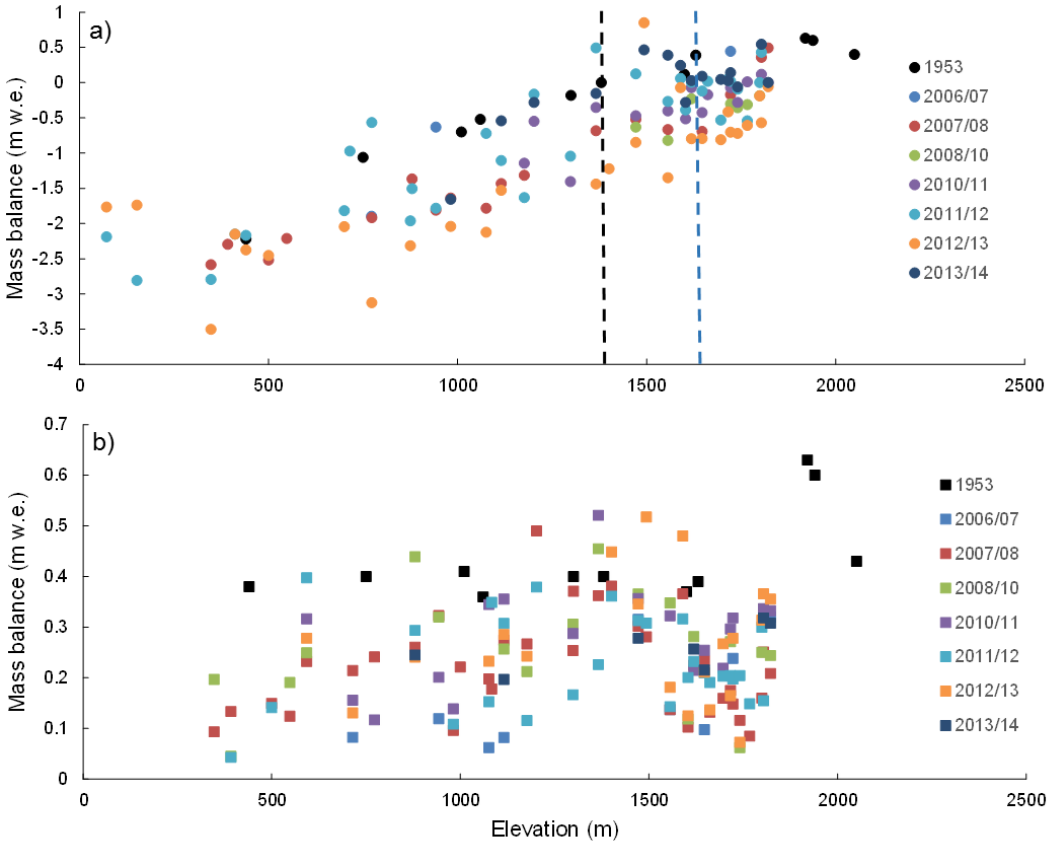

Figure 4.3: (a) Annual SMB measurements and (b) winter snowpack measurements (proxy for winter mass balance) against elevation along five PIC transects between 1953-2014. Survey lines include the 100, 200, 300 lines, Coronation Glacier survey line, plus the 1953 transect along Highway Glacier (Fig. 4.1; *Ward and Baird*, 1954). The horizontal stippled lines give the estimated ELA for 1953 (black; ~1380 m) and 2006-2014 (blue; ~1646).

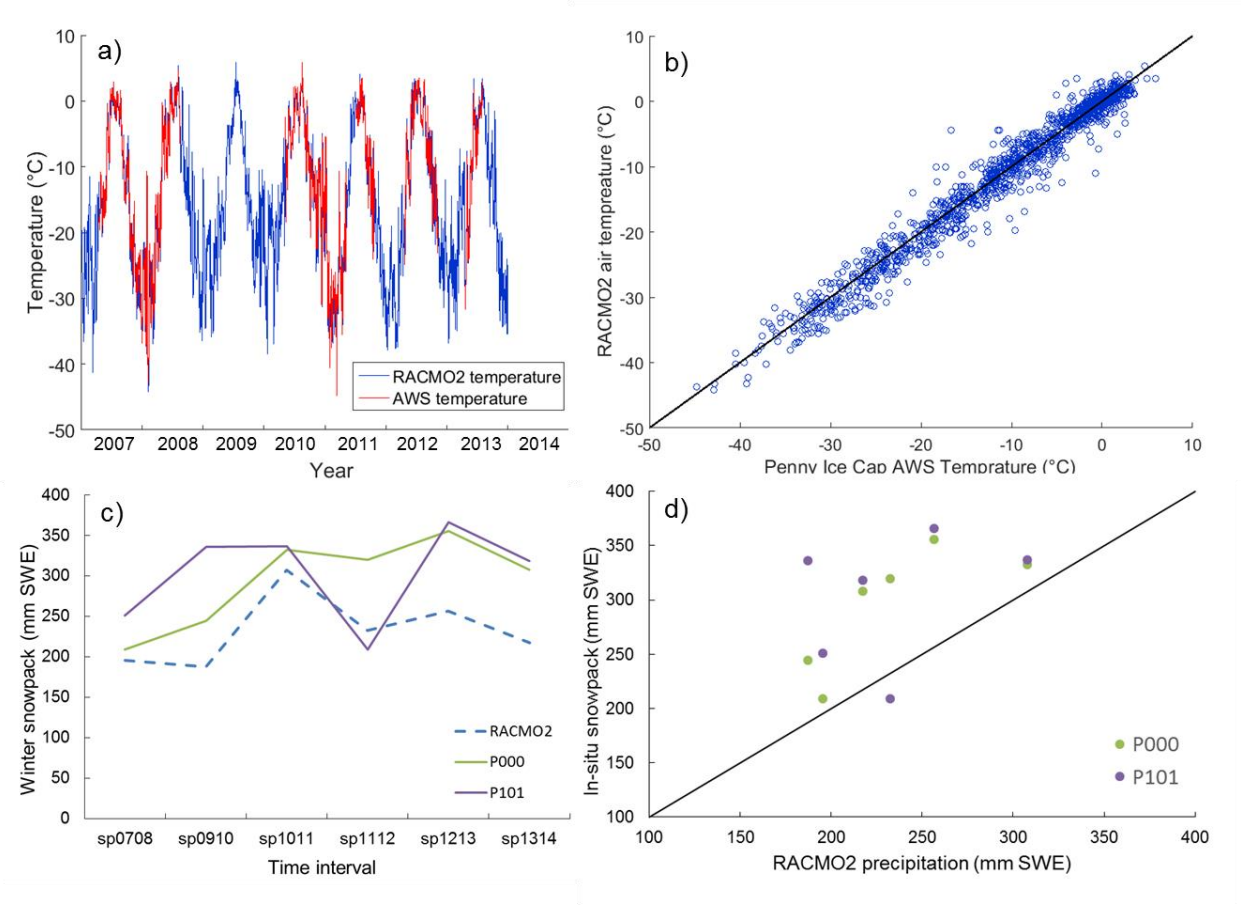

Figure 4.4: (a, b) Comparison between in-situ temperatures measured at the AWS at the summit of PIC (67.3°N, 66.9°W) and the modeled 2 m air temperature outputs from the overlapping RACMO2.3 grid cell. (c, d) Comparison between in-situ spring snowpack measurements at SMB survey stakes on PIC closest to the AWS versus RACMO2.3 cumulative winter precipitation. Snowpack measurements represent accumulated snowfall from the end of summer (~Sept.) to spring the following year (~April) and are labeled spYY_1YY_2, where YY_1 and YY_2 are consecutive years.

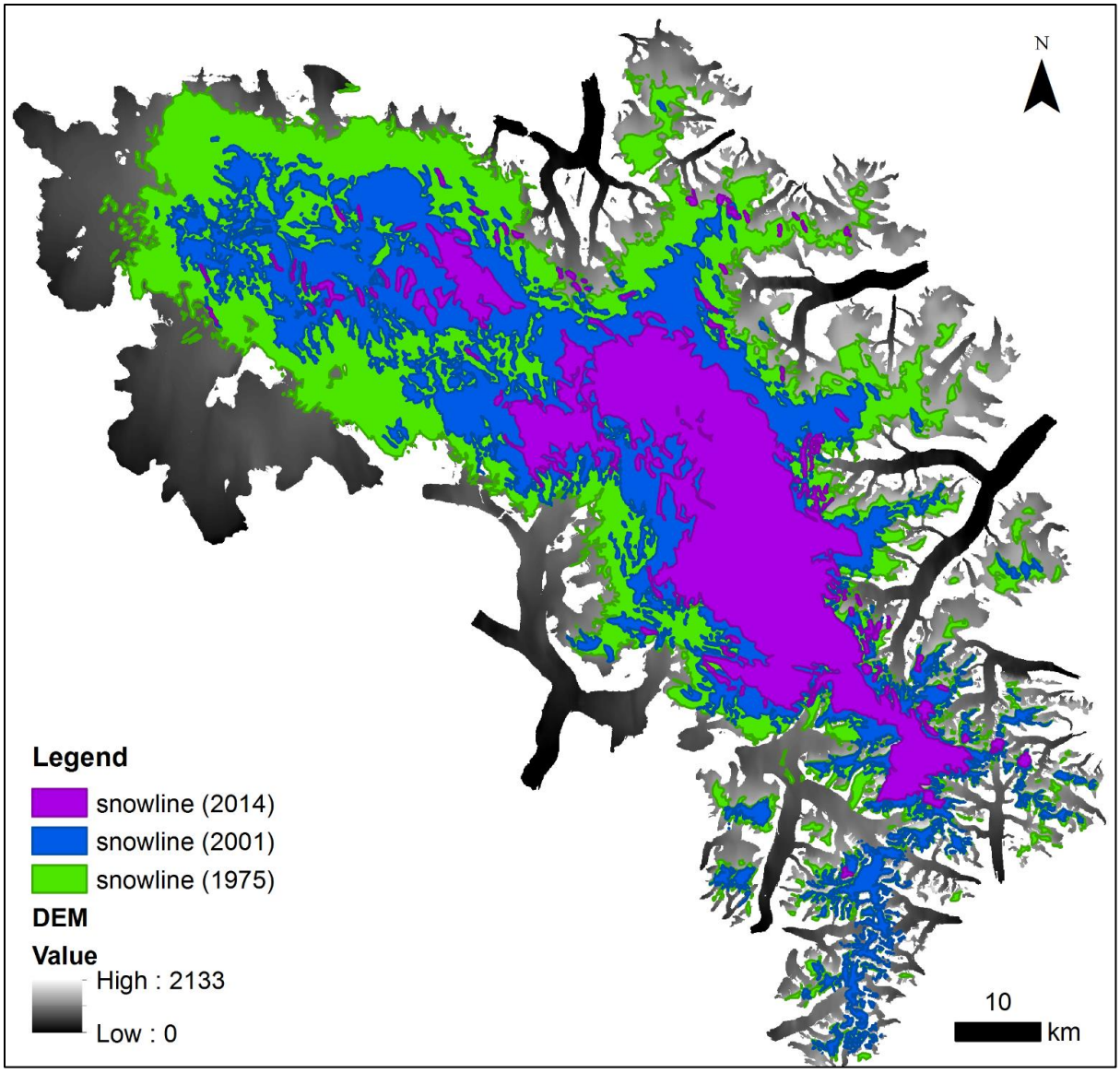

Figure 4.5: End of summer snowline on PIC for 1975, 2001 and 2014 delineated from Landsat imagery with the CDED DEM covering areas of exposed ice.

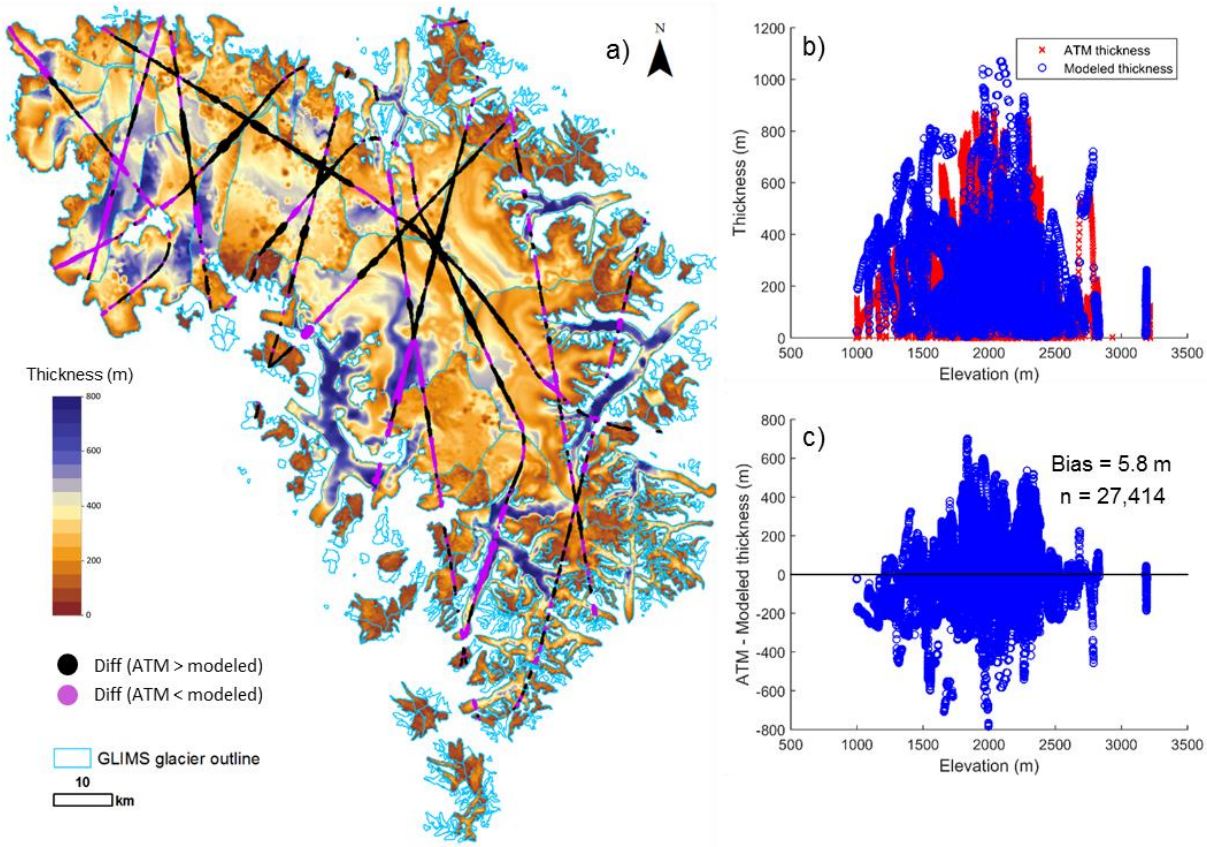

Figure 4.6: a) Modeled ice thicknesses [*Huss and Farinotti*, 2012] with the difference between modeled and point measurements from airborne radar plotted as circles. The size of the circles represent the difference, and range from zero to 800 m, with a positive bias in black and negative bias in purple. b) Measured and modeled thicknesses plotted against elevation. c) Difference between measured and modeled thicknesses with elevation.

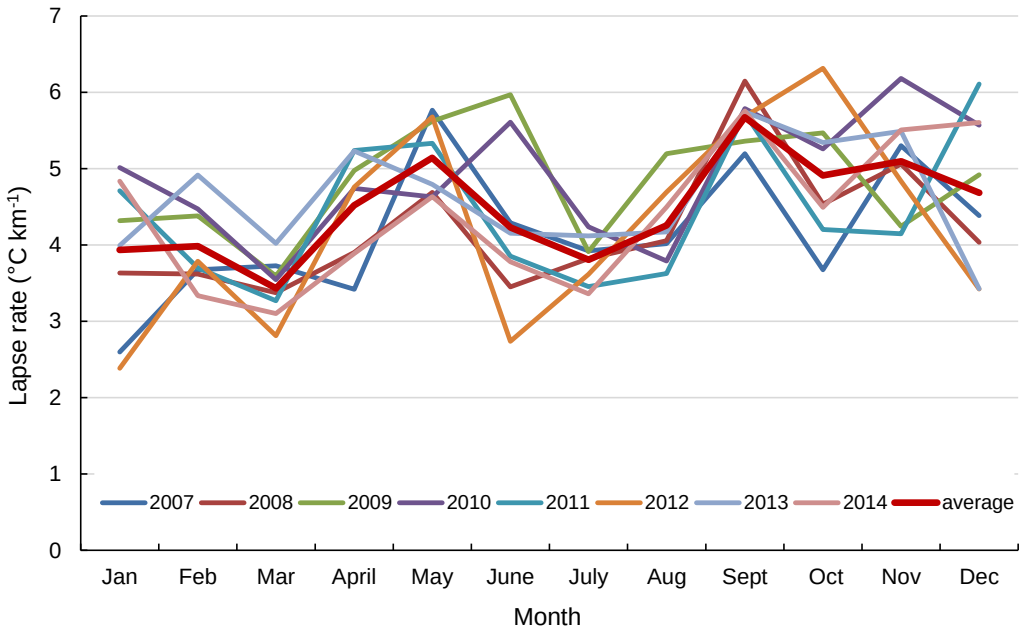

Figure 4.7: Monthly lapse rates for PIC derived from RACMO2.3 data from 2007-2014 and validated with in situ AWS data during July 2010.

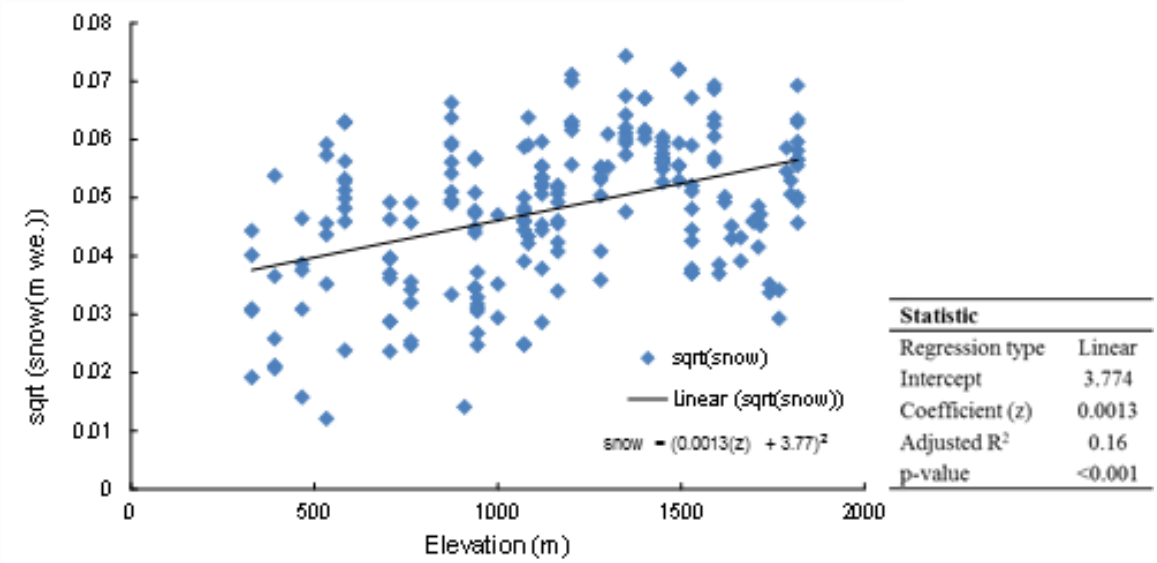

Figure 4.8: Spring snowpack (m w.e.) measurements from 2006-2014 against elevation (z) and associated linear regression line. The square root of snowpack measurements was used to obtain normally distributed residuals. The associated regression coefficients are provided in the inset table.

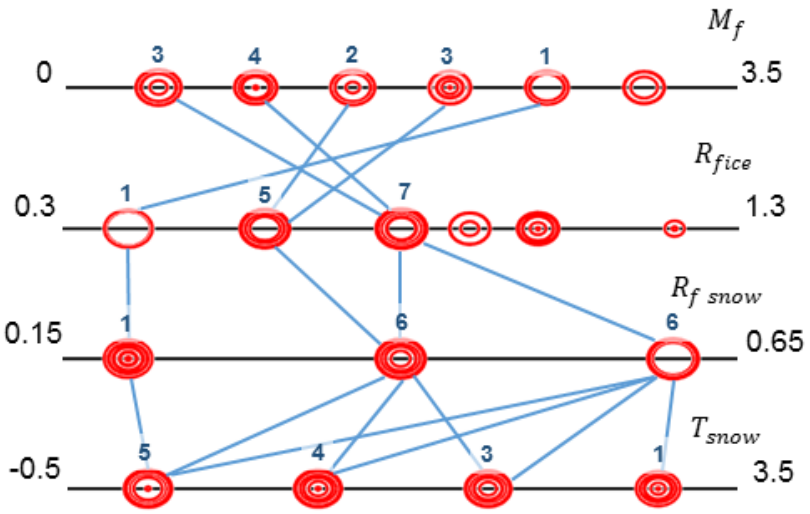

Figure 4.9: Range of tested parameter combinations (black line) that meet the requirements (section 4.5). A larger circle size indicates a better fit (higher r^2 and lower RMSE). Thirty four of the combinations had an RMSE > 0.5 and 13 had an RMSE <= 0.5 m w.e. These 13 combinations are connected with a line and each parameter value is labeled with the number of times it was used.

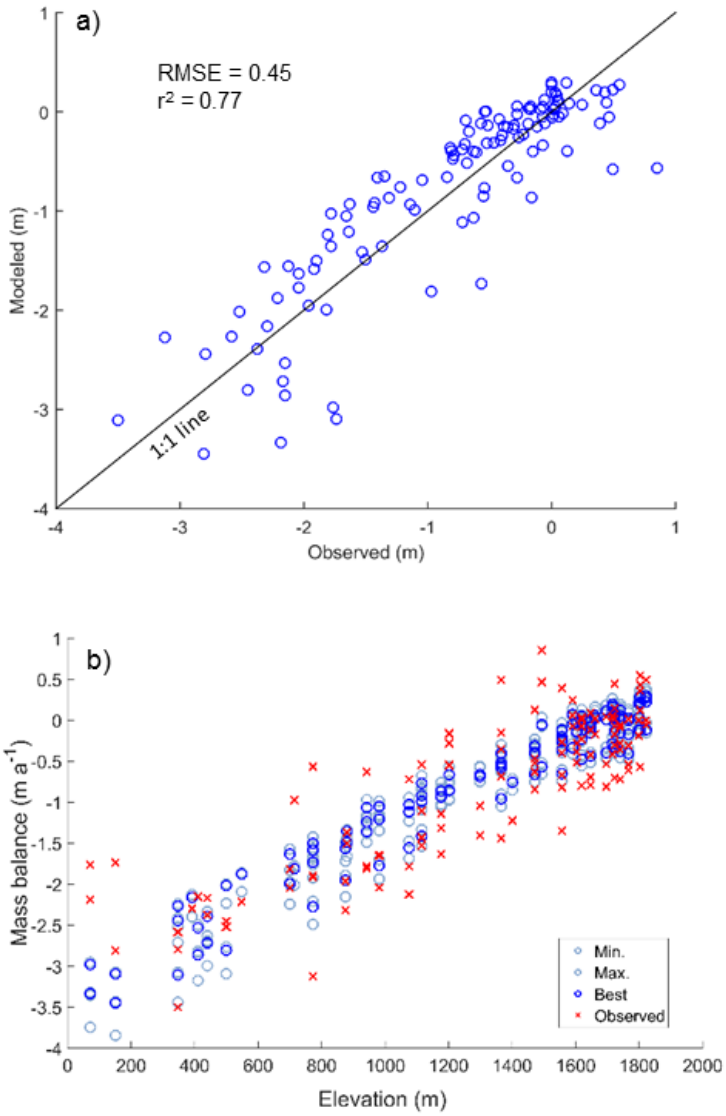

Figure 4.10: Observed stake measurements and corresponding modeled values for a) the optimal parameter combination; b) the optimal, minimum and maximum parameter combinations plotted against elevation for the period 2005-2013.

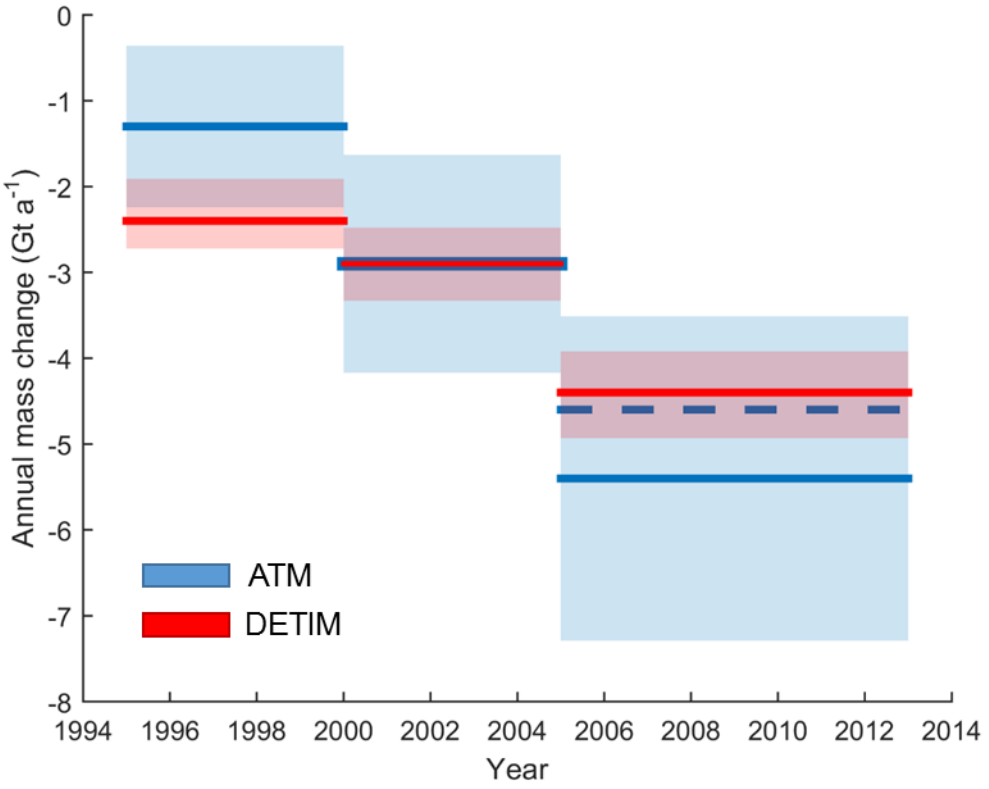

Figure 4.11: Estimates of mass change over PIC during the period1995-2013 from ATM data and DETIM model outputs. Shaded portions represent the 95% confidence intervals for the ATM data (blue) and the range of mass loss estimates obtained from the 13 DETIM parameter combinations (red). The bold red lines show the mass change obtained with the optimal DETIM parameter combination. The dotted blue line represents the mass change inferred from the 2005-2013 ATM data adjusted for firn densification [*Schaffer et al.*, in review-b], which was used for the model calibration.

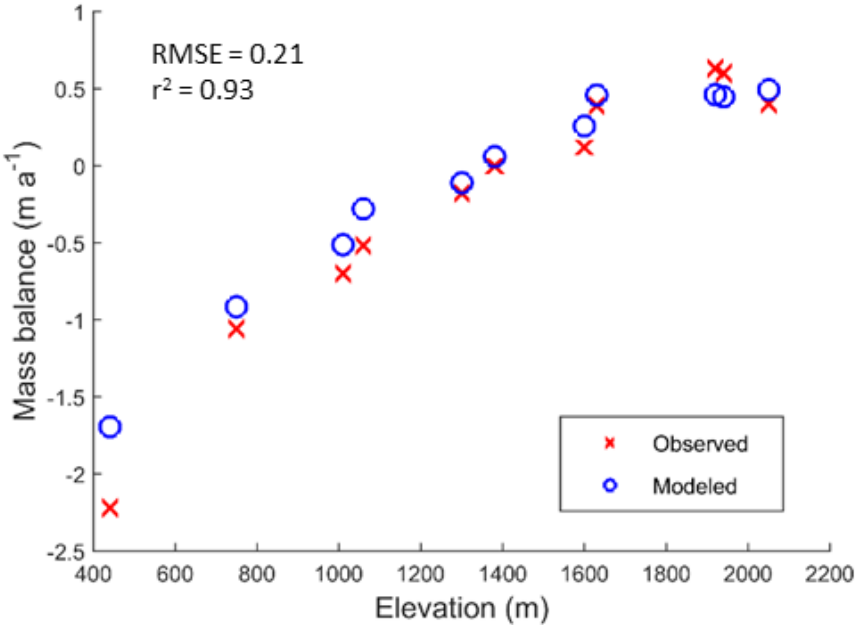

Figure 4.12: Measured SMB on Highway Glacier in 1953, compared to the DETIM model SMB output obtained at the same locations in 1959, using the optimal parameter combination.

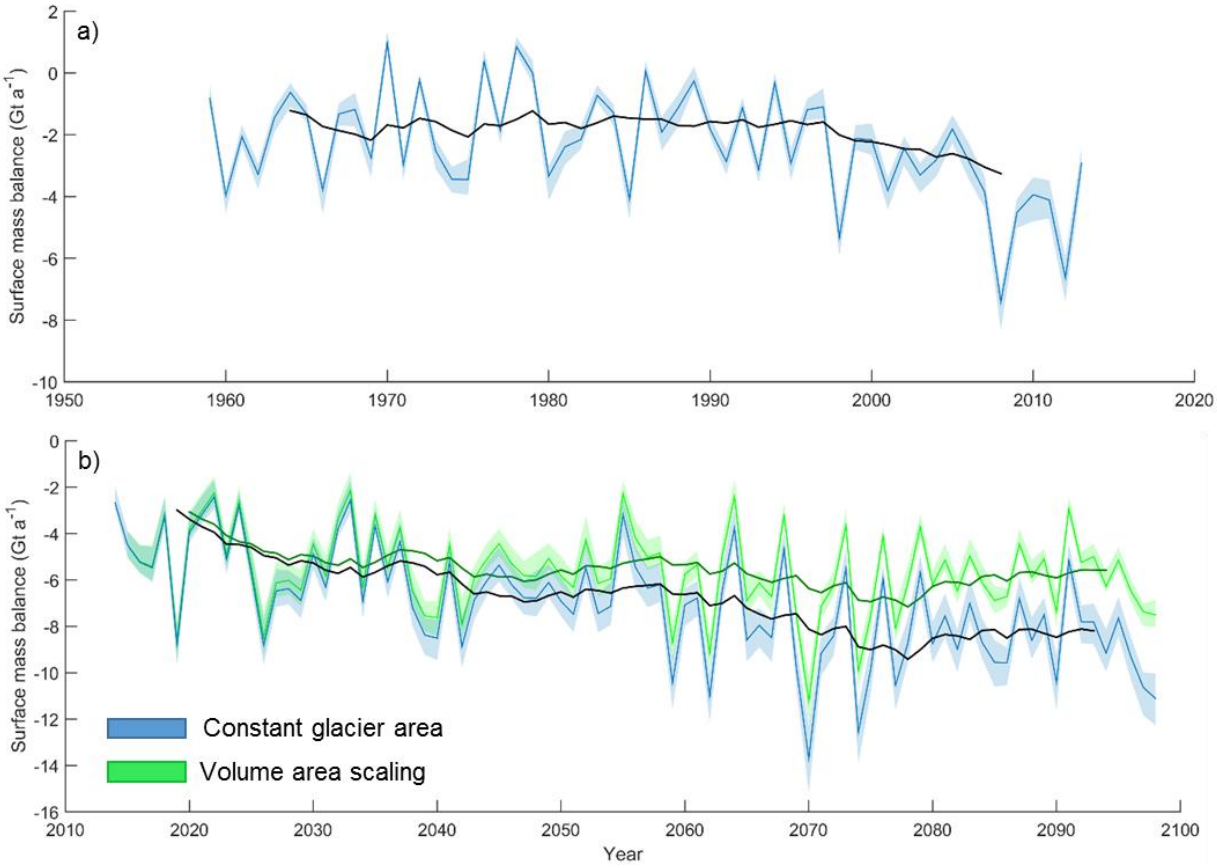

Figure 4.13: Annual modeled SMB for PIC between: a) 1959-2013, and b) 2014-2099. The solid line is the optimal model parameter combination while the shaded portion shows the range covered by the 13 parameter combinations. A constant glacier area was assumed for the dark blue series in both figures, while volume-area scaling was applied to the green series in b). Calving would add an additional 0.02 Gt a^{-1} of mass loss. The thicker lines are 10-year running means.

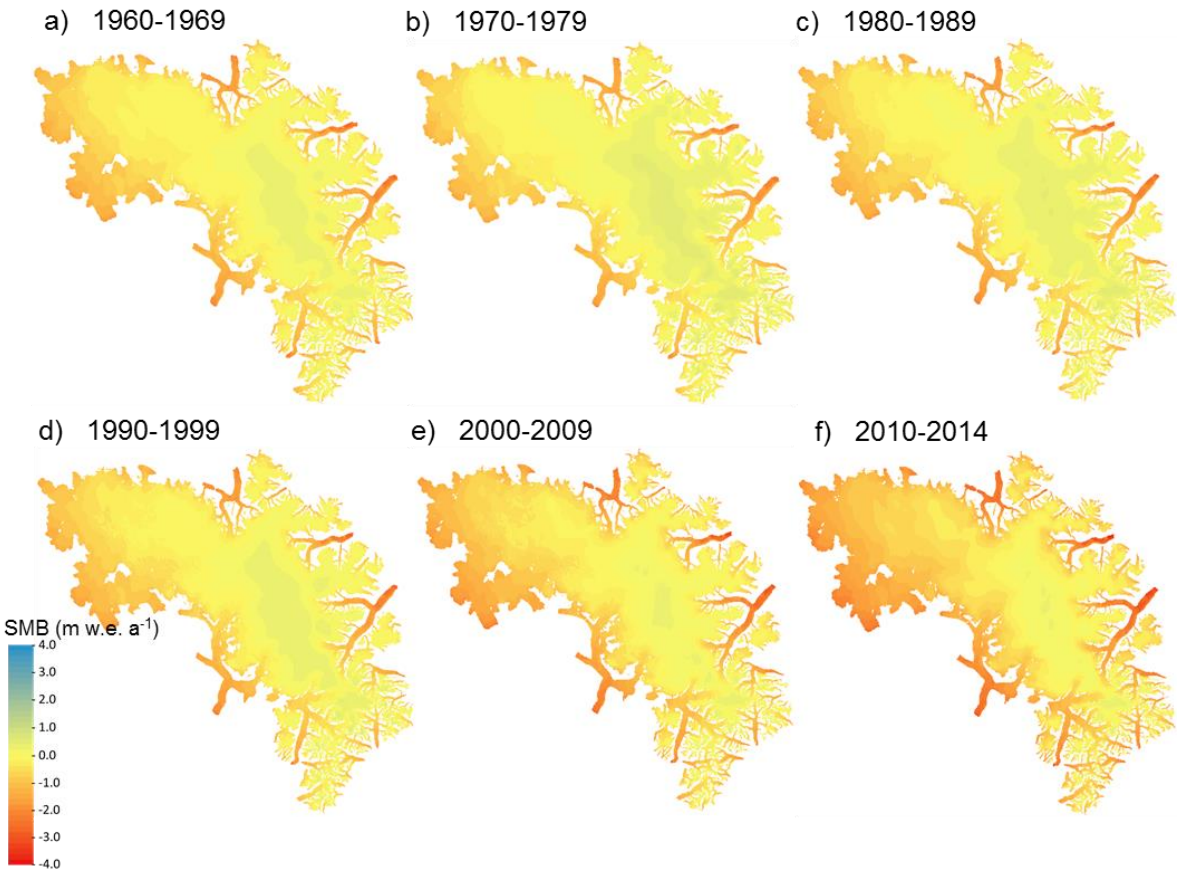

Figure 4.14: Decadal averages of the SMB over PIC modeled for the period 1960 to 2014. For the last interval (2010-14), values shown are the 5-year means.

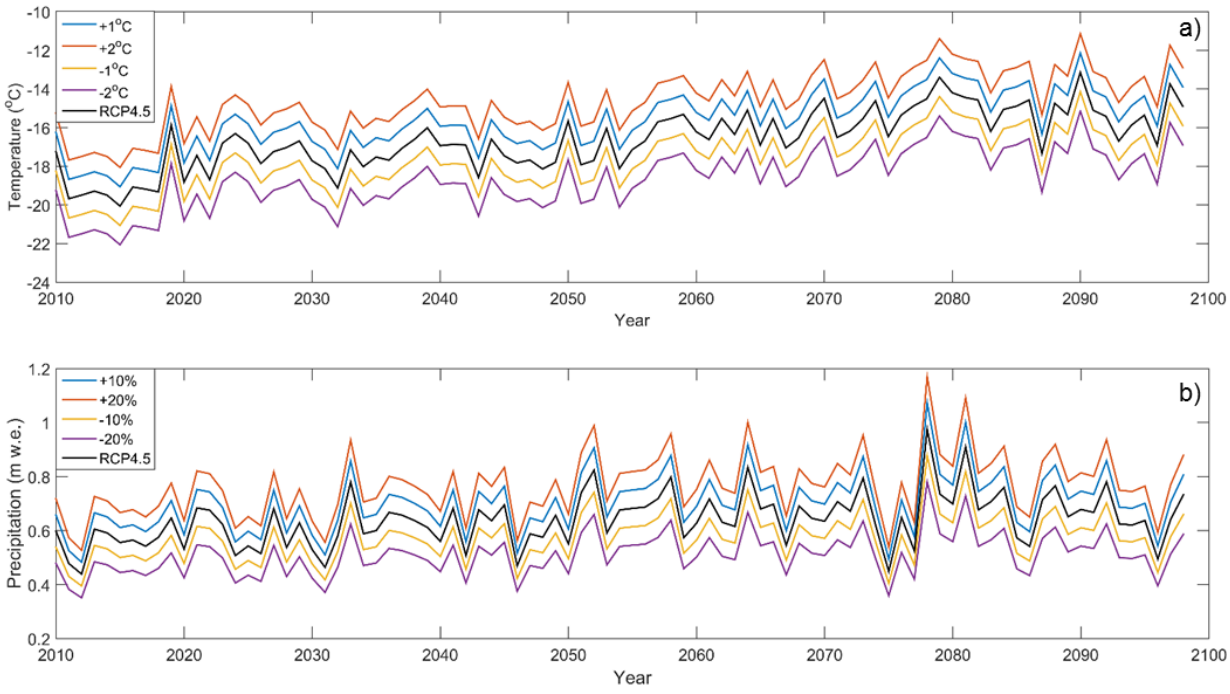

Figure. 4.15: a) Annual average temperature and b) total precipitation for 2010-2098 for the RCP4.5 climate scenario (black), and offsets (coloured lines). Data are from RACMO2.1 climate outputs for the grid cell overlapping the AWS at the summit of PIC.

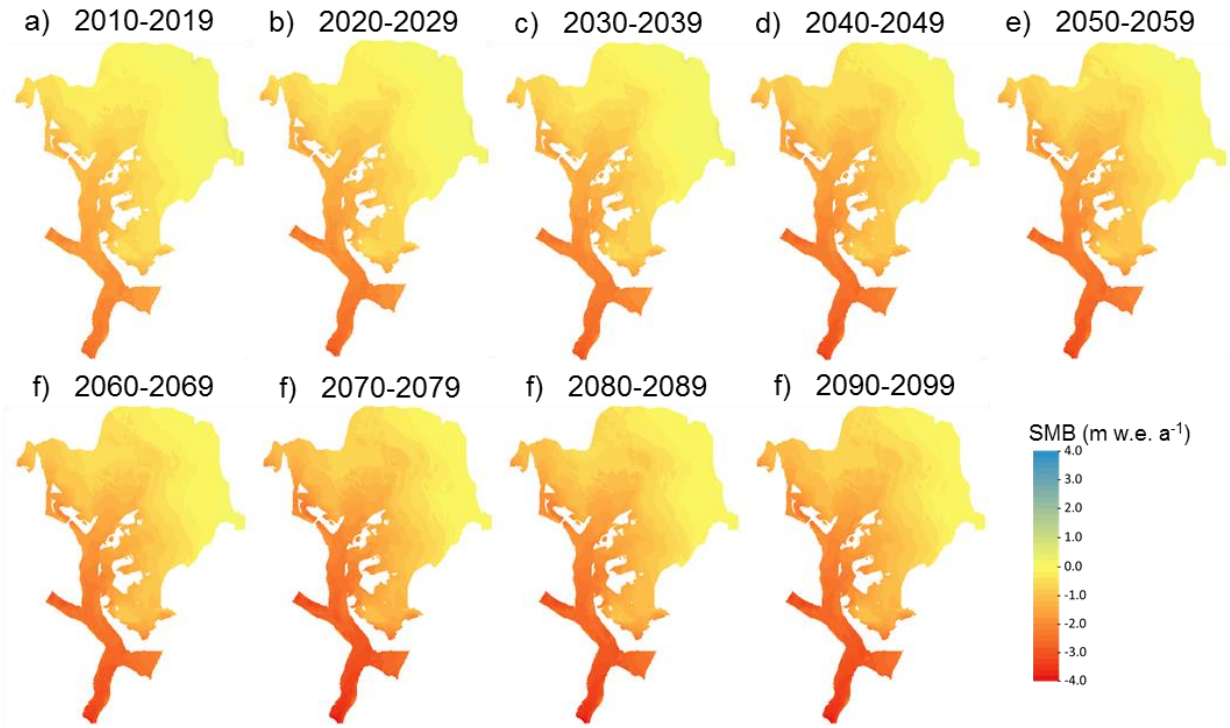

Figure 4.16: Modeled SMB for the period 2010 to 2099 for Glacier 1 with a constant glacier area. Ten year averages are shown.

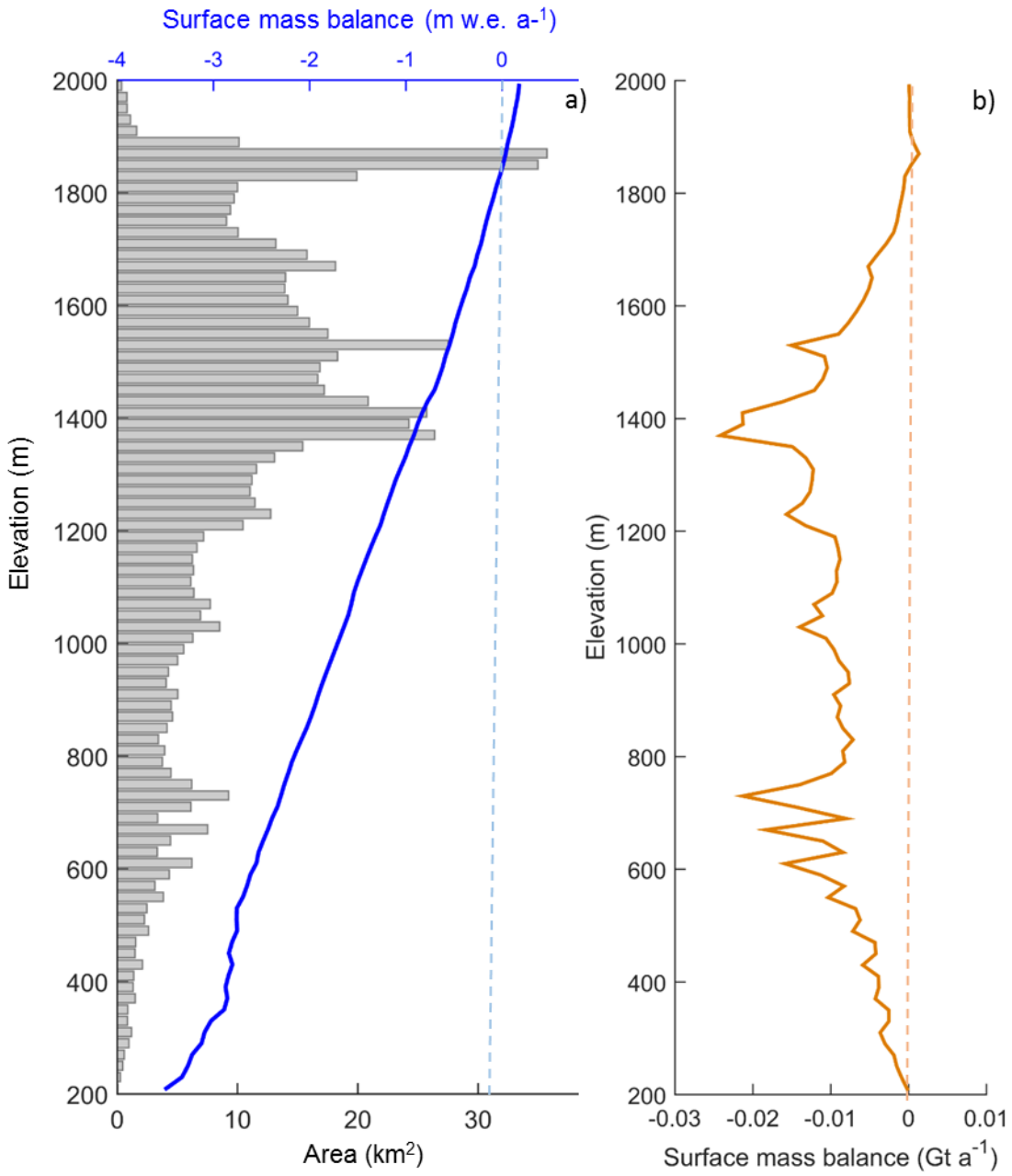

Figure 4.17: (a) Glacier 1 hypsometry (grey bars) and average rate of change in surface height (m w.e. a^{-1}) over the period 2010-2099 and (b) mass loss rate (Gt a^{-1}) for each 20 m elevation band.

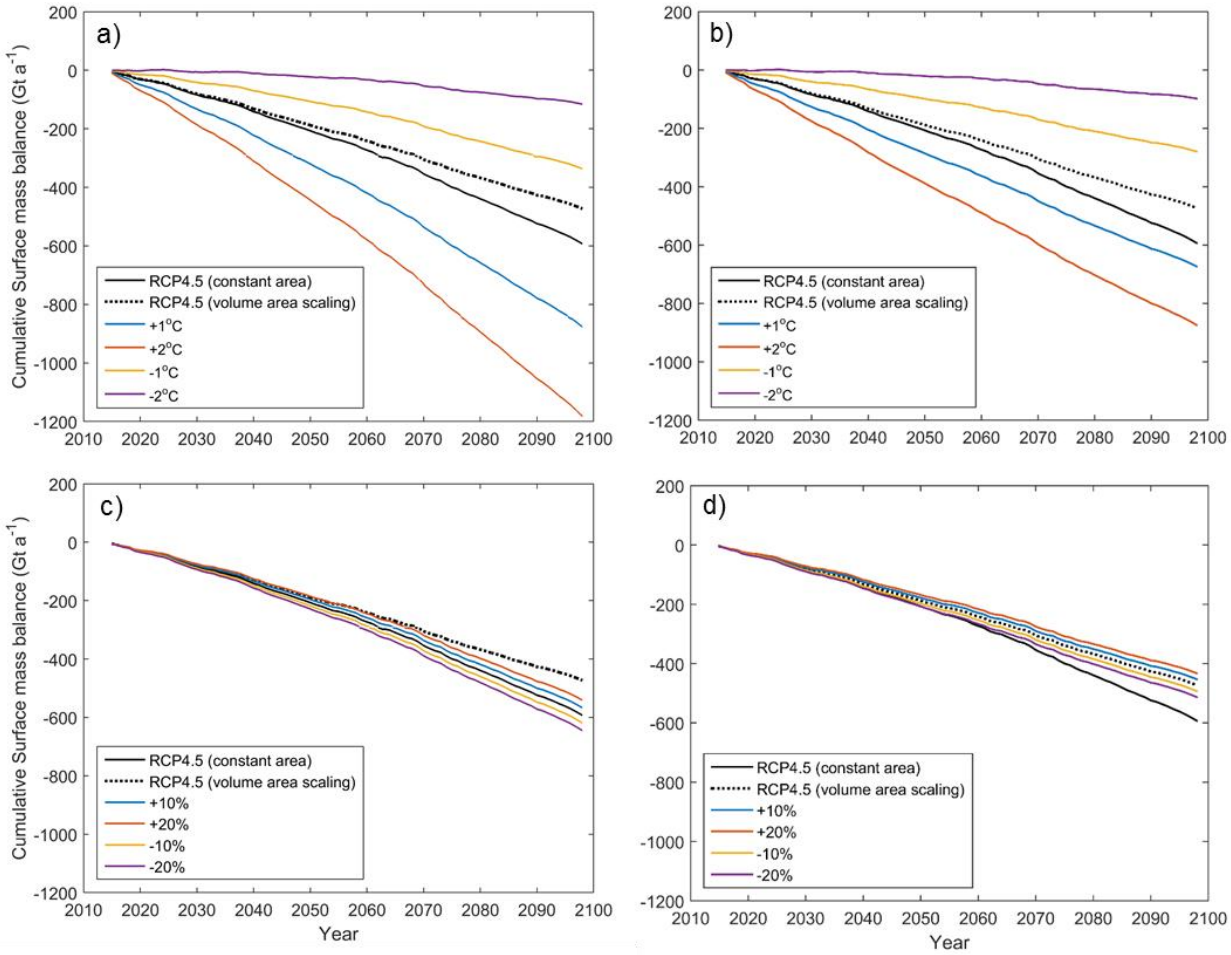

Figure 4.18: Cumulative modeled surface mass balance for the period 2015 to 2099 for a) four temperature scenarios, b) four temperature scenarios with volume area scaling, c) four precipitation scenarios and d) four precipitation scenarios with volume area scaling. Outputs using the unmodified RACMO2.1 data are plotted as black solid and dashed lines for the constant area and volume area scaling scenarios, respectively.

CHAPTER 5: CONCLUSIONS

5.1 SUMMARY AND CONCLUSIONS

This thesis has quantified changes in the mass loss rate of PIC from 2005-2014, determined the velocity response of the ice cap to changes in surface melt since the early 1950s, and modeled the ice-cap-wide mass balance from 1958 to 2099 using a modified temperature index model. Changes in glacier mass loss rates were inferred from volume changes calculated from 2005, 2013 and 2014 ATM surface altimetry measurements. The volume change from 2005-2013 was corrected for vertical ice velocity to isolate the elevation change due to mass loss alone. These calculations indicate that the mass loss for PIC inferred from ATM altimetry data may be overestimated by 15% if the observed elevation changes are not corrected for the effects of increased melt/refreezing rates, and by a further 4% if ice dynamics are ignored. Correcting the data for vertical ice motion has the effect of increasing the mass loss at lower elevations and decreasing it at higher elevations, and these estimates are insensitive to the assumed density in the firn zone (900 or 800 kg m^{-3}). There has been a four-fold increase in the mass loss rate over PIC from the mid-1990s (-1.3 ± 0.7 Gt a-1) to the period 2005-2013 (-5.4 ± 1.9 Gt a^{-1}). This increased mass loss rate has coincided with a relatively rapid upglacier migration of the equilibrium line, leaving large areas of sub-surface firn in the current ablation area, >400 vertical meters below the current ELA of ~1646 m. The firn-ice transition at ~1300 m a.s.l. is much closer to the 1953 ELA (~1380 m a.s.l.) on Highway Glacier, suggesting a delayed response to the recent increase in melt rates. The position of the dynamic equilibrium line, >300 m below the current ELA, also suggests that the ice cap has not yet adjusted dynamically to its recent mass changes.

The spatial patterns and long-term changes in surface velocity over PIC were mapped using optical and radar satellite imagery from 1985-2014, and compared with historical ground measurements from 1953. An ice-cap-wide velocity map produced for 2011/2012 showed that most of PIC is slow-moving (<20 m a^{-1}), with faster motion restricted to areas of high relief where the broad accumulation area connects to topographically constrained outlet glaciers. Velocities on outlet glaciers ranged from ~100 - 250 m a^{-1} and generally decreased down-glacier. The exception to this pattern was tidewater-terminating glaciers, which showed a distinct increase in velocities in their lowest terminus region. The six largest outlet glaciers on the ice cap

decelerated at an average rate of 21 m a^{-1} between 1985-2010, or 12% $decade^{-1}$. Within that period most glaciers accelerated until the 1990s, and decelerated afterwards. The measured decelerations were greater than the total short-term variability of surface velocities associated with seasonal and interannual fluctuations. Historical ice velocity measurements on Highway Glacier provided a longer-term perspective, and revealed that this glacier decelerated by 71% between 1953 and 2009/11, from 57 m a^{-1} to 17 m a^{-1}. The recent slowdown of PIC outlet glaciers has coincided with increases in mass loss, terminus retreat and an inferred reduction in basal sliding, supporting the hypothesis that glacier thinning and/or increased meltwater production promotes a long-term reduction in ice motion.

The surface mass balance of PIC from 1958 to 2099 was modeled with an enhanced temperature index model calibrated with in situ data from 2006-2014. The model performs well when compared to SMB measurements during the calibration period (r^2 = 0.77, RMSE = 0.45 m w.e.), 1953 (r^2 = 0.93, RMSE = 0.21 m w.e.), and gives the same SMB, within error limits, as the 1995-2005 airborne altimetry data. Modeled mass balance rates become increasingly negative after the mid-1990s, particularly since 2005. Maximum mass loss occurs in the late 2070s for the midrange RCP4.5 climate scenario. Over the entire modeled period (1958-2099), the ten year running mean of modeled SMB is negative, supporting the conclusion that there will be irreversible mass loss of Canadian Arctic Archipelago glaciers [*Lenaerts et al.*, 2013]. By 2099, PIC is expected to lose 16-20% of its initial 2014 volume for the volume-area scaling and constant area scenarios, respectively. When a +2°C offset is applied to the RCP4.5 data set, the ice cap loses 30-40% of its initial 2014 volume by 2099. If the average mass loss rate between 2015-2099 continues into the future, PIC will disappear in ~530 years for the RCP4.5 scenario and in ~290 years if a +2°C perturbation is applied.

5.2 KEY CONTRIBUTIONS

This study has provided the first comprehensive evaluation of the impact of vertical ice motion caused by firn compaction and/or ice dynamics on mass loss estimates inferred from airborne altimetry data over a large Arctic ice cap. Geodetic methods (based on detection of surface elevation changes) have been heavily relied upon to quantify the response of glaciers and ice caps to climate warming over the past few decades [e.g. *Abdalati et al.*, 2004; *Gardner et al.*,

2011, 2012], but few previous studies have assessed whether proper accounting for vertical ice motion is required to determine accurate mass loss rates. Several studies have sought to model the firn densification rate ($\dot{\rho}$) and quantify the contribution to observed $\dot{h}$ in the dry snow zones of GIS and Antarctica [*Cuffey*, 2001; *Zwally and Li*, 2002; *Li et al.*, 2003; *Shepherd et al.*, 2012; *Gardner et al.*, 2013; *Morris and Wingham*, 2014; *Ligtenberg et al.*, 2015]. Some geodetic studies have also incorporated densification into the error estimate for mass change calculations above the ELA [*Gardner et al.*, 2012]. Studies on individual alpine glaciers have reported an over-estimation of mass losses inferred from geodetic compared to direct SMB measurements (glaciological method) [*Krimmel*, 1999; *Beedle et al.*, 2014]. However, such comparisons have only been previously completed for individual glaciers and not over an entire ice cap. Furthermore, this study used a large variety of data sets including airborne altimetry, ICESat, dGPS, GPR, Envisat, SMB and ice core data to produce and substantiate the results.

A multi-decadal record of ice surface velocity variations on PIC since the 1950s was produced and compared to historical SMB data to provide insights into the relationship between surface melt rates and glacier motion over the past 30-60 years on one of the largest ice caps in the CAA. An ice-cap-wide velocity map for 2011/2012 was produced and temporal variations in ice motion along the centre flow line and several transverse profiles for key outlet glaciers were investigated. This study provides a more complete analysis than the previous study by Heid & Kääb (2012b), which only focused on velocity changes at point locations on parts of 12 PIC outlet glaciers between 1985 and 2011. The long-term velocity trends for the whole of PIC were consistent with those found by Heid and Kääb (2012b), who reported an overall deceleration of glaciers over 1985-2010, with an initial period of acceleration between 1985 to 1998, followed by deceleration. The present study also examined velocity changes on Highway Glacier since 1953, providing a longer term record of ice velocity variability. For this glacier, ice motion due to deformation was calculated by applying Glen's flow law in 1953 and 2010. The decreasing influence of basal sliding was inferred from the increased dominance of ice flow due to deformation calculated over time, providing insight into the mechanism behind glacier deceleration. This study contributes to a growing body of literature documenting that the majority of land-terminating glaciers are decelerating in response to a warming climate [*Thomson and Copland*, in press; *Vincent et al.*, 2009; *Heid and Kääb*, 2012b; *Tedstone et al.*, 2015; *Waechter et al.*, 2015; *Wilson et al.*, 2016].

Previous projections of mass change for glaciers in the southern Canadian Arctic Archipelago over the next century have been approximate as there have been no studies published that have used spatially distributed data to calibrate or validate mass balance models there, despite rapid mass loss observed over the past few decades. In this study the SMB over PIC was modeled from 1958 to 2099 using a model calibrated with a comprehensive SMB dataset totaling 140 measurements covering a representative range of elevations, slopes and aspects as well as ATM altimetry data. The model was thoroughly validated with SMB data, ATM altimetry and ice cores covering the entire historical modeling period (1959-2004). The resolution of SMB outputs is ~60 m, a notable improvement over the 11 km resolution provided in the only other study to model the SMB of PIC at a regional scale [*Lenaerts et al.*, 2013]. These model outputs show an increasingly negative mass balance since the mid-1990s, matching observations of in-situ and modeled SMB for Agassiz, Devon and Melville Ice Caps in the northern Canadian Arctic Archipelago [*Lenaerts et al.*, 2013]. The pronounced increase in modeled mass loss since 2005 has also been observed with ATM altimetry elevation changes over PIC and patterns of mass change over the entire Canadian Arctic derived from satellite elevation changes (ICESat), gravity measurements (GRACE) and SMB modelling results [*Gardner et al.*, 2011]. The ten year running mean of modeled SMB is negative over the entire model period (1958-2099), supporting the conclusion that there will be irreversible mass loss of Canadian Arctic Archipelago glaciers over the next several centuries [*Lenaerts et al.*, 2013].

5.3 FUTURE WORK

This study has calculated the impact of vertical motion on ice-cap-wide mass loss estimates inferred from airborne altimetry data in the Canadian Arctic. Future studies should investigate the effect of vertical motion further to reduce the uncertainty associated with extrapolating vertical velocities across an ice mass. Measurements of firn densification from ice cores over a range of elevations and a detailed ice-cap-wide grid of dGPS measurements of vertical velocity and horizontal displacement at mass balance stakes would be ideal. It would be critical to pair the dGPS measurements with a kinematic dGPS survey or high resolution surface DEM to accurately determine surface slope since the correction for down-slope movement of mass balance stakes can significantly alter the final vertical velocity values.

To further investigate the causes of the observed velocity slowdowns across PIC (e.g., relative importance of changes in internal deformation vs. basal sliding), additional measurements of ice thickness change and temperature are required over the most dynamically active outlet glaciers (e.g. Glacier 1). Ice thicknesses should be measured with a low frequency ground penetrating radar and one or more AWS and thermistor cables extending to at least 10 m below the ice surface should be installed to measure ice temperatures. Direct measurements of ice deformation and basal ice motion from borehole measurements would be ideal, but very expensive and logistically challenging. Installing a continually operating dGPS would provide insight into seasonal and diurnal velocity fluctuations. Further work is also needed to better understand the cause of deceleration on the two tidewater-terminating glaciers on PIC. Measurements of sea surface temperatures and bathymetry in Baffin Bay, as well as continued monitoring of glacier motion and runoff, are required.

While DETIM performs well when compared to in situ and geodetic measurements of SMB over PIC, further work is required to address several model limitations and expand its application. The most pressing issue is likely that the model does not properly account for the two most important feedbacks for long-term mass balance modeling: retreat (negative feedback) and elevation change (positive feedback). A comprehensive study on White Glacier, Axel Heiberg Island, suggests that retreat currently has a larger impact on mass balance [*Thomson et al.*, 2016], but a study on an Alaskan glacier reports that the positive elevation feedback may have a larger influence in a warming climate [*Trussel et al.*, 2015]. In DETIM, ice retreat is accounted for through a volume-area scaling method that assumes that all volume loss is compensated for through retreat and provides a theoretical upper limit for retreat (section 4.3.2). A more realistic calibration method should be applied based on the best match to glacier outlines. The elevation feedback is not accounted for, but has been incorporated into the latest version of DETIM and could be applied to PIC once thorough validation against measured data has been completed. An improved ice thickness data set would be required to run the elevation feedback and more accurately calibrate the theoretical maximum retreat with volume-area scaling. Modeled ice thicknesses for PIC [*Huss and Farinotti*, 2012] have a distribution of ice thicknesses similar to measured values, but obvious discontinuities exist between individual drainage basins and point measurements may differ by up to 800 m. Measured ice thicknesses from NASA IceBridge flights provide good coverage of the ice cap interior, but do not profile any of the major outlet

glaciers. DETIM should be run for additional climate scenarios including RCP2.6 and RCP8.5 to cover the full range of possible SMB predictions. If the RACMO2.3 data becomes available, this should be used since the climate data is better correlated with the in situ measurements on PIC than RCMO2.1. Although the modeled mass balance for Glacier 1 is highly correlated to that of PIC ($r = 0.9995$), upscaling from one drainage basin does not allow for assessments of the melt contribution to individual catchments. Additional model runs should be completed to cover most, if not all of PIC.

CHAPTER 6: REFERENCES

Abdalati, W., W. Krabill, E. Frederick, S. Manizade, C. Martin, J. Sonntag, R. Swift, R. Thomas, J. Yungel, and R. Koerner (2004), Elevation changes of ice caps in the Canadian Arctic Archipelago, *J. Geophys. Res.*, *109*(F04007), 1–11, doi:10.1029/2003JF000045.

Alley, R. B., P. U. Clark, P. Huybrechts, and I. Joughin (2005), Ice-sheet and sea-level changes, *Science*, *310*, 456–460, doi:10.1126/science.1114613.

AMAP-SWIPA (2011), *Snow, Water, Ice and Permafrost in the Arctic (SWIPA): Climate Change and the Cryosphere.*, Arctic Monitoring and Assessment Program (AMAP), Oslo, Norway.

Anderson, B., I. Willis, B. Goodsell, A. Banwell, I. Owens, A. Mackintosh, and W. Lawson (2014), Annual to daily ice velocity and water pressure variations on Ka Roimata o Hine Hukatere (Franz Josef Glacier), New Zealand, *Arctic, Antarct. Alp. Res.*, *46*(4), 919–932, doi:10.1657/1938-4246-46.4.919.

Van Angelen, J. H., J. T. M. Lenaerts, M. R. Van Den Broeke, X. Fettweis, and E. Van Meijgaard (2013), Rapid loss of firn pore space accelerates 21st century Greenland mass loss, *Geophys. Res. Lett.*, *40*(10), 2109–2113, doi:10.1002/grl.50490.

Anon (2008), "Climate Change in Canada: The Duval River disaster". The Innovator, Newsletter of the International Institute for Sustainable Development (Issue 6 October 2008).,

Arendt, A. (2012), *Randolph Glacier Inventory: A dataset of global glacier outlines, version 2.0, digital media*, digital media, http://www.glims.org/RGI/ RGI_Tech_Report_V2.0.pdf, Global Land Ice Measure from Space, Boulder, Colorado.

Bader, H. (1954), Sorge's law of densification of snow on high polar glaciers, *J. Glaciol.*, *2*(15), 319–323, doi:10.3198/1954JoG2-15-319-323.

Bahr, D. B., W. T. Pfeffer, and G. Kaser (2015), A review of volume-area scaling of glaciers, *Rev. Geophys.*, *53*, 95–140, doi:10.1002/2014RG000470.

Baird, P. D. (1953), Baffin Island expedition, 1953: A preliminary field report, *Arctic*, *6*, 227–251, doi:10.14430/arctic3878.

Bartholomew, I., P. Nienow, A. Sole, D. Mair, T. Cowton, and M. A. King (2012), Short-term variability in Greenland Ice Sheet motion forced by time-varying meltwater drainage: Implications for the relationship between subglacial drainage system behavior and ice velocity, *J. Geophys. Res. Earth Surf.*, *117*(F3), 1–17, doi:10.1029/2011JF002220,2012.

Beedle, M. J., B. Menounos, and R. Wheate (2014), An evaluation of mass-balance methods applied to Castle Creek Glacier, British Columbia, Canada, *J. Glaciol.*, *60*(220), 262–276, doi:10.3189/2014JoG13J091.

Bezeau, P., M. Sharp, D. Burgess, and G. Gascon (2013), Firn profile changes in response to extreme 21st-century melting at Devon Ice Cap, Nunavut, Canada, *J. Glaciol.*, *59*(217), 981–991, doi:10.3189/2013JoG12J208.

Bradley, R. S. (1973), Seasonal Climatic Fluctuations on Baffin Island during the Period of

Instrumental Records, *Arctic*, *26*(3), 230–243.

Brenner, A. C., J. P. DiMarzio, and H. J. Zwally (2007), Precision and accuracy of satellite radar and laser altimeter data over the continental ice sheets, *IEEE Trans. Geosci. Remote Sens.*, *45*, 321–331, doi:10.1109/TGRS.2006.887172.

Burgess, D. O., M. J. Sharp, D. W. F. Mair, J. A. Dowdeswell, and T. J. Benham (2005), Flow dynamics and iceberg calving rates of Devon Ice Cap, Nunavut, Canada, *J. Glaciol.*, *51*(173), 219–230, doi:10.3189/172756505781829430.

Burgess, E. W., C. F. Larsen, and R. R. Forster (2013), Summer melt regulates winter glacier flow speeds throughout Alaska, *Geophys. Res. Lett.*, *40*(23), 6160–6164, doi:10.1002/2013GL058228.

Casey, J. A., and R. E. J. Kelly (2010), Estimating the equilibrium line of Devon Ice Cap , Nunavut , from RADARSAT-1 ScanSAR wide imagery, *Can. J. Remote Sens.*, *36*(Suppl.1), S41–S55, doi:10.5589/m10-013.

Cogley, J. G., W. P. Adams, and M. A. Ecclestone (1996), Mass balance of White Glacier, Axel Heiberg Island, N.W.T., Canada, 1960-91, *J. Gl*, *42*(142), doi:10.3198/1996JoG42-142-548-563.

Cogley, J. G. et al. (2011), *Glossary of Glacier Mass Balance and Related Terms*, IHP-VII Technical Documents in Hydrology No. 86, IACS Contribution No. 2, UNESCO-IHP, Paris.

Copland, L., M. Sharp, and A. Dowdeswell (2003a), The distribution and flow characteristics of surge-type glaciers in the Canadian High Arctic, *Ann. Glaciol.*, *36*(1), 73–81, doi:10.3189/172756403781816301.

Copland, L., M. J. Sharp, P. Nienow, and R. G. Bingham (2003b), The distribution of basal motion beneath a High Arctic polythermal glacier, *J. Glaciol.*, *49*(166), doi:10.3189/172756503781830511.

Copland, L., S. Pope, M. P. Bishop, J. F. Shroder, P. Clendon, A. B. G. Bush, U. Kamp, Y. B. Seong, and L. A. Owen (2009), Glacier velocities across the Karakoram, *Ann. Glaciol.*, *50*(52), 41–49, doi:10.3189/172756409789624229.

Cuffey, K. M. (2001), Interannual variability of elevation on the Greenland ice sheet: effects of firm densification, and establishment of a multi-century benchmark, *J. Glaciol.*, *47*(158), 369–377, doi:10.3189/172756501781832151.

Cuffey, K. M., and W. S. B. Paterson (2010), *The Physics of Glaciers*, 4th edn., Burlington, MA: Elsevier Inc.

Derksen, C. et al. (2012), Variability and change in the Canadian cryosphere, *Clim. Chang.*, *115*, 59–88, doi:10.1007/s10584-012-0470-0.

Fatland, D. R., C. S. Lingle, and M. Truffer (2003), A surface motion survey of Black Rapids Glacier, Alaska, U.S.A, *Ann. Glaciol.*, *36*(1), 29–36, doi:10.3189/172756403781816095.

Fisher, D. et al. (1998), Penny ice cap cores, Baffin Island,Canada, and the wisconsinan foxe

dome connection: two states of Hudson Bay Ice Cover, *Science*, *279*(5351), 692–5, doi:10.1126/science.279.5351.692.

Fisher, D., J. Zheng, D. Burgess, C. Zdanowicz, C. Kinnard, M. Sharp, and J. Bourgeois (2012), Recent melt rates of Canadian arctic ice caps are the highest in four millennia, *Glob. Planet. Change*, *84–85*, 3–7, doi:10.1016/j.gloplacha.2011.06.005.

Fitch, A. J., A. Kadyrov, W. J. Christmas, and J. Kittler (2002), Orientation Correlation, in *Procedings of the British Machine Vision Conference 2002*, pp. 133–142, Cardiff, UK, 2-5 September 2002.

Fitzpatrick, A. W., A. Hubbard, I. Joughin, D. J. Quincey, D. Van As, A. P. B. Mikkelsen, S. H. Doyle, B. Hasholt, and G. Jones (2013), Ice flow dynamics and surface meltwater flux at a land-terminating sector of the Greenland ice sheet, *J. Glaciol.*, *59*(216), 687–696, doi:10.3189/2013JoG12J143.

Fricker, H. A., A. Borsa, B. Minster, C. Carabajal, K. Quinn, and B. Bills (2005), Assessment of ICESat performance at the salar de Uyuni, Bolivia, *Geophys. Res. Lett.*, *32*(21), 1–5, doi:10.1029/2005GL023423.

Gardner, A., G. Moholdt, A. Arendt, and B. Wouters (2012), Accelerated contributions of Canada's Baffin and Bylot Island glaciers to sea level rise over the past half century, *Cryosph.*, *6*, 1103–1125, doi:10.5194/tc-6-1103-2012.

Gardner, A. S., G. Moholdt, B. Wouters, G. J. Wolken, D. O. Burgess, M. J. Sharp, J. G. Cogley, C. Braun, and C. Labine (2011), Sharply increased mass loss from glaciers and ice caps in the Canadian Arctic Archipelago, *Nature*, *473*(7347), 357–360, doi:10.1038/nature10089.

Gardner, A. S. et al. (2013), A reconciled estimate of glacier contributions to sea level rise: 2003 to 2009., *Science*, *340*(6134), 852–857, doi:10.1126/science.1234532.

Gascon, G., M. Sharp, D. Burgess, P. Bezeau, and A. B. G. Bush (2013), Changes in accumulation-area firn stratigraphy and meltwater flow during a period of climate warming: Devon Ice Cap, Nunavut, Canada, *J. Geophys. Res. Earth Surf.*, *118*(4), 2380–2391, doi:10.1002/2013JF002838.

Glen, J. W. (1955), The creep of polycrystalline ice, *Proc. R. Soc. London*, *228*(1175), 519–538, doi:10.1098/rspa.1955.0066.

Gray, A. L., N. Short, K. E. Mattar, and K. C. Jezek (2001), Velocities and Flux of the Filchner Ice Shelf and its Tributaries determined from Speckle Tracking Interferometry, *Can. J. Remote Sens.*, *27*(3), 193–206, doi:10.1080/07038992.2001.10854936.

Gray, L., D. Burgess, L. Copland, M. N. Demuth, T. Dunse, K. Langley, and T. V. Schuler (2015), CryoSat-2 delivers monthly and inter-annual surface elevation change for Arctic ice caps, *Cryosph.*, *9*, 1895–1913, doi:10.5194/tc-9-1895-2015.

Hagen, J. O., T. Eiken, J. Kohler, and K. Melvold (2005), Geometry changes on Svalbard glaciers: mass-balance or dynamic response?, *Ann. Glaciol.*, *42*(1), 255–261, doi:10.3189/172756405781812763.

Harig, C., and F. J. Simons (2016), Ice mass loss in Greenland, the Gulf of Alaska, and the

Canadian Archipelago: Seasonal cycles and decadal trends, *Geophys. Res. Lett.*, *43*(7), 3150–3159, doi:10.1002/2016GL067759.

Heid, T., and A. Kääb (2012a), Evaluation of existing image matching methods for deriving glacier surface displacements globally from optical satellite imagery, *Remote Sens. Environ.*, *118*, 339–355, doi:10.1016/j.rse.2011.11.024.

Heid, T., and A. Kääb (2012b), Repeat optical satellite images reveal widespread and long term decrease in land-terminating glacier speeds, *Cryosph.*, *6*, 467–478, doi:10.5194/tc-6-467-2012.

Hock, R. (1999), A distributed temperature-index ice- and snowmelt model including potential direct solar radiation, *J. Glaciol.*, *45*(149), 101–111.

Hock, R. (2003), Temperature index melt modelling in mountain areas, *J. Hydrol.*, *282*(1), 104–115, doi:10.1016/S0022-1694(03)00257-9.

Holdsworth, G. (1984), Glaciological reconnaissance of an ice core drilling site, Penny Ice Cap, Baffin Island, *J. Glaciol.*, *30*(104), 3–15.

Howat, I. M., I. Joughin, M. Fahnestock, B. E. Smith, and T. A. Scambos (2008), Synchronous retreat and acceleration of southeast Greenland outlet glaciers 2000-06: Ice dynamics and coupling to climate, *J. Glaciol.*, *54*(187), 646–660, doi:10.3189/002214308786570908.

Huss, M., and D. Farinotti (2012), Distributed ice thickness and volume of all glaciers around the globe, *J. Geophys. Res.*, *117*(F04010), 1–10, doi:10.1029/2012JF002523.

Huss, M., and R. Hock (2015), A new model for global glacier change and sea-level rise, *Front. Earth Sci.*, *3*(54), 1–22, doi:10.3389/feart.2015.00054.

Huss, M., G. Jouvet, D. Farinotti, and A. Bauder (2010), Future high-mountain hydrology: A new parameterization of glacier retreat, *Hydrol. Earth Syst. Sci.*, *14*(5), 815–829, doi:10.5194/hess-14-815-2010.

Iken, A. (1981), The effect of the subglacial water pressure on the sliding velocity of a glacier in an idealized numerical model, *J. Glaciol.*, *27*(97), 407–421, doi:10.3198/1981JoG27-97-407-421.

IPCC (2013), *Climate Change 2013: The Physical Science Basis. Contribution of Working Group I to the Fifth Assessment Report of the Intergovernmental Panel on Climate Change*, [Stocker, T.F., D. Qin, G.K. Plattner, M. Tignor, SK. Allen, J. Boschung, A. Nauels, Y. Xia, V. Bex and P.M. Midgley (eds.)]. Cambridge University Press, Cambridge, United Kingdom and New York, NY, USA, 1535 pp.

Jacob, T., J. Wahr, W. T. Pfeffer, and S. Swenson (2012), Recent contributions of glaciers and ice caps to sea level rise, *Nature*, *482*(7386), 514–518, doi:10.1038/nature10847.

Janssens, I., and P. Huybrechts (2000), The treatment of meltwater retention in mass-balance parameterizations of the Greenland ice sheet, *Ann. Glaciol.*, *31*(1), 133–140, doi:10.3189/172756400781819941.

Joughin, I. (2002), Ice-sheet velocity mapping: A combined interferometric and speckle-tracking

approach, *Ann. Glaciol.*, *34*(1), 195–201, doi:10.3189/172756402781817978.

Kääb, A., and M. Vollmer (2000), Surface geometry, thickness changes and flow fields on creeping mountain permafrost: Automatic extraction by digital image analysis, *Permafr. Periglac. Process.*, *11*, 315–326, doi:10.1002/1099-1530(200012).

Kamb, B., C. F. Raymond, W. D. Harrison, H. Engelhardt, K. A. Echelmeyer, N. Humphrey, M. M. Brugman, and T. Pfeffer (1985), Glacier surge mechanism: 1982-1983 surge of Variegated glacier, Alaska, *Science 227*(4686), 469–479, doi:10.1126/science.227.4686.469.

Kaufman, D. S. et al. (2009), Recent Warming Reverses Long-Term Arctic Cooling, *Science 325*, 1236–1239, doi:10.1126/science.1173983.

Kick, W. (1962), Variations of some central asiatic glaciers, *IASH Publ. (Symposium Obergurgl 1962 – Var. Regime Exist. Glaciers)*, *58*, 223–229.

Kovacs, A., A. J. Gow, and R. M. Morey (1995), The in-situ dielectric constant of polar firn revisited, *Cold Reg. Sci. Technol.*, *23*(3), 245–256, doi:10.1016/0165-232X(94)00016-Q.

Krabill, W. (2013), *Icebridge ATM L1B Elevation and Return Strength, Version 2 (May 2005; April 2013; April 2014)*, NASA National Snow and Ice Data Center Distributed Active Archive Center, Boulder, Colorado, USA.

Krabill, W. B., R. H. Thomas, C. F. Martin, R. N. Swift, and E. B. Frederick (1995), Accuracy of airborne laser altimetry over the Greenland ice sheet, *Int. J. Remote Sens.*, *16*(7), 1211–1222, doi:10.1080/01431169508954472.

Krabill, W. B., W. Abdalati, E. B. Frederick, S. S. Manizade, C. F. Martin, J. G. Sonntag, R. N. Swift, R. H. Thomas, and J. G. Yungel (2002), Aircraft laser altimetry measurement of elevation changes of the Greenland ice sheet: technique and accuracy assessment, *J. Geodyn.*, *34*(3–4), 357–376, doi:10.1016/S0264-3707(02)00040-6.

Krimmel, R. M. (1999), Analysis of Difference Between Direct and Geodetic Mass Balance Measurements at South Cascade Glacier, Washington, *Geogr. Ann. Ser. A Phys. Geogr.*, *81*(4), 653–658, doi:10.1111/1468-0459.00093.

Lee, D. S., J. C. Storey, M. J. Choate, and R. W. Hayes (2004), Four years of Landsat-7 on-orbit geometric calibration and performance, *IEEE Trans. Geosci. Remote Sens.*, *42*(12), 2786–2795, doi:10.1109/TGRS.2004.836769.

Lenaerts, J. T., J. van Angelen, M. van den Broeke, A. Gardner, B. Wouters, and E. van Meijgaard (2013), Irreversible mass loss of Canadian Arctic Archipelago glaciers, *Geophys. Res. Lett.*, *40*(5), 870–874, doi:10.1002/grl.50214.

Lenaerts, J. T. M., M. R. Van Den Broeke, W. J. Van De Berg, E. Van Meijgaard, and P. Kuipers Munneke (2012), A new, high-resolution surface mass balance map of Antarctica (1979-2010) based on regional atmospheric climate modeling, *Geophys. Res. Lett.*, *39*, 1–5, doi:10.1029/2011GL050713.

Li, J., H. J. Zwally, H. Cornejo, and D. Yi (2003), Seasonal variation of snow-surface elevation in North Greenland as modeled and detected by satellite radar altimetry, *Ann. Glaciol.*,

37(1), 233–238, doi:10.3189/172756403781815889.

Ligtenberg, S. R. M., B. Medley, M. R. van den Broeke, and P. Kuipers Munneke (2015), Antarctic firn compaction rates from repeat-track airborne radar data: II. Firn model evaluation, *Ann. Glaciol.*, *56*(70), 167–174, doi:10.3189/2015AoG70A204.

Luckman, A., T. Murray, R. de Lange, and E. Hanna (2006), Rapid and synchronous ice-dynamic changes in East Greenland, *Geophys. Res. Lett.*, *33*(3), 1–4, doi:10.1029/2005GL025428.

Machguth, H., M. MacFerrin, D. van As, J. E. Box, C. Charalampidis, W. Colgan, R. S. Fausto, H. A. J. Meijer, E. Mosley-Thompson, and R. S. W. van de Wal (2016), Greenland meltwater storage in firn limited by near-surface ice formation, *Nat. Clim. Chang.*, *6*, 390–393, doi:10.1038/nclimate2899.

Mair, D., I. Willis, U. H. Fischer, B. Hubbard, P. Nienow, and A. Hubbard (2003), Hydrological controls on patterns of surface, internal and basal motion during three spring events’’: Haut Glacier d’Arolla, Switzerland, *J. Glaciol.*, *49*(167), 555–567, doi:10.3189/172756503781830467.

Marzeion, B., A. H. Jarosch, and M. Hofer (2012), Past and future sea-level change from the surface mass balance of glaciers, *Cryosph.*, *6*, 1295–1322, doi:10.5194/tc-6-1295-2012.

Maxwell, J. B. (1981), Climatic Regions of the Canadian Arctic Islands, *Arctic*, *34*, 225–240.

Moholdt, G., C. Nuth, J. Hagen, and J. Kohler (2010), Recent elevation changes of Svalbard glaciers derived from ICESat laser altimetry, *Remote Sens. Environ.*, *114*(11), 2756–2767, doi:10.1016/j.rse.2010.06.008.

Morris, E. M., and D. J. Wingham (2014), Densification of polar snow: Measurements, modeling, and implications for altimetry, *J. Geophys. Res. Earth Surf.*, *119*(2), 349–365, doi:10.1002/2013JF002898.

Nienow, P., M. Sharp, and I. Willis (1998), Seasonal changes in the morphology of the subglacial drainage system, Haut Glacier d’Arolla, Switzerland, *Earth Surf. Process. Landforms*, *23*(9), 825–843, doi:10.1002/(SICI)1096-9837(199809)23:9<825::AID-ESP893>3.0.CO;2-2.

Nilsson, J., L. S. Sorensen, V. R. Barletta, and R. Forsberg (2015), Mass change of Arctic ice caps and glaciers: implications of regionalizing elevation changes, *Cryosph.*, *9*, 139–150, doi:10.5194/tc-9-139-2015.

Noël, B., W. J. Van De Berg, E. Van Meijgaard, P. Kuipers Munneke, R. S. W. Van De Wal, and M. R. Van Den Broeke (2015), Evaluation of the updated regional climate model RACMO2.3: Summer snowfall impact on the Greenland Ice Sheet, *Cryosph.*, *9*(5), 1831–1844, doi:10.5194/tc-9-1831-2015.

Oerlemans, J. (2005), Extracting a climate signal from 169 glacier records., *Science (80-.).*, *308*(5722), 675–677, doi:10.1126/science.1107046.

Orvig, S. (1954), Glacial-meteorological observations on icecaps in Baffin Island, *Geogr. Ann.*, *36*(3/4), 193–318.

Papasodoro, C., E. Berthier, A. Royer, C. Zdanowicz, and A. Langlois (2015), Area, elevation and mass changes of the two southernmost ice caps of the Canadian Arctic Archipelago between 1952 and 2014, *Cryosph.*, *9*, 1535–1550, doi:10.5194/tc-9-1535-2015.

Papasodoro, C., A. Royer, A. Langlois, and E. Berthier (2016), Potential of RADARSAT-2 stereo radargrammetry for the generation of glacier DEMs, *J. Glaciol.*, *62*(233), 486–496, doi:10.1017/jog.2016.44.

Parizek, B. R., and R. B. Alley (2004), Implications of increased Greenland surface melt under global-warming scenarios: ice-sheet simulations, *Quat. Sci. Rev.*, *23*(9–10), 1013–1027, doi:10.1016/j.quascirev.2003.12.024.

Pfeffer, W. et al. (2014), The Randolph Glacier Inventory: a globally complete inventory of glaciers., *J. Glaciol.*, *60*(221), 537–552, doi:10.3189/2014JoG13J176.

Radic, V., and R. Hock (2011), Regionally differentiated contribution of mountain glaciers and ice caps to future sea-level rise, *Nat. Geosci. Lett.*, (January), 91–94, doi:10.1038/ngeo1052.

Reijmer, C. H., M. R. Van Den Broeke, X. Fettweis, J. Ettema, and L. B. Stap (2012), Refreezing on the Greenland ice sheet: A comparison of parameterizations, *Cryosphere*, *6*, 743–762, doi:10.5194/tc-6-743-2012.

Rothlisberger, H. (1955), Studies in glacier physics on the Penny Ice Cap, Baffin Island, 1953: Part III, seismic sounding, *J. Glaciol.*, *2*(18), 539–552, doi:10.3198/1955JoG2-18-539-552.

Schaffer, N., L. Copland, and C. Zdanowicz (in review-a), Ice velocity changes on Penny Ice Cap, Baffin Island, since the 1950s, *J. Glaciol.*

Schaffer, N., L. Copland, C. Zdanowicz, D. Burgess, and J. Nilsson (in review-b), Recent elevation changes of Penny Ice Cap, Baffin Island, corrected for ice dynamics and firn densification, *J. Geophys. Res. Earth Surf.*

Schoof, C. (2010), Ice-sheet acceleration driven by melt supply variability, *Nature*, *468*, 803–6, doi:10.1038/nature09618.

Sepp, M., and J. Jaagus (2010), Changes in the activity and tracks of Arctic cyclones, *Clim. Change*, *105*, 577–595, doi:10.1007/s10584-010-9893-7.

Serreze, M. C., M. M. Holland, and J. Stroeve (2007), Perspectives on the Arctic's shrinking sea-ice cover., *Science*, *315*(5818), 1533–6, doi:10.1126/science.1139426.

Sharp, M., D. Burgess, J. Cogley, M. Ecclestone, C. Labine, and G. J. Wolken (2011), Extreme melt on Canada's Arctic ice caps in the 21st century, *Geophys. Res. Lett.*, *38*(11), 1–5, doi:10.1029/2011GL047381.

Shepherd, A. et al. (2012), A reconciled estimate of ice-sheet mass balance, *Science*, *338*(6111), 1183–1189, doi:10.1126/science.1228102.

Shi, L., C. T. Allen, J. R. Ledford, F. Rodriguez-Morales, W. A. Blake, B. G. Panzer, S. C. Prokopiack, C. J. Leuschen, and S. Gogineni (2010), Multichannel coherent radar depth sounder for NASA operation ice bridge, *Int. Geosci. Remote Sens. Symp.*, 1729–1732, doi:10.1109/IGARSS.2010.5649518.

Short, N. H., and A. L. Gray (2005), Glacier dynamics in the Canadian High Arctic from RADARSAT-1 speckle tracking, *Can. J. Remote Sens.*, *31*(3), 225–239.

Short, N. H., and a L. Gray (2004), Potential for RADARSAT-2 interferometry: glacier monitoring using speckle tracking, *Can. J. Remote Sens.*, *30*(3), 504–509, doi:10.5589/m03-071.

Slangen, A. B. A., C. A. Katsman, R. S. W. van de Wal, L. L. A. Vermeersen, and R. E. M. Riva (2012), Towards regional projections of twenty-first century sea-level change based on IPCC SRES scenarios, *Clim. Dyn.*, *38*, 1191–1209, doi:10.1007/s00382-011-1057-6.

Sole, A., P. Nienow, I. Bartholomew, D. Mair, T. Cowton, A. Tedstone, and M. A. King (2013), Winter motion mediates dynamic response of the Greenland Ice Sheet to warmer summers, *Geophys. Res. Lett.*, *40*(15), 3940–3944, doi:10.1002/grl.50764.

Sorteberg, A., and J. E. Walsh (2008), Seasonal cyclone variability at 70°N and its impact on moisture transport into the Arctic, *Tellus , Ser. A*, *60*, 570–586, doi:10.1111/j.1600-0870.2008.00314.x.

Storey, J. C., and M. J. Choate (2004), Landsat-5 Bumper-Mode Geometric Correction, *IEEE Trans. Geosci. Remote Sens.*, *42*(12), 2695–2703, doi:10.1109/TGRS.2004.836390.

Sundal, A. V., A. Shepherd, P. Nienow, E. Hanna, S. Palmer, and P. Huybrechts (2011), Melt-induced speed-up of Greenland ice sheet offset by efficient subglacial drainage., *Nature*, *469*, 521–4, doi:10.1038/nature09740.

Sylvestre, T., L. Copland, M. N. Demuth, and M. Sharp (2013), Spatial patterns of snow accumulation across Belcher Glacier, Devon Ice Cap, Nunavut, Canada, *J. Glaciol.*, *59*(217), 874–882, doi:10.3189/2013JoG12J227.

Tedstone, A. J., P. W. Nienow, A. J. Sole, D. W. F. Mair, T. R. Cowton, I. D. Bartholomew, and M. a King (2013), Greenland ice sheet motion insensitive to exceptional meltwater forcing., *Proc. Natl. Acad. Sci. U. S. A.*, *110*(49), 19719–24, doi:10.1073/pnas.1315843110.

Tedstone, A. J., P. W. Nienow, N. Gourmelen, A. Dehecq, D. Goldberg, and E. Hanna (2015), Decadal slowdown of a land-terminating sector of the Greenland Ice Sheet despite warming, *Nature*, *526*, 692–695, doi:10.1038/nature15722.

Thomson, L., and L. Copland (2017), Multi-decadal reduction in glacier velocities and mechanisms driving deceleration at polythermal White Glacier, Arctic Canada., *J. Glaciol.*, 63(239), 450-463, doi:10.1017/jog.2017.3.

Thomson, L. I., M. Zemp, L. Copland, J. G. Cogley, and M. A. Ecclestone (2016), Comparison of geodetic and glaciological mass budgets for White Glacier , Axel Heiberg Island , Canada, *J. Glaciol.*, 63(237), 55-66, doi:10.1017/jog.2016.112.

Trussel, B. L., M. Truffer, R. Hock, R. J. Motyka, M. Huss, and J. Zhang (2015), Runaway thinning of the low-elevation Yakutat Glacier, Alaska, and its sensitivity to climate change, *J. Glaciol.*, *61*(225), 65–75, doi:10.3189/2015JoG14J125.

Van Wychen, W., L. Copland, L. Gray, D. Burgess, B. Danielson, and M. Sharp (2012), Spatial and temporal variation of ice motion and ice flux from Devon Ice Cap, Nunavut, Canada, *J.*

Glaciol., *58*(210), 657–664, doi:10.3189/2012JoG11J164.

Van Wychen, W., D. Burgess, L. Gray, L. Copland, M. Sharp, J. Dowdeswell, and T. Benham (2014), Glacier velocities and dynamic ice discharge form the Queen Elizabeth Islands, Nunavut, Canada, *Geophys. Res. Lett.*, *41*(2), 484–490, doi:10.1002//2013GL058558.

Van Wychen, W., L. Copland, D. Burgess, L. Gray, and N. Schaffer (2015), Glacier Velocities and Dynamic Discharge from the Ice Masses of Baffin Island and Bylot Island, Nunavut, Canada, *Can. J. Earth Sci.*, *52*(11), 980–989, doi:10.1139/cjes-2015-0087.

Van Wychen, W., J. Davis, D. Burgess, L. Copland, L. Gray, M. Sharp, and C. Mortimer (2016), Characterizing interannual variability of glacier dynamics and dynamic discharge (1999-2015) for the ice masses of Ellesmere and Axel Heiberg Islands, Nunavut, Canada, *J. Geophys. Res. Earth Surf.*, *121*(1), 1–25, doi:10.1002/2015JF003708.

Vincent, C., A. Soruco, D. Six, and E. L. E. Meur (2009), Glacier thickening and decay analysis from 50 years of glaciological observations performed on Glacier d'Argentière, Mont Blanc area, France, *Ann. Glaciol.*, *50*(50), 73–79, doi:10.3189/172756409787769500.

Vincent, L. A., X. Zhang, R. D. Brown, Y. Feng, E. Mekis, E. J. Milewska, H. Wan, and X. L. Wang (2015), Observed Trends in Canada's Climate and Influence of Low-Frequency Variability Modes, *J. Clim.*, *28*, 4545–4560, doi:10.1175/JCLI-D-14-00697.1.

Waechter, A., L. Copland, and E. Herdes (2015), Modern glacier velocities across the Icefield Ranges, St Elias Mountains, and variability at selected glaciers from 1959 to 2012, *J. Glaciol.*, *61*(228), 624–634, doi:10.3189/2015JoG14J147.

van de Wal, R. S. W., W. Boot, M. R. van den Broeke, C. J. P. P. Smeets, C. H. Reijmer, J. J. a Donker, and J. Oerlemans (2008), Large and rapid melt-induced velocity changes in the ablation zone of the Greenland Ice Sheet., *Science (80-.).*, *321*(5885), 111–3, doi:10.1126/science.1158540.

Ward, W. H. (1954), Glaciological studies in the Penny Highland, Baffin Island, 1953, *Int. Assoc. Sci. Hydrol. Bull.*, *39*, 297–308.

Ward, W. H. (1955), Studies in Glacier Physics on the Penny Ice Cap, Baffin Island, 1953 Part IV: The flow of Highway Glacier, *J. Glaciol.*, *2*(18), 592–600.

Ward, W. H., and P. D. Baird (1954), Studies in glacier physics on the Penny Ice Cap, Baffin Island, 1953: Part I, A description of the Penny Ice Cap, its accumulation and ablation, *J. Glaciol.*, *2*(15), 342–355.

Weber, J. R., and P. Andrieux (1970), Radar Soundings on the Penny Ice Cap, Baffin Island, *J. Glaciol.*, *9*(55), 49–54, doi:10.3198/1970JoG9-55-49-54.

Weber, J. R., and R. V. Cooper (1993), *Monitoring of elevation changes of the Penny Ice Cap, Baffin Island*, Geological Survey of Canada, Geophysics Division, Ottawa.

Williamson, S., M. Sharp, J. Dowdeswell, and T. Benham (2008), Iceberg calving rates from northern Ellesmere Island ice caps, Canadian Arctic, 1999-2003, *J. Glaciol.*, *54*(186), 391–400, doi:10.3189/002214308785837048.

Wilson, R., S. H. Mernild, J. K. Malmros, C. Bravo, and D. Carrion (2016), Surface velocity fluctuations for Glaciar Universidad, central Chile, between 1967 and 2015, *J. Glaciol.*, Available on CJO 2016, doi:10.1017/jog.2016.73.

Zdanowicz, C., A. Smetny-Sowa, D. Fisher, N. Schaffer, L. Copland, J. Eley, and F. Dupont (2012), Summer melt rates on Penny Ice Cap, Baffin Island: Past and recent trends and implications for regional climate, *J. Geophys. Res.*, *117*(F02006), 1–21, doi:10.1029/2011JF002248.

Zdanowicz, C., E. Kruemmel, D. Lean, A. Poulain, C. Kinnard, E. Yumvihoze, J. Chen, and H. Hintelmann (2015), Pre-industrial and recent (1970-2010) atmospheric deposition of sulfate and mercury in snow on southern Baffin Island, Arctic Canada, *Sci. Total Environ.*, *509–510*, 104–114, doi:10.1016/j.scitotenv.2014.04.092.

Zwally, H. J., Schutz, R., Bentley, C., Bufton, J., Herring, T., Minster, B., Spinhirne, J., and Thomas, R. (2011), *GLAS/ICESat L1B Global Elevation Data V031, 20 February 2003 to 11 October 2009*, Digital Media, Boulder, CO.

Zwally, H. J., and J. Li (2002), Seasonal and interannual variations of firn densification and ice-sheet surface elevation at the Greenland summit, *J. Glaciol.*, *48*(161), 199–207, doi:10.3189/172756502781831403.

Zwally, H. J., W. Abdalati, T. Herring, K. Larson, J. Saba, and K. Steffen (2002), Surface Melt-Induced Acceleration of Greenland Ice-Sheet Flow, *Science*, *297*(5579), 218–222, doi:10.1126/science.1072708.